8-9-2014

Dielectric Properties of Composite Materials during Damage Accumulation and Fracture

Md. Rassel Raihan
University of South Carolina - Columbia

Dielectric Properties of Composite Materials during Damage Accumulation and Fracture

by

Md. Rassel Raihan

Bachelor of Science
Bangladesh University of Engineering & Technology, 2007

Master of Engineering
University of South Carolina, 2012

Submitted in Partial Fulfillment of the Requirements

For the Degree of Doctor of Philosophy in

Mechanical Engineering

College of Engineering and Computing

University of South Carolina

2014

Accepted by:

Kenneth L. Reifsnider, Major Professor

Prasun K. Majumdar, Committee Member

Fanglin Chen, Committee Member

Harry J. Ploehn, Committee Member

Lacy Ford, Vice Provost and Dean of Graduate Studies

DEDICATION

This dissertation is dedicated to my Parents, Brothers and my Wife for their endless love, support and encouragement.

ACKNOWLEDGEMENTS

I would like to thank Dr. Kenneth Reifsnider, my dissertation research advisor, for his invaluable advice, guidance, and support that made this work possible. His encouraging words and positive way of thinking motivated me throughout my doctoral research. I didn't just learn how to excel in research from Dr. Reifsnider, but I also learned how to motivate others. It has been enjoyable, challenging and above all an educational experience working with him.

I would also like to thank the other members of my advisory committee. I am grateful to Dr. Majumdar for his help and support from the very first day of my graduate life both in experimental and academic activities. His enthusiasm and dedication towards the scientific research has been an inspiration to my research. Dr. Chen has been a tremendous asset. It is rare to find an instructor that has such a genuine concern for students as Dr. Chen. Considerable knowledge was gained through participation in his course on Fuel Cells. Dr. Ploehn has been a pleasure to work with, and a privilege to be associated with a gentleman with such a distinguished career in scientific research.

I really appreciate the help of my colleagues, Jon-Michael Adkins, Jeffrey Baker, Fazle Rabbi and Lee Woolley, during my doctoral research.

I would like to thank my Parents and Brothers for their sacrifices and unselfish love and support. Lastly but not least, I would like to thank, the love of my life, my wife Piya for all her support throughout this process. I am forever thankful and truly blessed to have her in my life.

ABSTRACT

Fiber reinforced polymer matrix composite materials have many unique properties and their high performance makes them available to use in many advanced technologies i.e. aerospace, microelectronics, and energy storage. There is a correlation that exists between the long term behavior of those materials under combined mechanical, thermal, and electrical fields, and the functional properties and characteristics of the composite materials that requires a fundamental understanding of the material state changes caused by deformation and damage accumulation. This will ultimately lead, for example, to the design and synthesis of optimal multifunctional material systems. Composite materials are heterogeneous and the complex morphology of these material systems has been investigated for decades to achieve multi-functionality and reliable performance in extreme environments. These heterogeneous materials are inherently dielectric. Broadband Dielectric Spectroscopy (BbDS) is a robust tool for dielectric material characterization often used in polymer industries. In composite processing this method is employed to monitor the composite curing process. Dielectric spectra of heterogeneous materials are altered by many factors, e.g., electrical and structural interactions between particles, morphological heterogeneity, and shape and orientation of the constituent phases of the material system. During the service life of composites, damage occurs progressively and accumulates inside the materials. The process of microdefect interaction and accumulation to create a final fracture path is an active research area.

The present research is designed to investigate material state change using a new non-invasive interrogation method for establishing not only internal integrity but also the nature and distribution of internal material structure and defect morphology changes by using Broadband Dielectric Spectroscopy (BbDS) to detect and characterize permittivity changes during the history of loading. Interpretations of the results by analysis of discrete local details, and prognosis of performance will be discussed by the introduction of a new technique, called Generalized Compliance, which directly and quantitatively reflects material state changes.

A two dimensional computational model was also developed using COMSOL^{TM}. The effects of volume fraction and the distribution of the defects inside the material volume, and influence of the permittivities and ohmic conductivities of the host material and defects on the effective dielectric behavior of the resulting composite as a function of applied frequency spectra are discussed. Single frequency dielectric behavior with increasing defect development inside the composite is used to interpret the in-situ BbDS experimental results for the progressive damage of the material systems investigated.

TABLE OF CONTENTS

LIST OF FIGURES

CHAPTER 1 INTRODUCTION

Composite materials are now widely used in advanced industries, i.e. aerospace, naval, sport, automotive, electronic packaging and energy storage, in which engineered heterogeneity has been designed and introduced to achieve specific engineering functions.

Emerging technologies in the areas of electronics and energy storage require the design of next-generation dielectric-component materials with well-defined structure and properties with higher performance under applied voltage and temperature fields. Researchers from Imperial College London and their European partners, including Volvo Car Corporation, have developed a prototype strong and light weight multifunctional structural composite material composed of carbon fibers and a polymer resin which can store and discharge electrical energy and also be used as a car body structure [1-2].

Aerospace industries are more inclined to use these multifunctional composites to reduce the weight to achieve fuel efficiency, and also for energy storage and structural stability.

To design and synthesize an effective material system requires a fundamental understanding of the material state change caused by applied mechanical, thermal, and electrical fields. Under combined applied field conditions, materials degrade progressively. To evaluate such material state changes there are many tools and methods but most of them do not give a direct and quantitative assessment of the damage state.

Composite materials by nature are heterogeneous dielectric material systems. When degradation happens in the material system, it develops a combination of material state and morphology changes. Broadband Dielectric Spectroscopy (BbDS) is a robust tool to extract the material-level information, including the morphology changes caused by micro-detect generation and the orientation of those defects. Composite materials should be designed in such a way that they can cope with their applied environments; to achievethis, it is necessary to engineer the material system from the nano- and micro-scale by controlling the shape, size, properties and interfaces of those systems. The local material states of high performance composite structures change during their service period. In order to achieve a prognosis of the composite durability, structural integrity, damage tolerance, and fracture toughness, we must take into consideration the appropriate balance equations, defect growth relationships, and constitutive equations with specified material property variations. Local changes in the material state also have significant effects on the prognosis of the composite system.

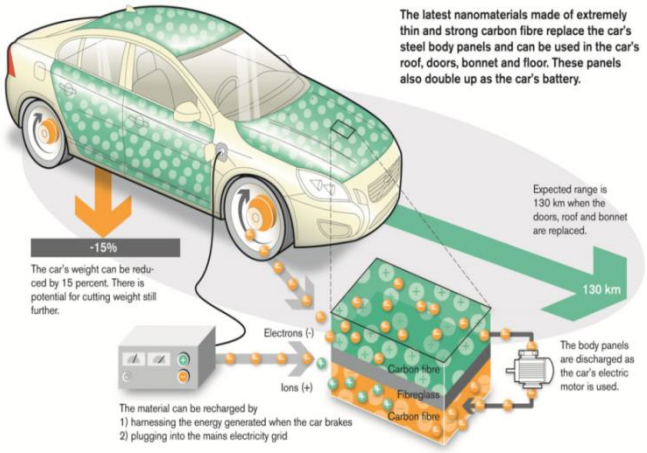

Figure 1.1 Volvo car body panel serve as battery [2].

1.1 Objectives

The objective of the present work is application of a robust material characterization tool BbDS for the prognosis of composite material systems during the service life. Dielectric property measurements and analysis will follow the material state changes (i.e. formation of microcracks, interaction of the cracks, accumulations of the defects, fiber fracture and changes in the morphology of the material during the introduction of the progressive damage) from initial pristine condition to the final failure for various applied field conditions.

Find out a approach based on the dielectric properties of the material system to identify the strongest and weakest before applying any load and which could be used to define mechanical properties such as strength, life, and durability of the material.

Construct a basic computer simulation model and validate with the experimental results.

1.2 Dissertation layout

Chapter two represents a literature review of the progressive failure of the composite materials, state of the art detection techniques and a description of Broadband Dielectric Spectroscopy.

In chapter three there is a short discussion about the major experimental facilities that were used during the dissertation work.

Chapter four presents the results of the dielectric study of SOFC composite materials without any electrochemistry.

In chapter five a new In-situ BbDS method is introduced to follow the progressive failure of the composite materials.

Chapter six discusses the ex-situ dielectric study and prognosis of the composite materials based on BbDS data.

In chapter seven a basic computational model is presented and compared with the experimental results.

CHAPTER 2 LITERATURE REVIEW

2.1 Progressive Failure in Composite Materials

Damage in composite materials under static, creep and fatigue conditions have been studied and published in engineering journals since the late 1970s [1]. Degradation of composite materials is generally initiated and evolves by microdamage development events, mostly matrix microcracking and growth, delamination, fiber fracture, fiber-matrix decoupling, and microbuckling.

2.1.1 Microcracking

Microcracking is the most general damage mode in composite materials which actually changes the material mechanical properties [3-20]. Microcracks can originate from the debonding of fiber/matrix interfaces or existing defects, voids or inclusions. Figure 2.1 is an example of fiber matrix debonding and initiation of matrix microcracks [8].These microcracks are usually distributed densely after the initial development, and grow through the ply thickness and width, generally parallel to the fiber direction in a given ply. Figure 2.2 illustrates their development through the ply thickness for both continuous fiber and woven composite laminates [8]. They usually do not develop and grow independently; rather, their local stress fields typically interact. Usually, distributed amounts of microcracks have small or no effect on the strength of the fiber controlled composite laminate, but they can change the global stiffness considerably and cause local stress redistributions. From experimental data, changes in stiffness are not uniform throughout the life of a material element; initially and again just before fracture,

the change is large, and at intermediate stages the rate of stiffness change is more moderate [4-9].

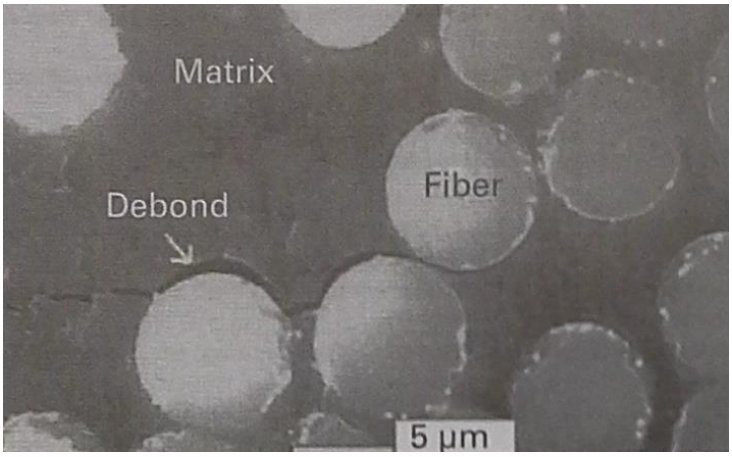

Figure 2.1 matrix crack initiation from fiber/matrix debonding. [8]

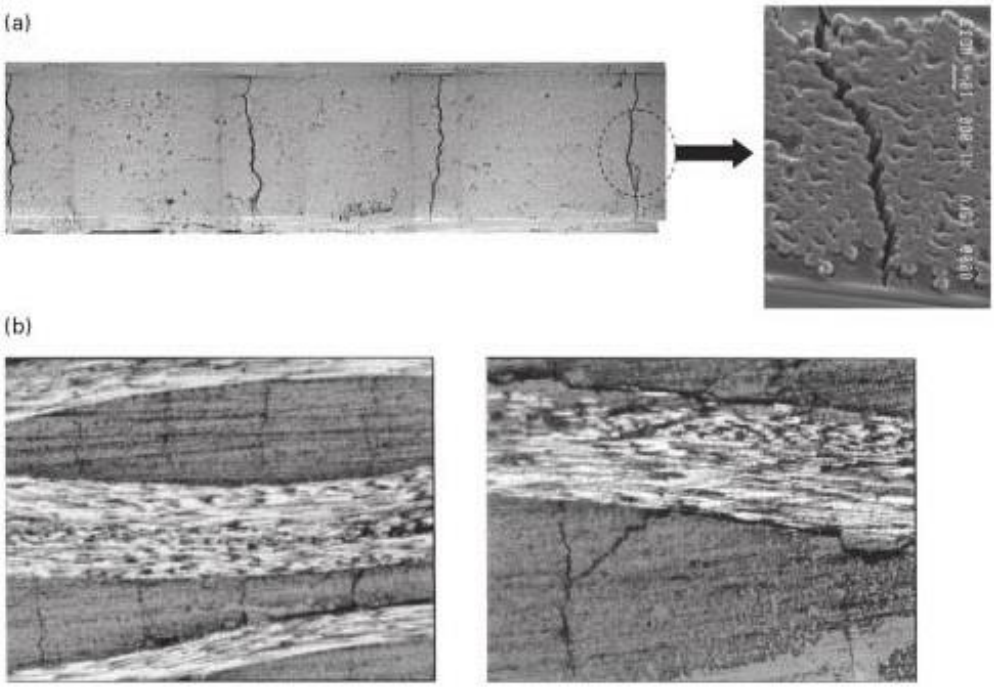

Figure 2.2 Examples of matrix crack in (a) continuous fiber and (b) woven fiber polymeric composites. [8]

2.1.2 Delamination

When local regions of composites deform differently (e.g., two neighboring plies) in response to the local loads, the resulting damage may lead to delamination. The delamination process, which is an important damage mode, is not independent of other damage. Most delamination is initiated by microcracking [10]. This delamination process can change the laminate strength, which doesn't generally happen in the case of microcracking, and fracture can be the end result of stress redistribution associated with delamination [11]. But delamination is a damage event, not a failure event in composite materials.

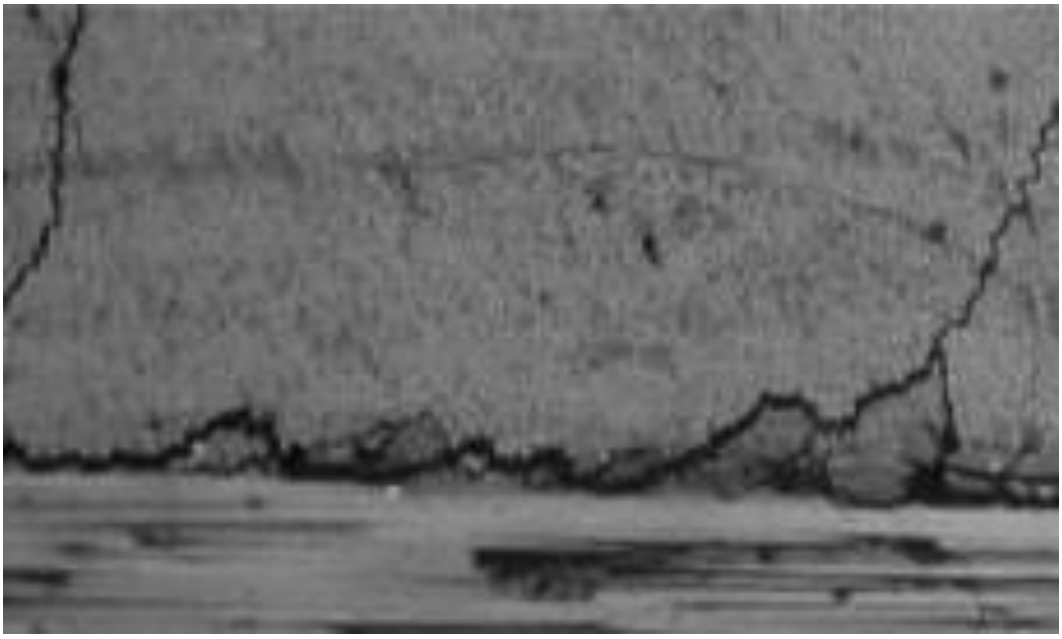

Figure 2.3 Interlaminar delamination crack formed due to joining of two adjacent matrix cracks in a fiber reinforced composite laminate [8]

2.1.3 Fiber Fracture:

Another damage mode, and generally a failure mode in structural composites, is fiber fracture. Fiber fracture is difficult to detect and studied less completely than any of the other damage modes. Fiber fracture is highly coupled to damage in fiber and matrix materials [12-14]. In woven composites, the interaction between fiber and matrix is complicated because the weft and wrap fibers are braided together.

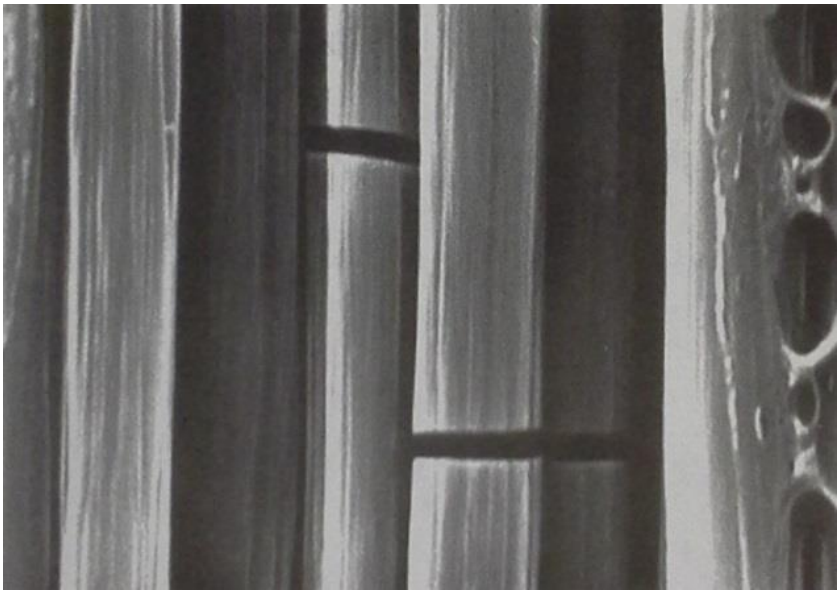

Figure 2.4 Adjacent fiber fractures in interior of carbon-epoxy composite.

Micro-buckling of fibers is another damage mode, but these effects are often neglected for woven composite materials.

Progressive failure in composite materials can be considered to be the statistical accumulation, and subsequent interaction between microdefects. During dynamic tensile loading, acceleration of the damage accumulation is rate dependent, which actually alters the ultimate strength, strain to failure, and energy dissipation capabilities [16-24].

The progressive failure nature of damage development under uniaxial loading of an off-axis woven structural composite specimen can be divided in four zones [25].

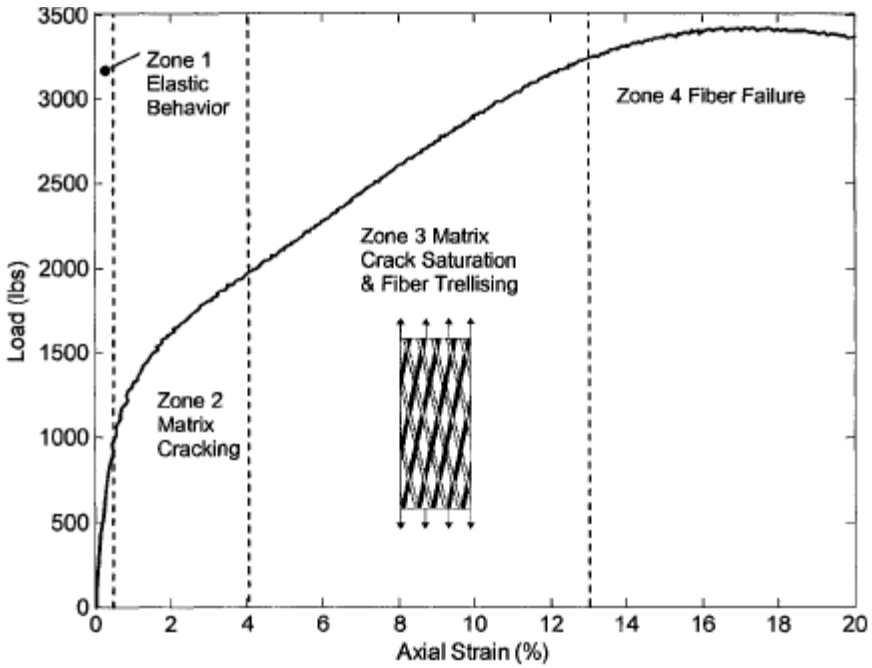

Figure 2.5 Off-axis Response of Woven Composite (45 Degree Tension) [25]

1. Zone 1: Elastic loading zone.

2. Zone 2: Matrix micro-cracking begins, and as the load increases, micro cracking also increases and the stress-strain behavior becomes non-linear.

3. Zone 3: Micro cracking reaches a saturation point, known as the 'characteristic damage state' [4]. After that, non-linearity due to the micro-cracking slows and trellising starts, which is dominated by rotation of the fibers. Fibers reorient towards the loading direction.

4. Zone 4: The final non-linearity is the likely result of statistically based fiber failure over a range of axial strain.

For fatigue samples, Talreja [26] also divided the life into 5 parts; the 1st part is dominated by matrix microcracking; the 2nd section involves crack bridging and interfacial debonding; in the 3rd phase delamination prevails; damage accumulation

accelerates in the 4th region which is dominated by fiber breaking and finally fracture occurs.

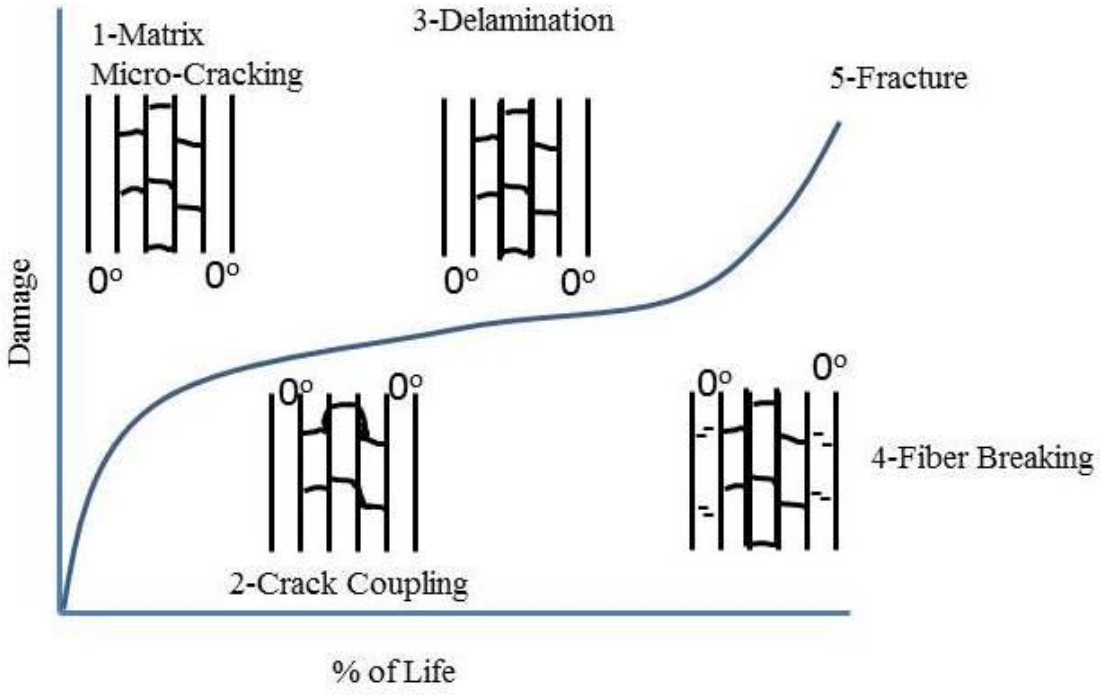

Figure 2.6: A plot of the typical growth of damage and reduction in stiffness and remaining strength throughout the life of the composite.

2.2 State of Art Damage Monitoring Techniques

There are many Non-destructive techniques used to detect the damage of composite materials, which is complicated in nature.

2.2.1 Ultrasonic, Scanning Acoustic Microscope and Acoustic Emission

Ultrasonic Testing (UT) and Acoustic Emission (AE) techniques are widely used NDT methods for composite defect detection [27-41]. In ultrasonic NDE, elastic waves propagate through the sample. Flaws/damage cause disturbances in the wave field which can be detected utilizing one the following measurements: time of flight (TOF; wave

transit or delay), path length, frequency, phase angle, amplitude, acoustic impedance, and angle of wave deflection (reflection and refraction) [42].

Though it has wide advantages and applicability, this method also has some limitations such as the requirement of point to point inspection, limited depth due to attenuation, limited interpretation due to a high variation of composite properties, low contrast due to high attenuation and scattering in composites, and slow methodology. And above all, it is an indirect method that cannot determine the type and orientation of the defects.

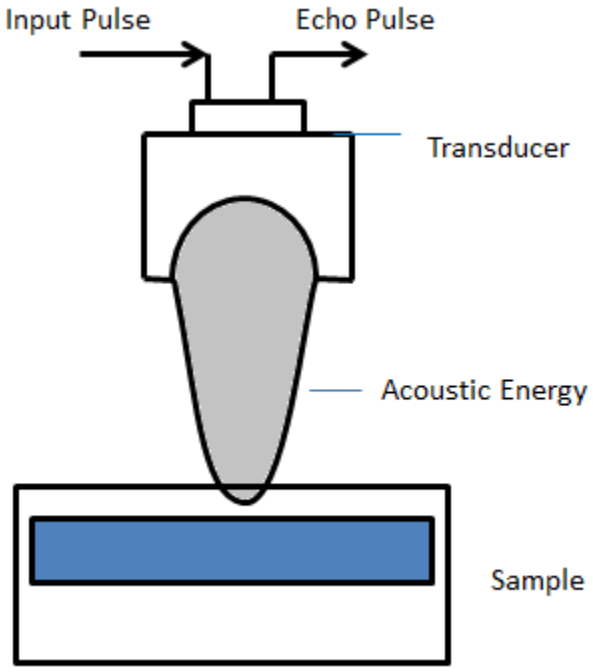

Figure 2.7 Schematic of SAM technique

Scanning Acoustic Microscopy (SAM) defect detection are high resolution ultrasonic imaging techniques that apply a range of frequencies from 30 MHZ to 3 GHz. Figure 2.7 is the schematic of the SAM technique most often used to detect the delamination of composite laminates [43-45].

Like ultrasonic NDT, SAM is limited by high attenuation and scattering of the signal. It cannot distinguish between delamination, interlaminar cracks, and initiation of cracks, matrix damage, or fiber fracture. With this technique it is not possible to follow the material state change progressively through the service life.

When a crack forms and grows, it releases energy which generates elastic waves that propagate outwards from the defect. AE is simply the detection and study of the transient elastic wave that originates from an energy release by the material defects. However, although Acoustic Emission (AE) is an old and well-established NDE method [27, 28, 30-32, 34, 41], it is not quantitative and cannot define the type of defects and location that cause the impulse. Due to the reflections, wave anisotropic propagation speeds depending on direction, and attenuation, the "triangulating" of damage in composite materials using AE signals is very complicated and difficult.

2.2.3 Electrical Resistance Method

Most NDE techniques require sensors on the surface of the composites or are non-contact methods that must have a clear view of the sample surface. But in electrical methods, most of the time, the composite system itself is used as the sensor. Detecting damage using electrical resistivity based on percolation methods is a well-known practice for damage detection in composite research [46-83].

Changes in capacitance and dissipation have also been observed [72] for CFRP through the thickness.

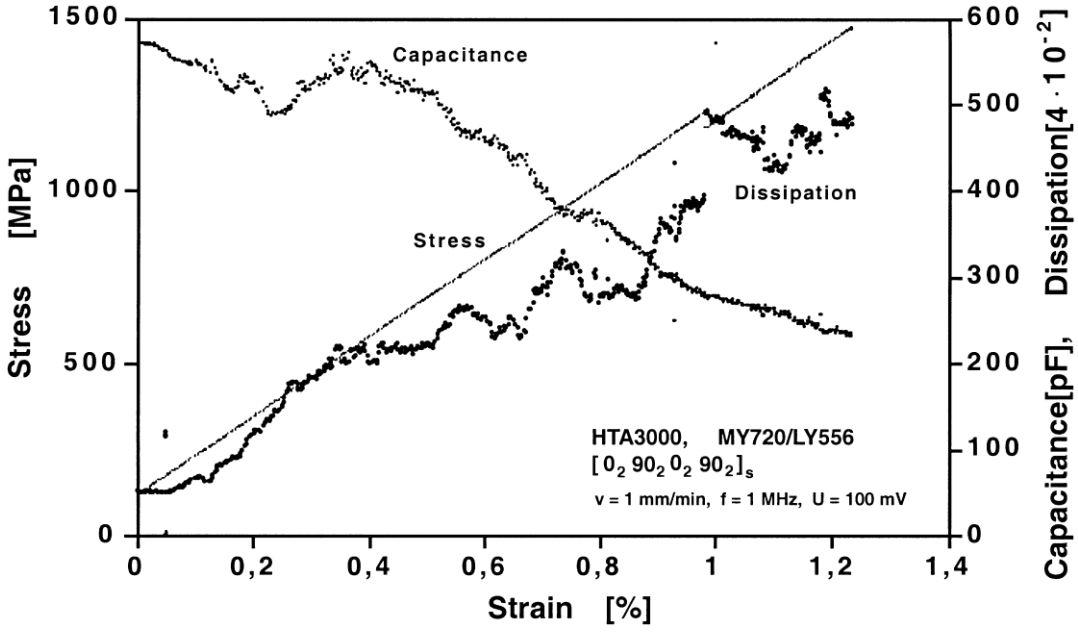

Figure 2.8: Tensile test of a cross-ply laminate, showing the stress/strain curve and dependent capacitance and dielectric dissipation (at 1 MHz and 100 mV) of a CFRP specimen.

Irving et al. [83] has studied electrical resistance changes for both static and fatigue testing of CFRP.

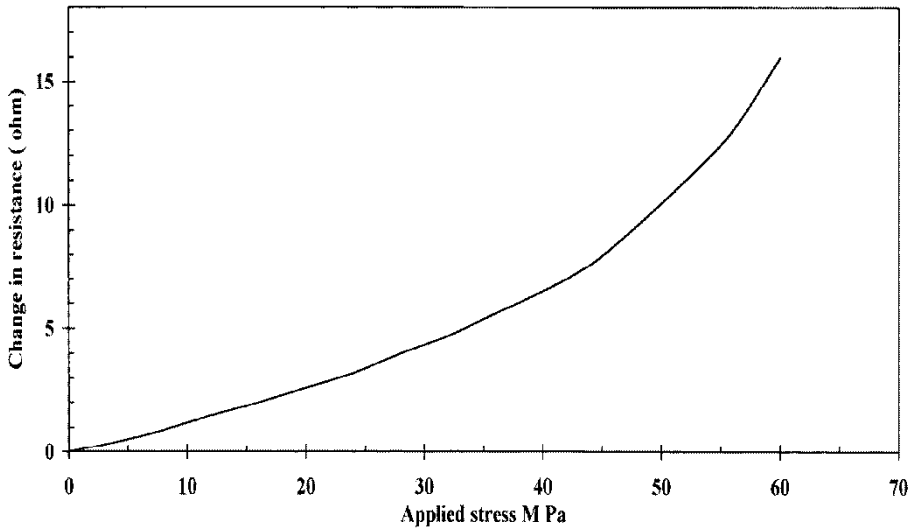

Figure 2.9: Change in resistance for 90° samples [83].

Although electrical methods have the potential to measure the damage state during the service life of the composite materials, they can't give quantitative information about the defects, orientation of the flaws, crack density, and local connectivity, or information about the damage mode.

2.3 Broadband dielectric spectroscopy (BbDS)

Broadband dielectric spectroscopy is the interaction of electromagnetic waves with matter in the frequency range from a lower value of 10^{-6} Hz to a higher frequency of 10^{12} Hz. This dynamic range contains information about the molecular and collective dipolar fluctuation; charge transport and polarization effects occur at inner and outer boundaries in the form of different dielectric properties of the material under study. Figure 2.10 shows the effect of different charge displacement mechanisms on dielectric response and their corresponding effective frequency range.

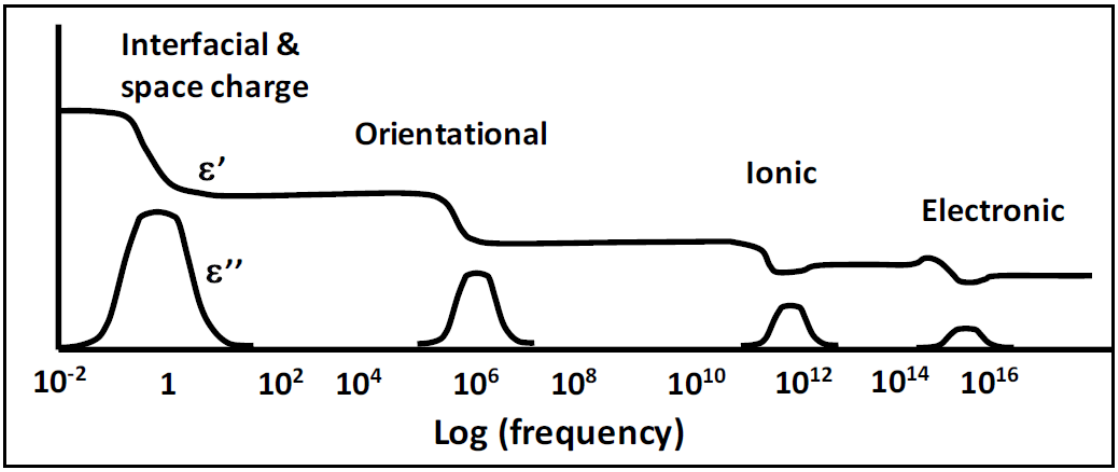

Figure 2.10 Dielectric responses of material constituents at broad band frequency ranges.

Hence broadband dielectric spectroscopy can be used as a useful tool to obtain a wealth of information on the dynamics of bound dipoles and mobile charge carriers

depending on the details of the molecular system and the microstructure in heterogeneous materials.

2.3.1 Polarization in dielectrics

Maxwell's equations describe the interaction between electromagnetic fields and matter [84-85].

$$\nabla.\vec{\boldsymbol{D}} = \rho \qquad (2-1)$$

$$\nabla \times \vec{\boldsymbol{H}} = \vec{j} + \frac{\partial \vec{\boldsymbol{D}}}{\partial t} \qquad (2-2)$$

$$\nabla \times \vec{\boldsymbol{E}} + \frac{\partial \vec{\boldsymbol{B}}}{\partial t} = 0 \qquad (2-3)$$

$$\nabla.\vec{\boldsymbol{B}} = 0 \qquad (2-4)$$

Here $\vec{\boldsymbol{D}}$ is the dielectric displacement, ρ is the charge density, $\vec{\boldsymbol{H}}$ magnetic field, $\vec{\boldsymbol{E}}$ electric field, $\vec{\boldsymbol{B}}$ magnetic induction and $\vec{j}$ is the ohmic current density. In addition to Maxwell's equations, the field must satisfy continuity equations based on the charge density ρ and current density $\vec{j}$ which can be expressed as follows

$$\nabla.\vec{j} + \frac{\partial \rho}{\partial t} = 0 \qquad (2-5)$$

The interrelation between the dielectric displacement $\vec{\boldsymbol{D}}$ and electric field $\vec{\boldsymbol{E}}$ can be expressed as

$$\vec{\boldsymbol{D}} = \varepsilon_0 \vec{\boldsymbol{E}} + \vec{\boldsymbol{P}} \qquad (2-6)$$

for linear materials. And polarization can be related to the charge density when no external source is present by the following equation

$$\nabla.\vec{\boldsymbol{P}} = -\rho \qquad (2-7)$$

For a linear relationship between the dielectric displacement $\vec{\boldsymbol{D}}$ and electric field $\vec{\boldsymbol{E}}$ the proportionality constant ε can be used to express

$$\vec{\boldsymbol{D}} = \varepsilon\varepsilon_0\vec{\boldsymbol{E}} \qquad (2-8)$$

Here the constant ε is called the permittivity of the material which describes the dielectric behavior. When the Polarization is $\vec{\boldsymbol{P}}$ is taken into consideration using (2-6) and (2-8) we obtain

$$\vec{\boldsymbol{P}} = \chi\varepsilon_0\vec{\boldsymbol{E}} \equiv \varepsilon_0(\varepsilon - 1)\vec{\boldsymbol{E}} \qquad (2-9)$$

Here χ is the polarization coefficient known as the dielectric susceptibility.

Several polarization mechanisms can arise in a material system, i.e. electronic, ionic (molecular), atomic, dipolar (orientational), interfacial polarizations and polarization caused by the hopping charge [86].

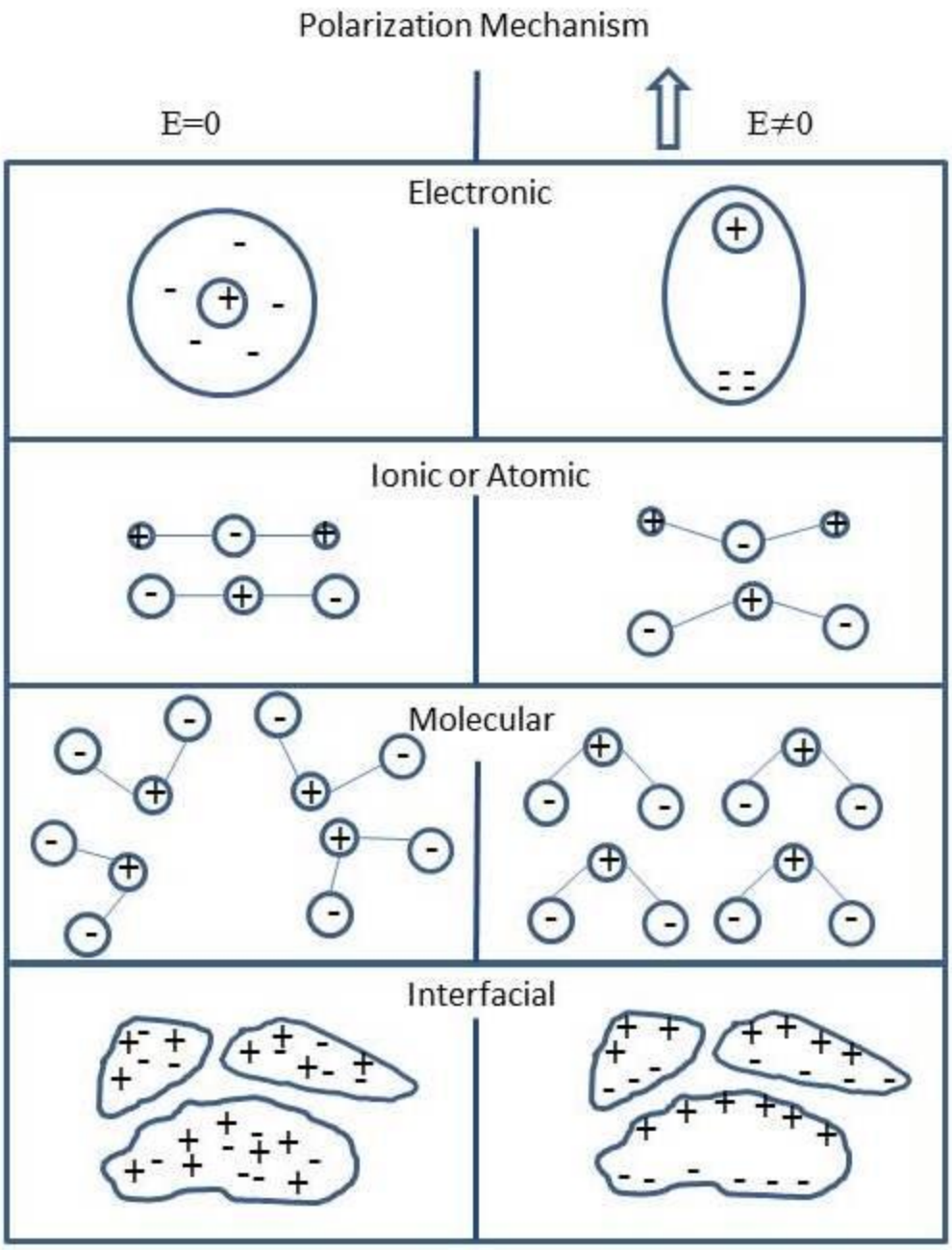

Figure 2.11 Basic Polarization mechanisms in the material.

Electronic, atomic and ionic polarization happens very quickly and is called instantaneous polarization, $\mathbf{P}_o$. It is not possible to store an infinite amount of electrical energy in a dielectric material, so longer- time polarization should be finite, $\mathbf{P}_{(t\to\infty)} = \mathbf{P}_s$.

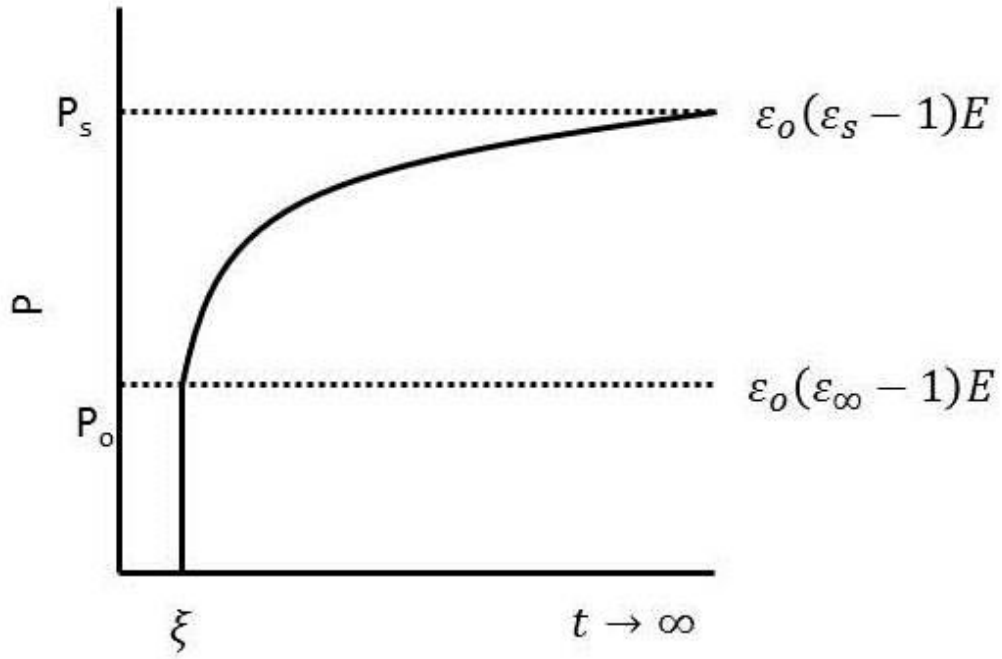

Figure 2.12 Time dependence of polarization, P, when a constant electric field is applied at $t = \xi$

Figure 2.12 shows polarization of a materials system for a constant-step electric field, $\mathbf{E} = \mathbf{E}_o\hat{n}$, applied at $t = \xi$. The dielectric constant of the materials at time $t = \xi$ is instantaneous permittivity ε_∞ and at $t \to \infty$ is the static permittivity ε_s. The time dependent polarization, $\mathbf{P}(t)$, is

$$\mathbf{P}(t) = \varepsilon_o(\varepsilon_\infty - 1)E(t) + \varepsilon_o \int_{-\infty}^{t} \mathrm{f}(t-\xi)\mathbf{E}(\xi)d\xi \qquad 2-10$$

Here f(t) is intrinsic material property and called dielectric response function. For harmonic electric fields from equation (2-6) and (2-10) we can get the complex permittivity of the material.

$$\varepsilon^*(\omega) = \varepsilon_\infty + \int_0^\infty \mathrm{f}(t)\mathrm{e}^{-\mathrm{i}\omega\mathrm{t}}dt \qquad 2-11$$

So the complex dielectric susceptibility is,

$$\chi(\omega) = \varepsilon^*(\omega) - \varepsilon_\infty = \int_0^\infty \mathrm{f}(t)\mathrm{e}^{-\mathrm{i}\omega\mathrm{t}}dt \qquad 2-12$$

2.3.2 Dielectric relaxation:

Maxwell's equations describe the complex permittivity ε* as a time or frequency dependent property if time dependent processes take place within the sample. This time or frequency dependency can be attributed to several causes.

Relaxation phenomena are typically related to the molecular fluctuation of dipoles due to their motion in a potential field. Moreover, the drift motion of mobile charge carriers (electrons, ions or charged defects) causes conductive contributions to the dielectric response. In general, time dependent processes within the materials create fluctuations in the applied electrical field E(t) and the resulting dielectric displacement D(t).

The dependence of the complex dielectric function ε*(ω) on the angular frequency ω of the outer electric field and temperature can generally be attributed to the following

1) Microscopic fluctuations of molecular dipoles [87].

2) Propagation of mobile charge carriers by translational diffusion of electrons, holes or ions.

3) The separation of charges at interfaces which gives rise to an additional polarization. The latter can take place at inner dielectric boundary layers (Maxwell/Wagner/Sillars-polarization) [88-89] on a mesoscopic scale and/or at the external electrodes contacting the sample (electrode polarization) on a macroscopic scale. The contribution to the loss for this type of polarization can be orders of magnitude larger than the contributions from molecular fluctuation.

Each of the above mentioned processes has specific features in the frequency and temperature dependence of the real and imaginary part of their complex dielectric function. It is the objective of the present work to analyze, to separate, and to quantify their different contributions to the dielectric spectra for our materials of interest. [90]

With gradually increasing frequency, relaxation processes are characterized by some common features in the real and imaginary part of the complex dielectric function, which can be written as

$$\varepsilon^*(\omega) = \varepsilon'(\omega) - i\varepsilon''(\omega) \qquad (2-13)$$

For the real part ε'(ω) of the complex dielectric function there is a step like decrease with increasing frequency and the imaginary part ε"(ω) is typically characterized by a peak.

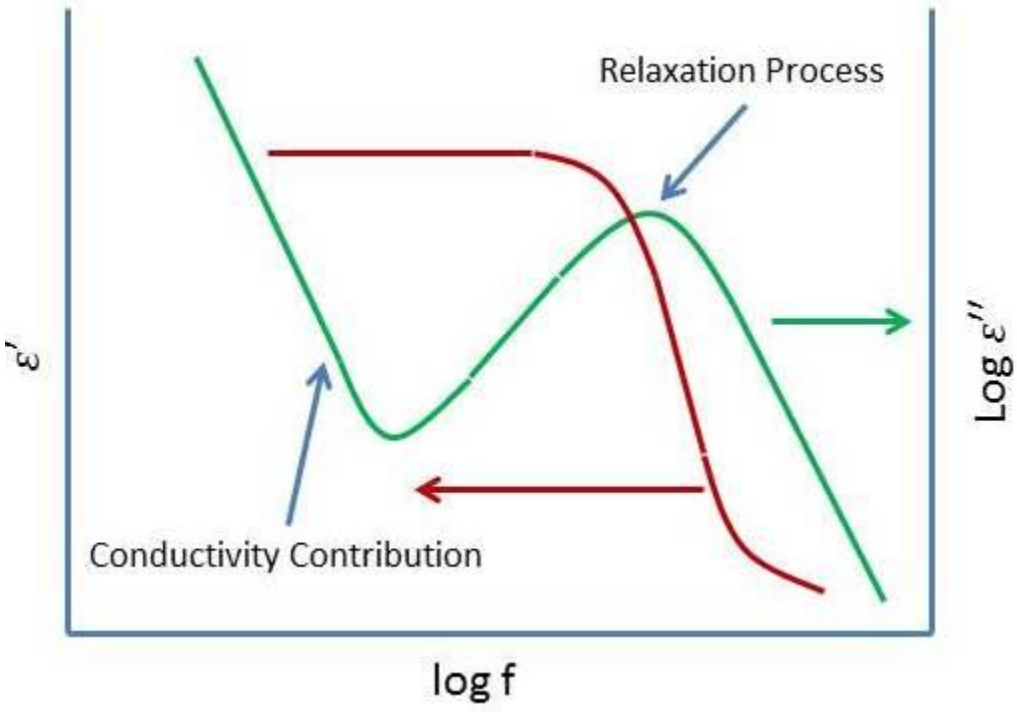

Figure 2.13: Real permittivity ε'(ω) (solid line) and imaginary permittivity ε"(ω) of the complex dielectric function for relaxation process of an ohmic conductor.

By contrast, conduction phenomena show an increase of the imaginary part of the dielectric function with decreasing frequency. In Figure 2.13 the permittivity behavior of ohmic and ionic conductive material is shown for variable frequency. For purely ohmic conduction, the real part of ε is independent of frequency while for ionic conduction or polarization effects (at inner boundaries of external electrodes) the real part of epsilon increases with decreasing frequency.

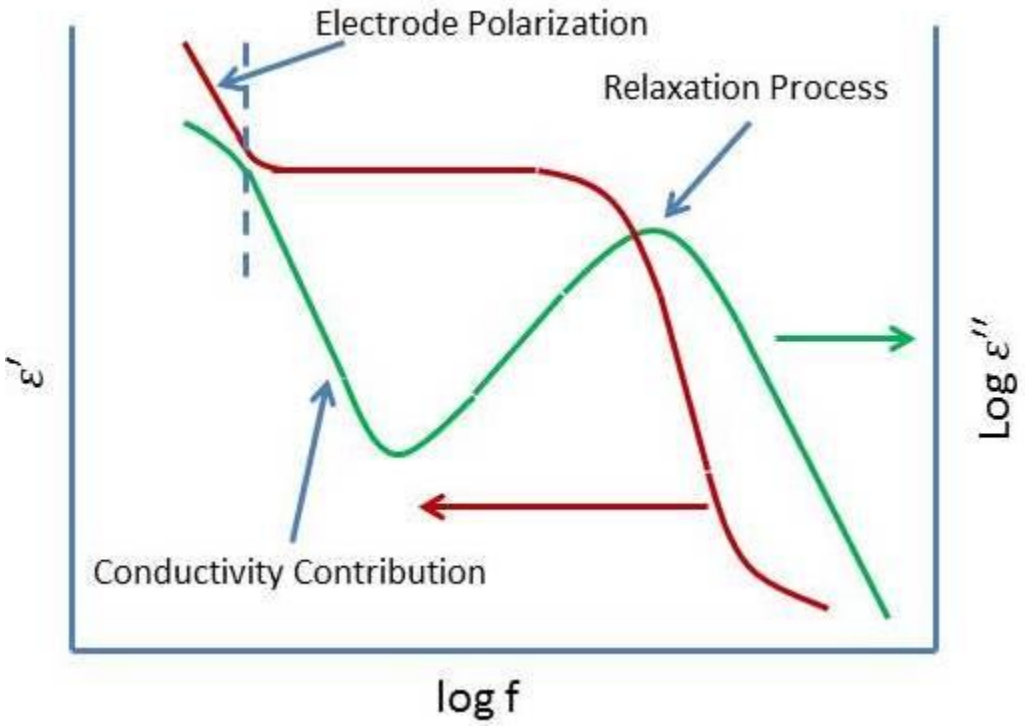

Figure: 2.14 Real permittivity ε'(ω) (solid line) and imaginary permittivity ε"(ω) of the complex dielectric function for relaxation process of an ionic conductive material.

Other useful alternative representations of dielectric properties of the material are the complex conductivity σ^* and complex electric modulus M*. They emphasize different aspects of polarization and charge transport for different frequency range. The dependence of real conductivity on frequency and temperature or charge carrier concentration has certain features that can be used to effect time temperature

superposition and to scale the normalized conductivity with respect to normalized frequency to identify the effects of different parameters on charge transport mechanisms. [87, 90]

2.3.3 Dielectric Study of Composite Materials:

Fiber reinforced composite materials are universally dielectric. They are poor and imperfect conductors that trap charge at interfaces and micro-boundaries, defects, and micro-cracks, and they typically conduct with several mechanisms. Heterogeneous material systems have many micro-nano interfaces and when they degrade, new "phases" are created. So materials of different electrical properties contact each other, and with degradation, the nature of the contact changes. In such a material system, polarization is typically an interfacial effect that is due to the build-up of charge on the interfaces. The dielectric relaxation due to interfacial polarization provides information about the heterogeneous structure and the electrical properties of the constituent components. The number of dielectric relaxations expected in heterogeneous systems depends not only on the number of different interfaces but also on the shape of the inclusions and their orientation relative to the vector direction of the applied field. In practice, however, all relaxations predicted are not observed because of the limited frequency range and sensitivity of measurements.

Abry et al. examined the dielectric properties of $[+45;-45]_{8s}$ laminates and found non-linearity in the complex impedance response Figure 2.15 and Figure 2.16[91].

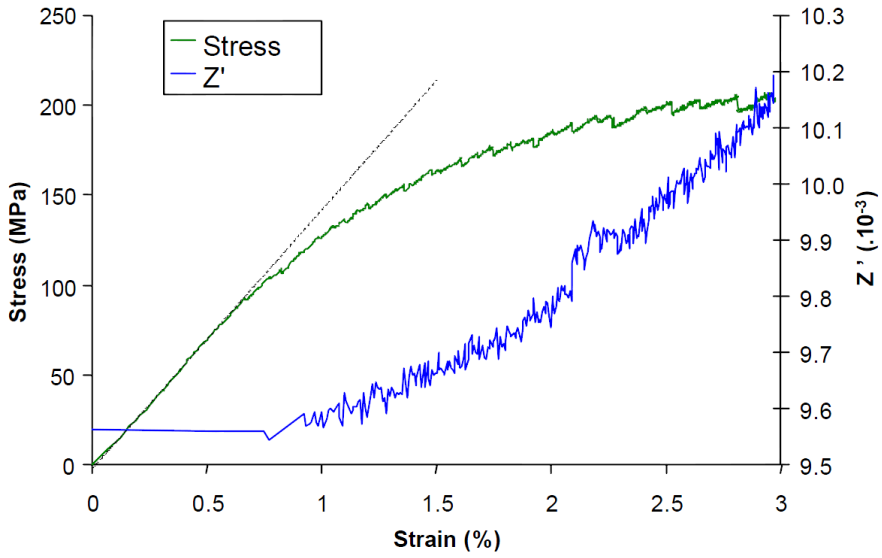

Figure 2.15: Changes in stress and in Z' as a function of strain during a quasi-static loading

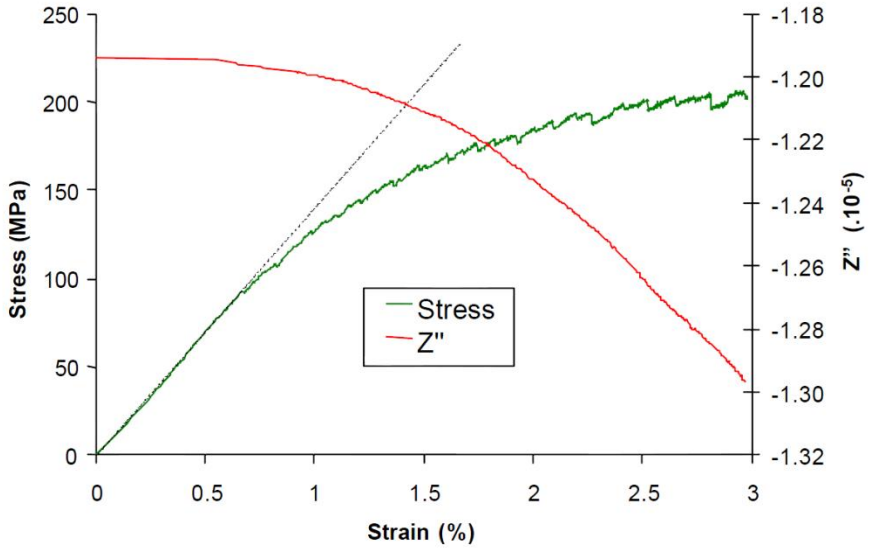

Figure 2.16: Changes in stress and in Z" as a function of strain during a quasi-static loading

Fazzino, et al. studied polymer based composites and showed that they develop micro cracking due to mechanical loading, which changed their dielectric response dramatically and definitively [92, 93]. They used end-load bending for fatigue loading

which actually caused surface-initiated damage. The Samples were soaked in 5M NaCl solution and this ionic solution filled the micro cracks and penetrated through the surface to the interior of the sample. The response was very sensitive to the local morphology (including the topological connectivity) of the dielectric dispersed phase, e.g., the micro cracks in this case.

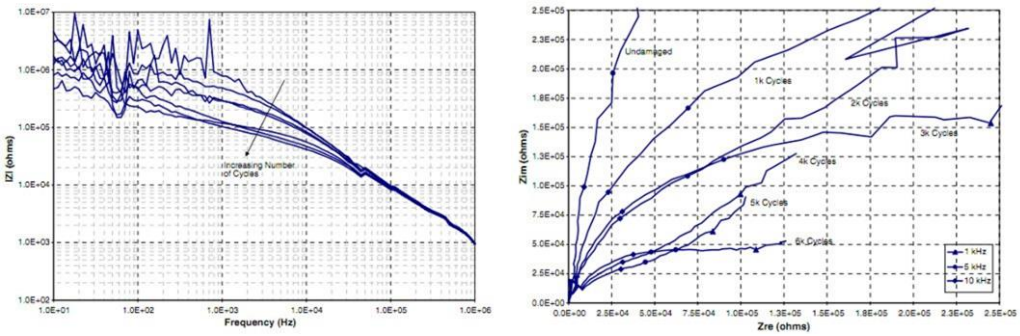

Figure 2.17: As damage increases, the Bode plot will become more level at lower frequencies. The Nyquist plot shows a decrease in slope as damage grows.

Dielectric responses gave some interesting outcomes for that special situation, but more investigation is needed to identify the damage and to predict the fracture events based on the dielectric properties of the material system.

CHAPTER 3 EXPERIMENTAL FACILITIES

In-situ experimental measurements of dielectric properties were achieved by coincident use of a Novocontrol dielectric spectroscopy unit and an MTS servohydraulic test machine. The Novocontrol unit was employed to measure the dielectric properties of the material system both at room and high temperature thermal loading using a Probostat thermal assembly. An MTS Landmark™ system was used for both quasi-static and cyclic loading of the composite sample while coupled with the Novocontrol unit by a special set-up constructed in our laboratories. An Xradia MicroXCT-400 X-ray tomography unit was used to visualize the internal details.

3.1 Broadband Dielectric Measurement

3.1.1 Novocontrol^{TM} System

The dielectric impedance spectroscopy system consists of a Novotherm-HT high temperature control system with temperature ranges from ambient up to 1200˚C with 0.1˚C resolution. The system consists of a Novotherm-HT temperature controller, a furnace and a ceramic sample cell with movable holder for the Probostat, and an Alpha analyzer for impedance analysis. The specifications of the Novocontrol^{TM} system are as follows:

Frequency	: 3μHz-20MHz
Phase accuracy	: 0.002˚ or tanδ accuracy $3X10^{-5}$
Impedance range	: $10^{-3}\Omega$-$10^{15}\Omega$
Novotherm- HT	: Ambient to 1200˚C

Any sequence of time, temperature and DC-bias can be used. Figure 3.1 is the schematic diagram of the Novocontrol^{TM} setup.

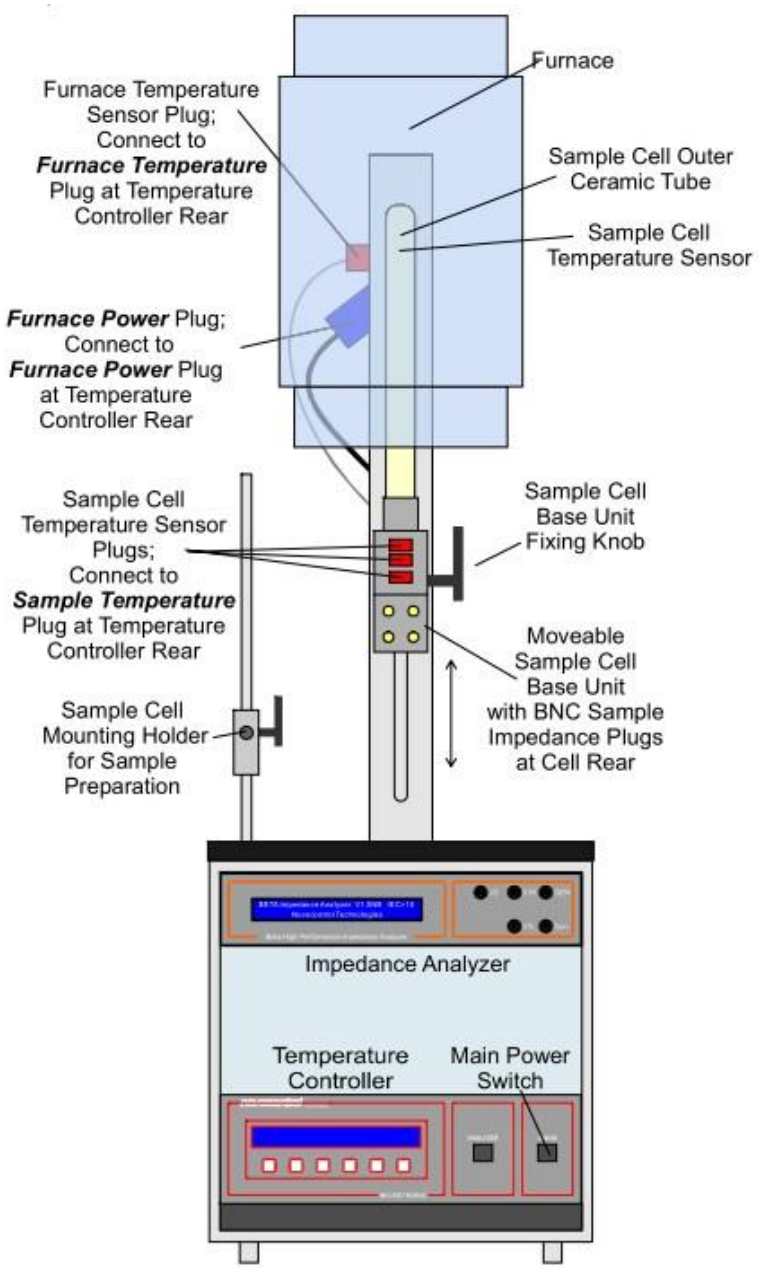

Figure 3.1 Novocontrol^{TM} system

3.1.2 Alpha analyzer:

The alpha analyzer measures the complex dielectric, conductivity and impedance properties of test materials as a function of frequency of the applied electric field with high precision. It is especially optimized for dielectric materials with high impedance and low loss factors over a broad frequency range, but can accurately measure highly conductive materials with low impedance, as well.

3.1.3 Principles of Dielectric Measurement in the NOVOCONTRL™:

The sample material is usually mounted in a sample cell between two electrodes forming a sample capacitor shown in figure 3.2.

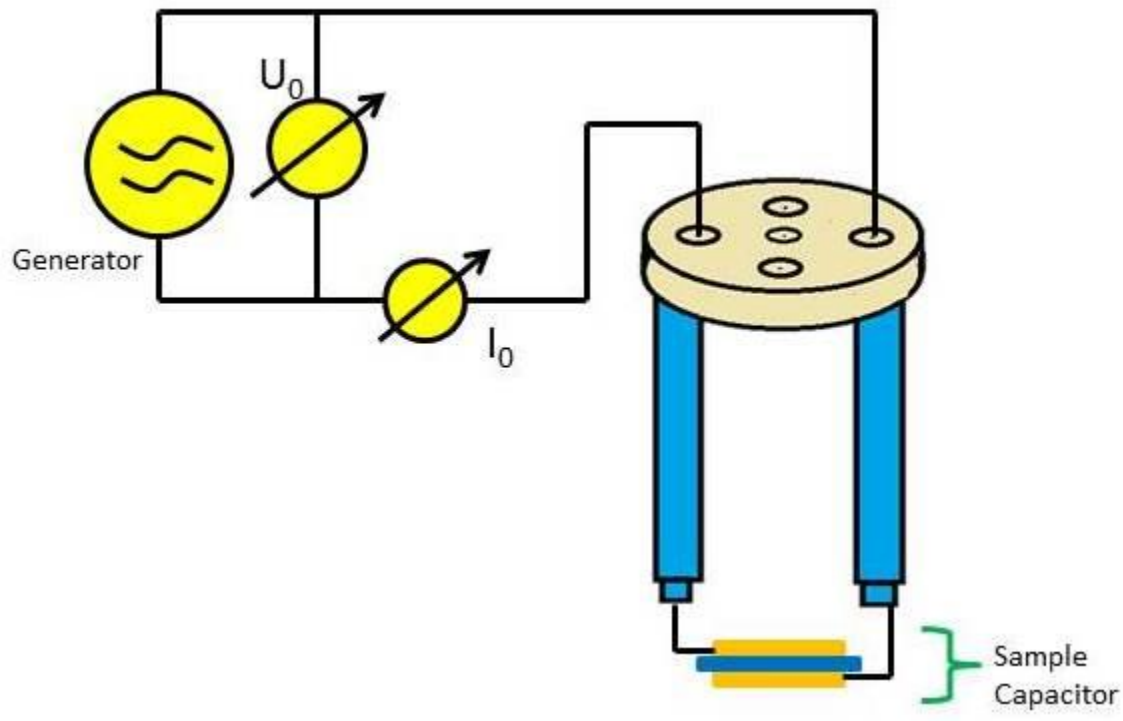

Figure 3.2 Principle of a dielectric or impedance measurement.

A voltage U_0 with a fixed frequency $\frac{\omega}{2\pi}$ is applied to the sample capacitor. U_0 causes a current I_0 at the same frequency in the sample. In addition, there will

generally be a phase shift between current and voltage described by the phase angle φ shown in figure 3.3.

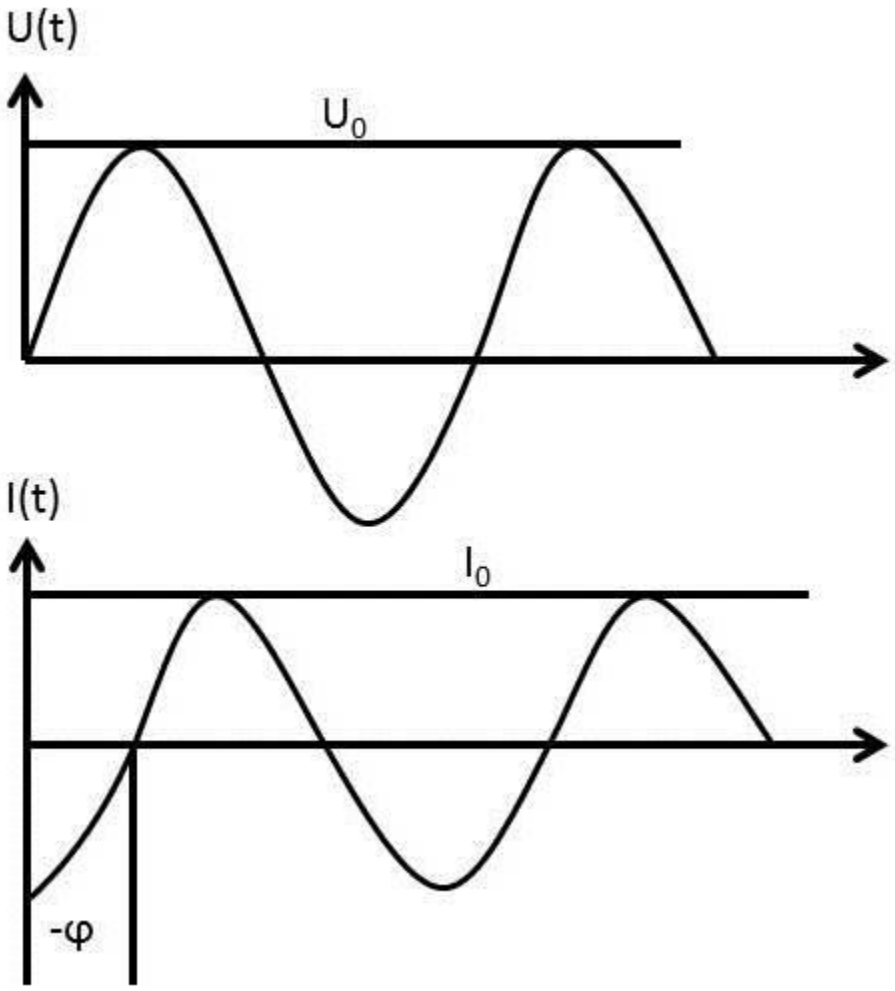

Figure 3.3 Amplitude and phase relations between voltage and current of a sample capacitor for electric measurements.

The ratio between U_0 and I_0 and the phase angle φ are determined by the sample material electric properties (permittivity and conductivity) and by the sample geometry. So the appropriate relations in complex notation can be expressed as

$$U(t) = U_0 \cos(\omega t) = Re(U^* \exp(i\omega t)) \qquad (3-1)$$

$$I(t) = I_0 \cos(\omega t + \varphi) = Re(I^* \exp(i\omega t)) \qquad (3-2)$$

With

$$U^* = U_0 \qquad (3-3)$$

and

$$I^* = I' + iI'' \qquad (3-4)$$

$$I_0 = \sqrt{I'^2 + I''^2} \qquad (3-5)$$

$$\tan(\varphi) = \frac{I''}{I'} \qquad (3-6)$$

For a sample with linear electromagnetic response, the measured impedance of the sample capacitor

$$Z^* = Z' + iZ'' = \frac{U^*}{I^*} \qquad (3-7)$$

And the imaginary permittivity can be calculated by

$$\varepsilon^*(\omega) = \varepsilon' - i\varepsilon'' = \frac{-i}{\omega Z^*(\omega)} . \frac{1}{C_0} \qquad (3-8)$$

Here C_0 is the capacity of the empty sample capacitor.

The specific conductivity is related to the dielectric function by

$$\sigma^*(\omega) = \sigma' - i\sigma'' = i2\pi f \varepsilon_0(\varepsilon^* - 1) \qquad (3-9)$$

And Electric Modulus can be calculated by

$$M^*(\omega) = \frac{1}{\varepsilon^*(\omega)} \qquad (3-10)$$

3.1.4 ProboStat™ Assembly

The ProboStat™ is a test cell that enables measurements of electrical properties, transport parameters, and kinetics of materials, solid/gas interfaces and electrodes under controlled atmospheres at high temperatures up to 1600ºC. Figure 3.4 shows the sample station and the electrode and gas supply assembly of the Probostat. The sample under test rests on a 50 cm long support tube of alumina, inside a closed outer tube of alumina or

silica. The sample can be contacted with 2, 3 or 4 electrodes of platinum. A spring-loaded alumina assembly holds the sample and electrodes in place. Sixteen electrical feed-throughs on the base shown in figure 3.5 allow use of 4 shielded electrode leads, surface guard, and up to three thermocouples. Electrical connections are made via coax cables suitable for standard impedance spectrometer connectors, and standard thermocouple compensation cables. Gases can be fed in single or dual chamber modes directly onto or from electrodes, allowing measurements under controlled atmospheres, transport number measurements with gradients, and testing of fuel cell, pump, and sensor components. Gas supply is via Swagelok quick-connects.

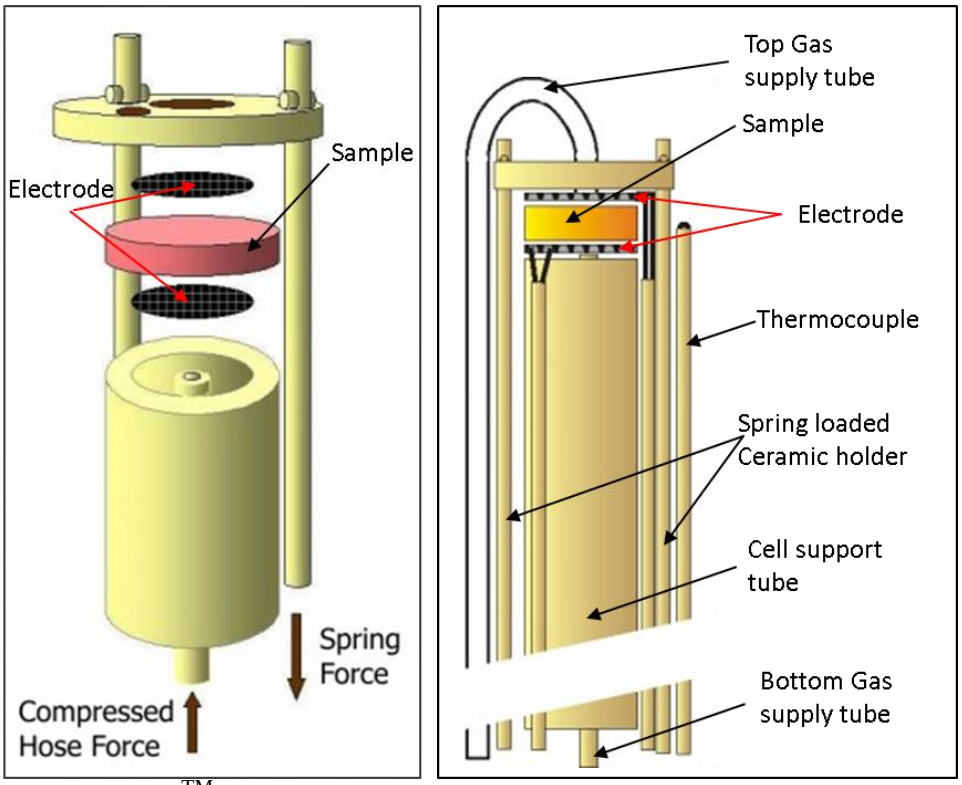

Figure 3.4 Probostat™ spring loads and regular 2-electrode 4-wire setup with dual gas supplies and thermocouple

Figure 3.5 Probostat™ base unit with feedthroughs

3.2 Mechanical Response Measurement

MTS™ is a leader of servo-hydraulic load frame technology. The MTS Landmark™ platform enables the repeatability and the flexibility one needs to perform a full spectrum of static and dynamic material testing.

Figure 3.6 MTS Landmark™ and dielectric measurement set-up

3.3 Visual Inspection

Microfocused X-ray Computed Tomography MicroXCT) was used to investigate the material state change visually, and for this purpose an Xradia MicroXCT-400 machine was utilized.

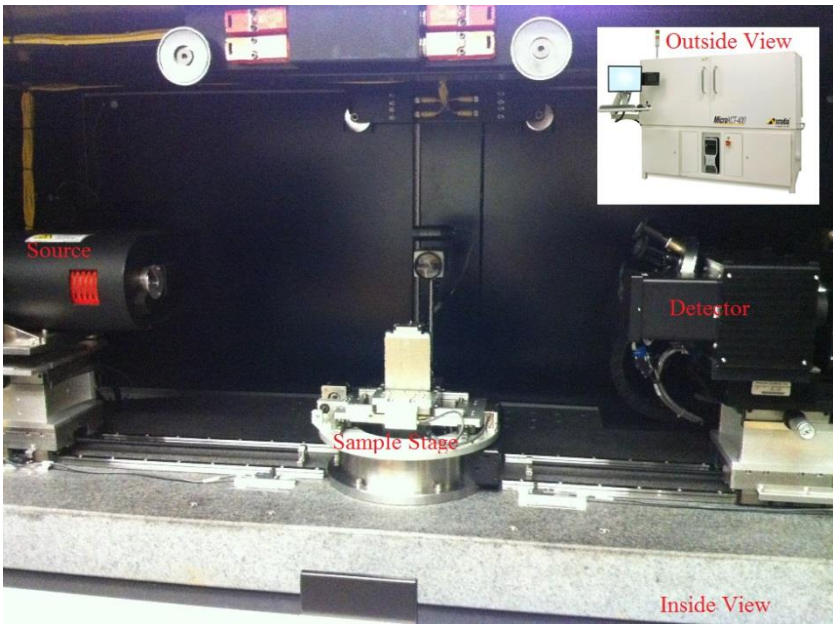

Figure 3.7 Xradia MicroXCT-400 Machine

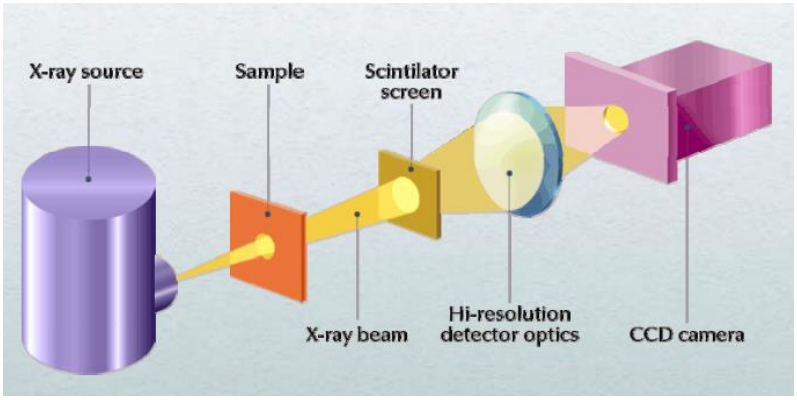

Figure 3.8 Basic Principle of MicroXCT

X-ray energy is generated by an x-ray source and penetrates through the materials; the sample absorbs certain amounts and types of the x-ray energy depending on the sample density, atomic number, and thickness and attenuation number. X-ray energies which escape from the sample are captured by a detector for different sample rotations. Later projections which are captured by the detector are used to process a 3D image reconstruction of the sample region.

CHAPTER 4 DIELECTRIC STUDY OF SOFC COMPOSITE MATERIALS

In the absence of electrochemistry, the effect of different porous microstructures (i.e., porosity, connectivity, distribution and geometry) of SOFC composite electrodes was studied to observe the electromagnetic response in the time and frequency domain at different operating temperatures [94-95]. The specimens were 20 mm diameter button cells (8%YSZ based cells manufactured by EnrG Inc.) with a bi-electrode supported structure or "BSC" (as pioneered by NASA) [96-97]. This study provided a model material for development of the test method and identification of internal defects.

The key feature of the design concept is the symmetrical cell, which is made by supporting the thin electrolyte on both sides with a porous YSZ support structure [96-97]. The graded porosity provides the smallest pores at the electrode/electrolyte interface, creating the maximum amount of active interfacial area or triple-phase boundary once the active electrode materials are infiltrated.

4.1 Effect of morphology difference in actual SOFC active and inactive zone

As shown in Figure. 4.1, after operating the SOFC for 8 hrs., Broadband Dielectric Spectroscopy (BbDS) measurements were carried out on areas near and far away from the active region of a SOFC button cell. The impedance was measured in the absence of any electrochemical processes at room temperature. It was postulated that material deterioration contributed to the formation of new morphological variations inside the SOFC structure which caused the variations in impedance response. By implementing 3D X-ray tomography, the micro-structural differences were visualized. A

representative virtual section of the electrolyte is also shown in the figure. There is visible material damage, i.e. a crack on the electrolyte near the electrolyte-electrode interface.

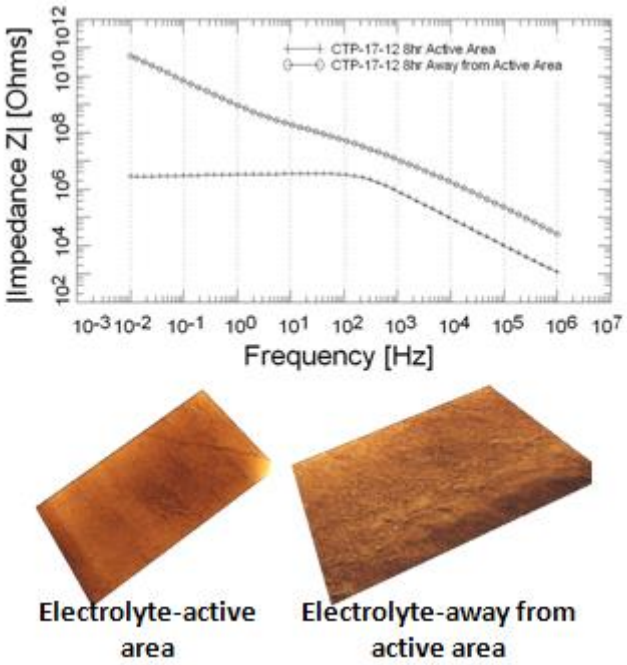

Figure 4.1 Broadband dielectric spectroscopy response of active and away from active regions of an SOFC button cell after 8 hr of operation (measured at room temperature)

4.2 Effect of porous morphology (% solid loading) difference in SOFC material response at high temperature:

The porosity of the electrode material was varied by using different solid loading during processing of freeze-cast SOFC button cells to study its effect on the conductivity. Figure 4.2 shows two different porous morphologies (TTP1-B has 40% solid in freeze asting or 67% porosity compared to 50% solid loading in TTP1-C or 61% porosity) contributed to the different dielectric response, and change in impedance, at 800C.

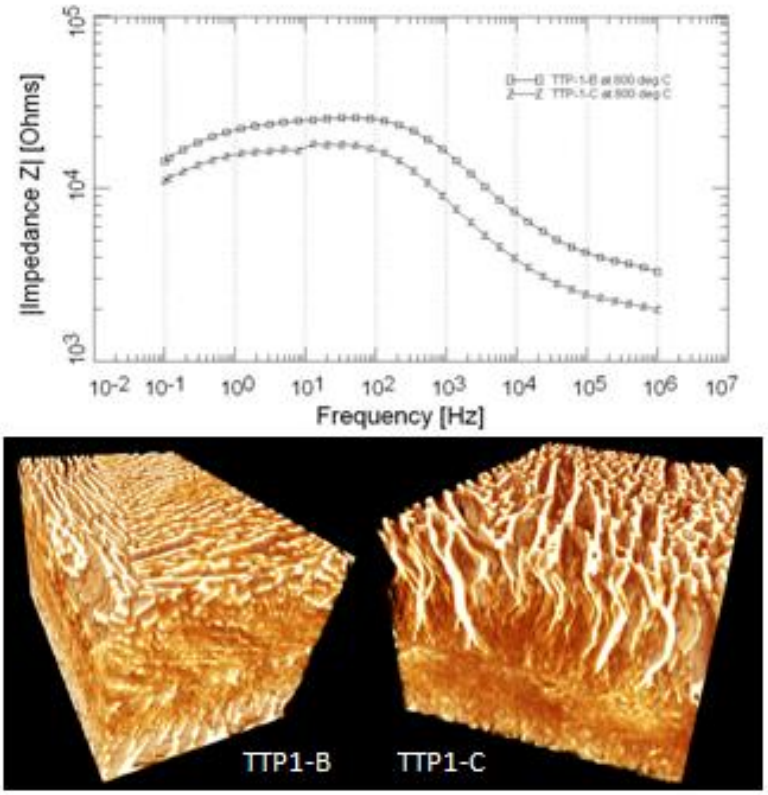

Figure 4.2: BbDS response of two different morphology at 800C

4.3 Effect of geometric variations (cellular to lamellar) in morphology of SOFC material:

In this experiment, morphology of single layers (freeze-cast tape) of electrode material (YSZ) were varied systematically. As shown in Figure 4.2, the geometry of porous microstructure was generally cellular except where it was slightly lamellar at the nucleation or electrolyte side in the TTP8A specimen, but specimen TTP8B had a more uniform lamellar structure. On the other hand, TTP8C featureda lamellar structure which varied from a dense microstructure at the electrode side to large pores at the other side. The corresponding variation of conductivity at 800C has been plotted as a function of AC

frequency (Figure 4.3). This figure shows conductivity variation due to change in geometry of the electrode microstructure.

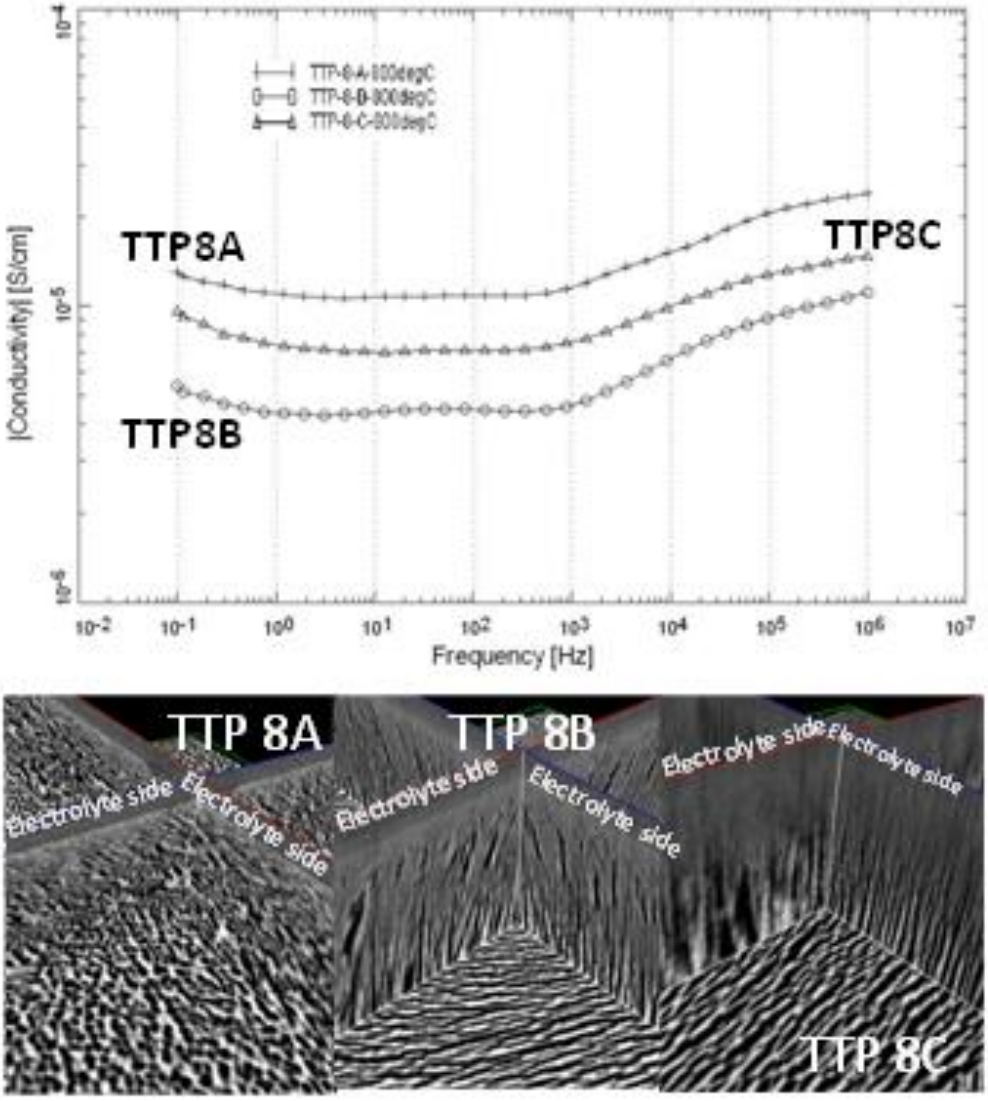

Figure 4.3: Difference in impedance in different electrode geometries (cellular vs. lamellar)

4.4 Effect of Asymmetry in morphology of SOFC material:

In this experiment we compared a fairly homogeneous cellular morphology (TTP8A) with an inhomogeneous morphology TTP9C (dense dendytric porous structure near electrolyte is very different from the other side with larger lamellar pores). Figure 4.4 is a representative plot of impedance magnitude vs. frequency, and it shows a significant variation due to the stated micro-structural change.

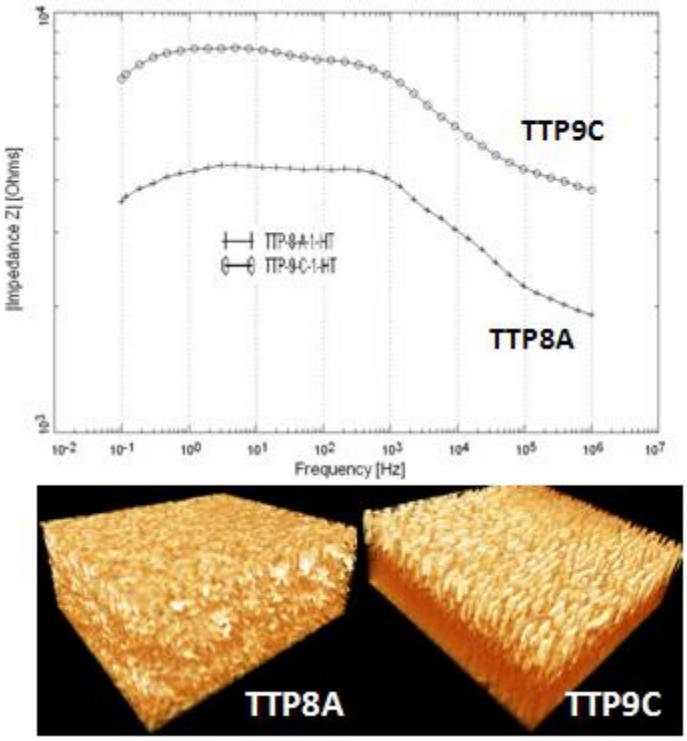

Figure 4.4 : Asymmetric variation of morphology from electrolyte side to the other

4.5 Effect of temperature and thermal cycles on the BbDS response of SOFC material:

In these experiments, SOFC button cells of two different porosities were heated to 800C and cooled to room temperature. BbDS characteristics were recorded in-situ. Figure 4.5 indicates that BbDS measurements capture the expected increase in

conductivity (decreasing impedance) with the increase in temperature. At the most fundamental level, this is very interesting because, in the absence of electrochemistry, the response from the material clearly demonstrates a polarization process associated with the material. The most interesting aspect of this study (Figure 4.5b) is that the impedance response changes differently after the first cycle of heating-cooling. Although between the 2nd and 3rd cycle, the difference in response is more narrow, the large drop in conductivity at the first thermal cycle is noteworthy.

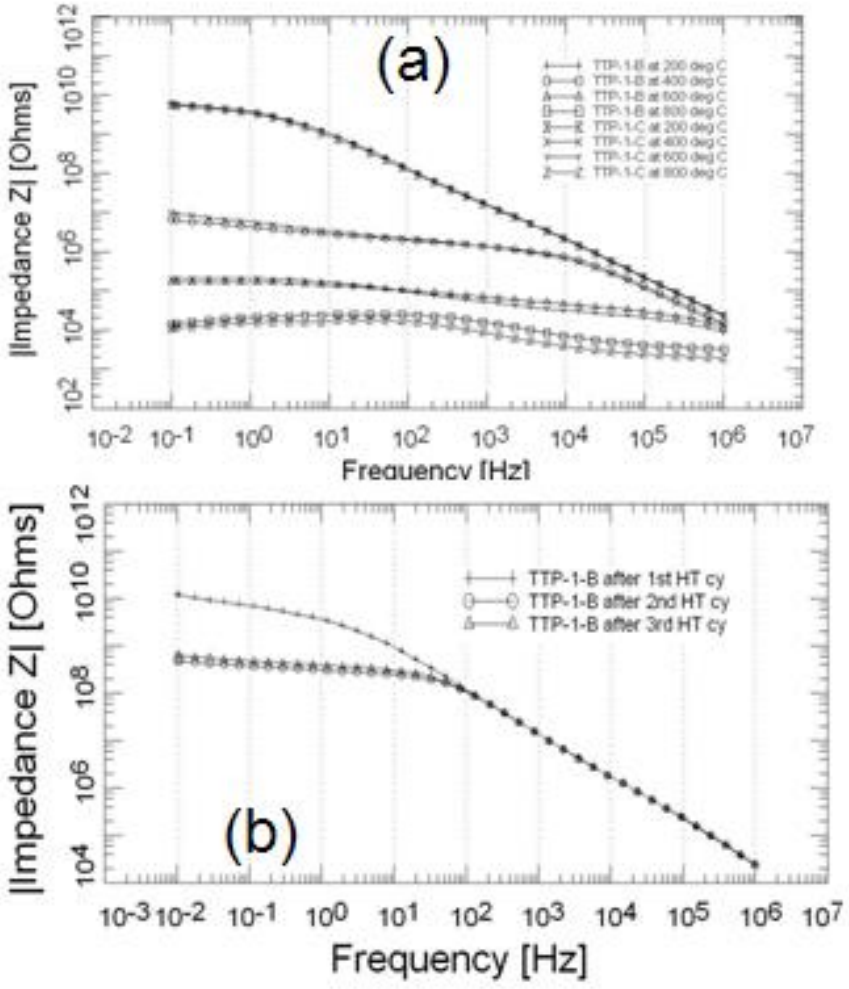

Figure 4.5: Change in specimen conductivity with increasing temperature and temperature cycling

4.6 Effect of electrolyte thickness on BbDS response of SOFC material:

As shown in Figure 4.6, the impedance and capacitance response for two different electrolyte thicknesses can also be measured via the BbDS technique. The larger electrolyte thickness yielded higher capacitance. This result is somewhat expected and confirmed by the BbDS measurement results. The importance of the result is that if there is an interface failure in the material structure, it will be captured via a change in capacitance.

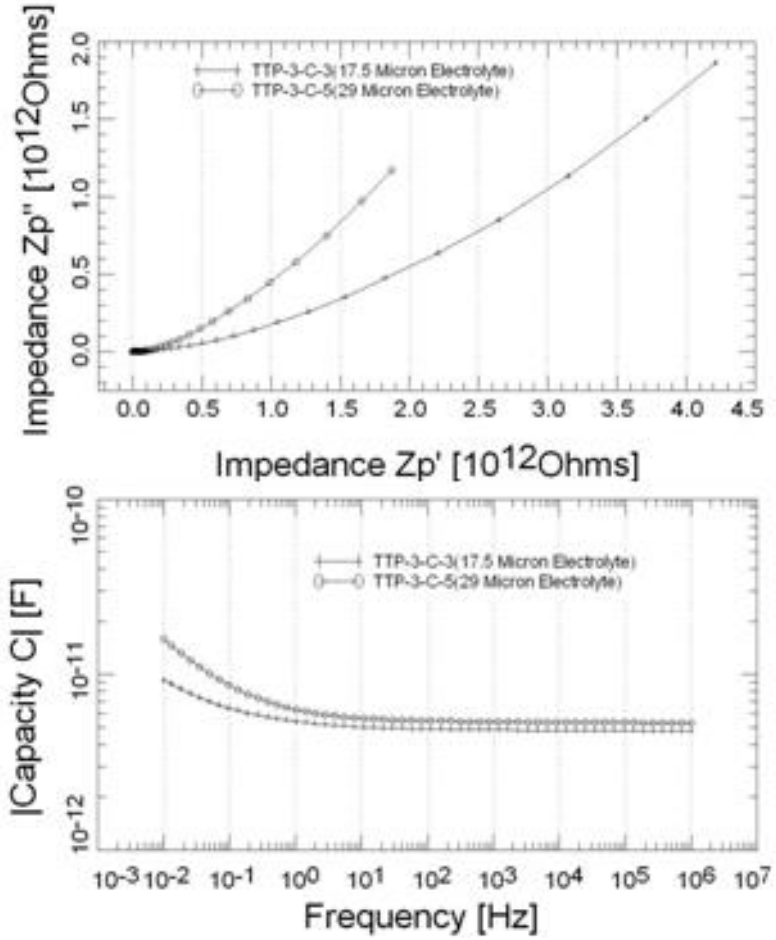

Figure 4.6: Room temperature BbDS response of SOFC button cell with different electrolyte thickness

4.7 Dielectric response of a damaged button cell

In order to study the effect of defects on the dielectric performance of an SOFC cell, a small crack was created on the dense electrolyte surface. BbDS was conducted on the sample before and after the damage at room temperature. Figure 4.7 is the electrical modulus representation of the sample's dielectric properties before and after damage.

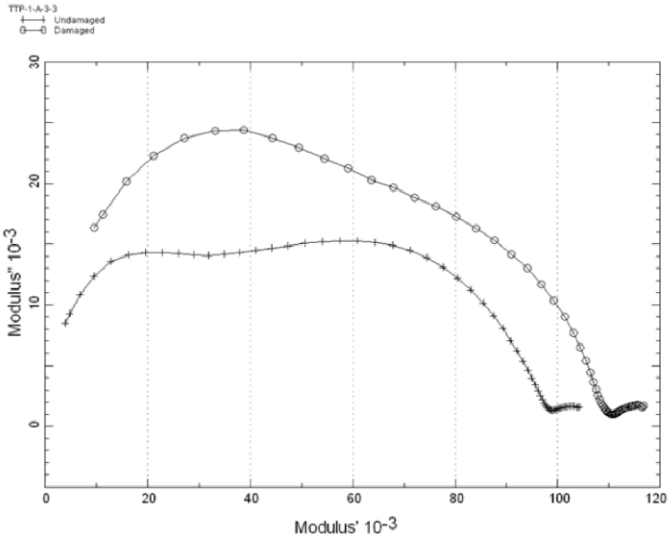

Figure 4.7: Electric modulus variation (real vs. imaginary part) for an undamaged (bottom) and damaged (top) SOFC.

In this case the well-known electric modulus representation was able to distinguish localized dielectric relaxation associated with a flaw [98]. As seen in Fig. 4.7 the relaxation peak shifted due to the damage induced inside the material.

4.8 Dielectric response of a Thermal Shock

Broadband Dielectric Spectroscopy of a sample at room temperature was performed on samples subjected to thermal shock using a special thermal shock tester constructed in-house which has the capability to heat up a sample to 800^{o} C in 1 min 20 sec and cool down to room temperature in 8 to 9 min. Figure 4.8 is the picture of the set-

up used for the thermal shock. BbDS tests were conducted before and after the thermal shock furnace treatment with two different dimensioned electrodes, which allowed observation of the effect of electrode size on the dielectric data.

The Nyquist plot and other dielectric representations are also shown below. Figure 4.9 and Figure 4.10, shows an increase in conductivity after the thermal shock.

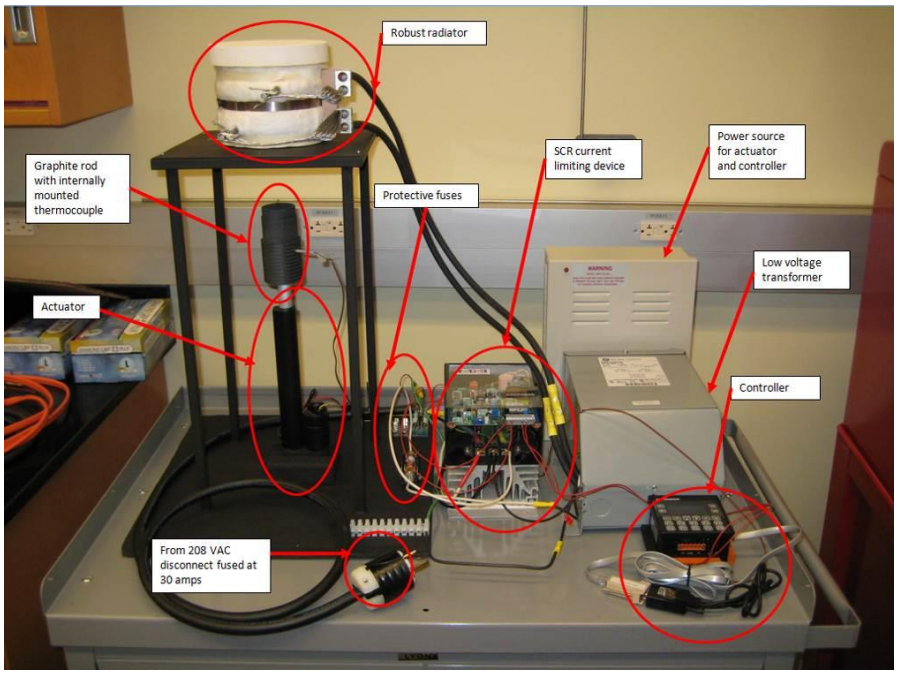

Figure 4.8: Visual set up of Thermal Shock Furnace (Build by Jon-Michael Adkins, Laboratory Technologist, Solid Oxide Fuel Cell Program)

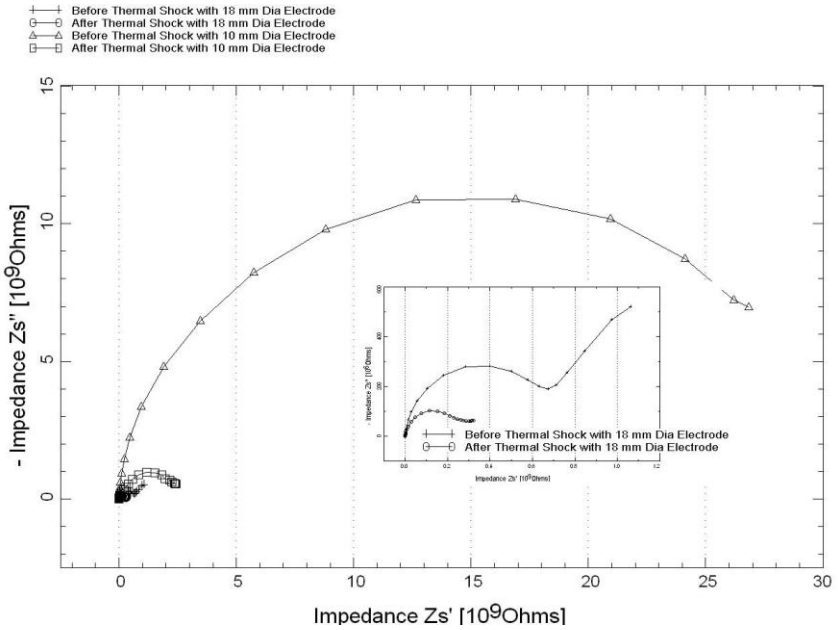

Figure 4.9: Nyquist plot before and after one Thermal Shock

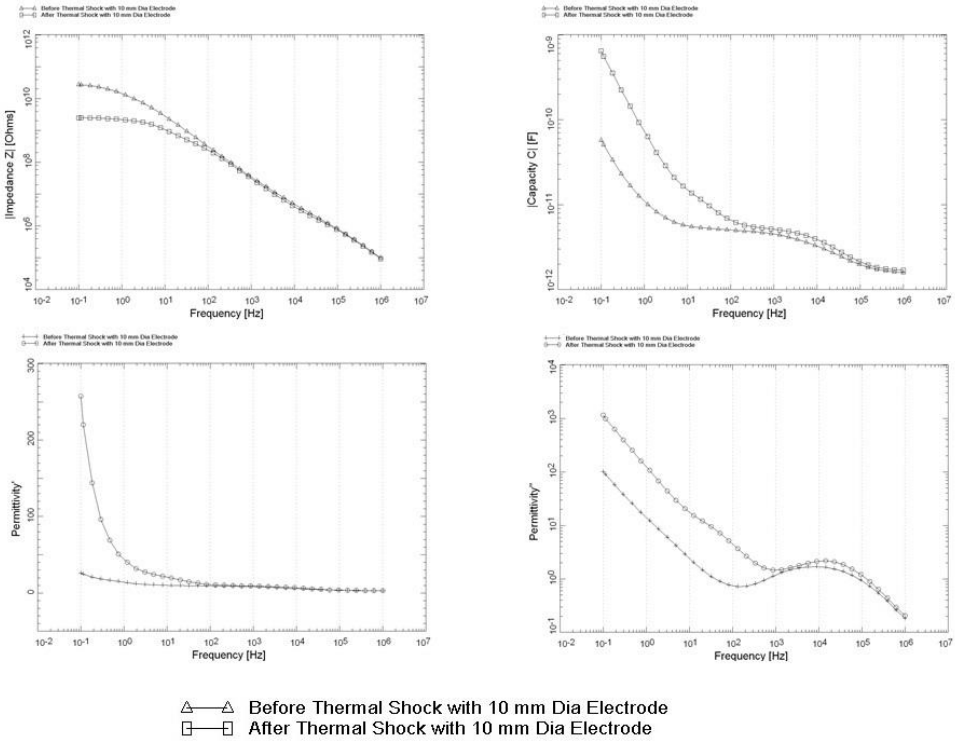

Figure 4.10: Dielectric representations of before and after thermal shock

The electrical modulus representation shows two peaks which shifted after the shock, Figure 4.11. This change may arise due to the change in the material grain boundaries or other distributed damage due to the thermal shock.

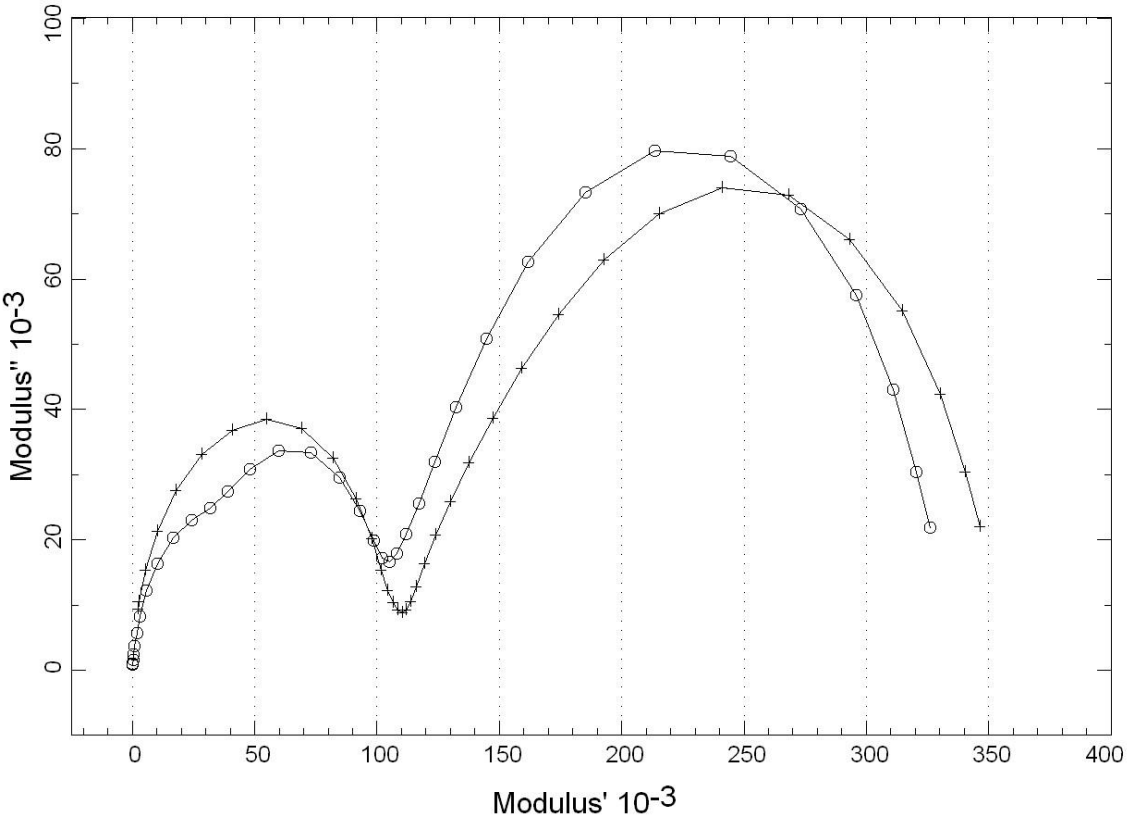

Figure 4.11: Electric modulus representation of thermal shock.

CHAPTER 5 IN-SITU DIELECTRIC STUDY OF COMPOSITE MATERIALS

Dielectric properties of woven glass fiber reinforced composites were observed for quasi-static uniaxial loading different orientation angles of the main fiber direction to the loading axis. Cyclic loading was also studied to look at the changes of dielectric properties. Samples were soaked in 5% KI (Potassium Iodide) solution and the effects of the ionic solution on the dielectric properties was investigated during the changes in mechanical response.

The composite material NP130 was chosen for these experiments, and was secured from Norplex-Micarta, a manufacturer of high performance thermoset composite laminates. The thin laminated composites used for tensile testing were made with a plain weave, E-glass fabric combined with a halogenated epoxy resin matrix. The manufacturers estimated 55% volume fraction of fiber in that material. The samples were composed of five plies, wherein each ply consisted of a single layer of fabric with two principle fiber directions of 0 degree and 90 degree, with the warp direction defined as the 0 degree orientation. The total thickness of the samples was nominally 1 mm. Table 2.1 is the summary of the typical properties of NP130 as published by the manufacturer. The samples were cut off-axis, at different angels relative to the principal axis. Sample layout and dimension is shown in Figure 5.1. In-situ mechanical and dielectric testing was also performed on carbon fiber reinforced composites to verify that the results observed in glass fiber reinforced composites were of a general nature.

Table 5.1 NP130 material properties

General Physical Properties	Unit	Values
Specific Gravity	-	1.8
Rockwell Hardness (.0625")	M Scale	100
Moisture Absorption (.0625")	%	0.1
Flexural Strength (.0625")	MPa	551.6
LW[1]/CW		413.7
Flexural Modulus (.0625")	GPa	18.6
LW/CW		16.5
Tensile Strength (.125")	MPa	344.7
LW/CW		275.8
Izod Impact Strength (.5") (Condition E-48/50)	J/cm	8.01
LW /CW		6.41
Compressive Strength (.500") Flatwise	MPa	482.6
Bonding Strength (.500")	Kg	997.9
Shear Strength (Perpendicular) (.0625")	MPa	151.7

Thermal & Electrical Properties	Unit	Values
Temperature Index (electrical/mechanical)	°C	130 / 140
Coefficient of Thermal Expansion X-axis (.062") Y-axis	"/"/°C $x10^{-6}$	10.0 / 12.0
Flammability Rating U. L. 94	Class	V-0
Breakdown Voltage Condition A	kV	65
(.0625") D-48/50		54
Electric Strength Condition A	kV/cm	263.8
(.062") D-48/50		255.9
Permittivity (.062") Condition D-24/23	-	4.80
Dissipation Factor (.062") Condition D-24/23	-	0.025
Arc Resistance (.125") D-495	Sec	120
Comparative Tracking Index (.125") D3638	-	150
Tg (.500")	°C	127

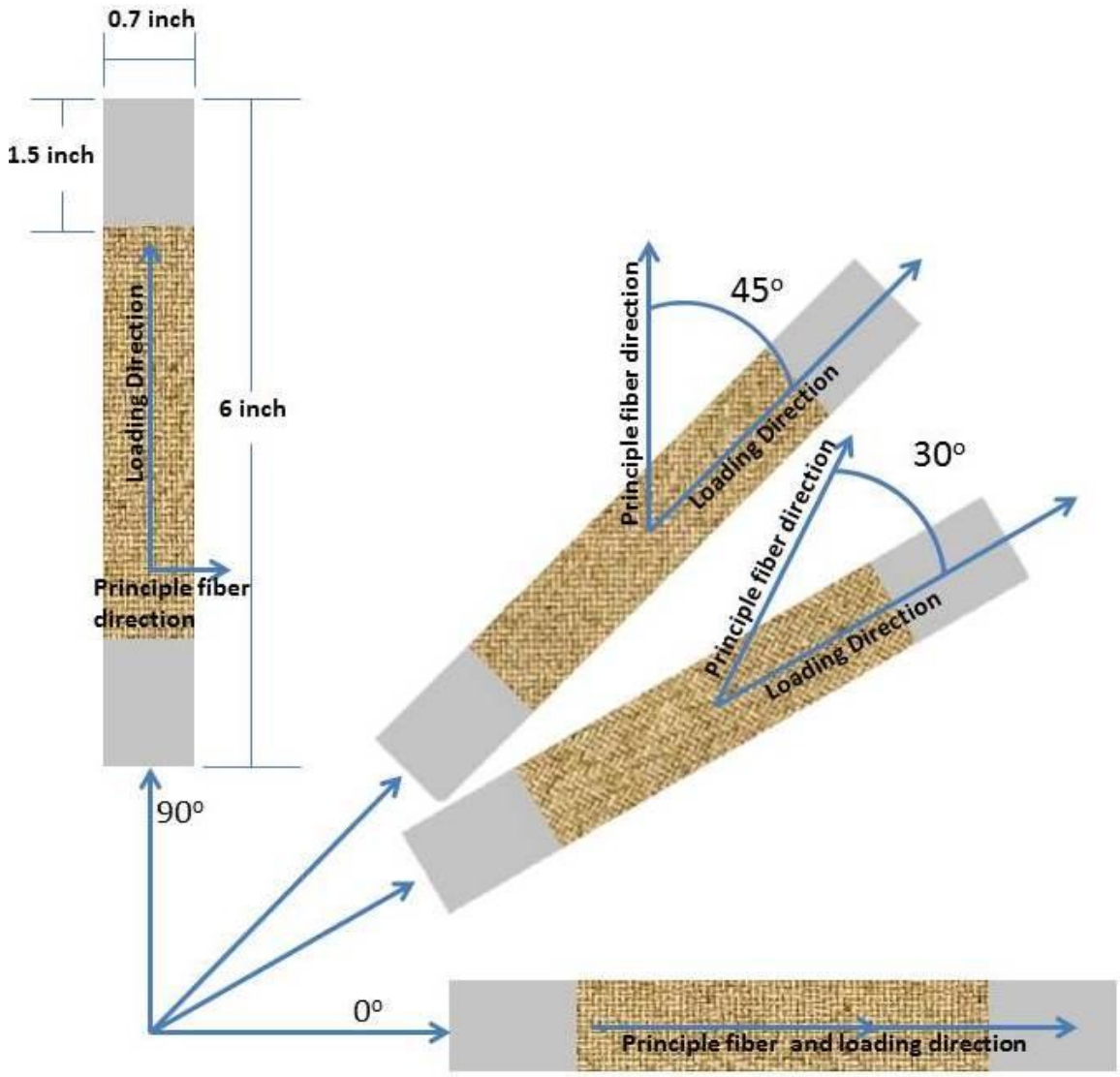

Figure 5.1 Sample layout and dimension

5.1 In-situ Tensile Test Set-up

To perform the tensile extension of coupon specimens of the woven glass fiber reinforced epoxy composites, strain was measured with an extensometer and a Novocontrol^{TM} unit was used to record dielectric data. Figure 5.2 shows the experimental setup used to measure the dielectric properties. Two types of dielectric data were collected, the first was with at a fixed frequency of 10 Hz during the test and the second was with a frequency sweep from 1 Hz to 10^6 Hz. The latter was performed at different

strain levels to interpret data from the AC signal applied by specially designed plates fixed on opposing sides of the thickness of the specimens.

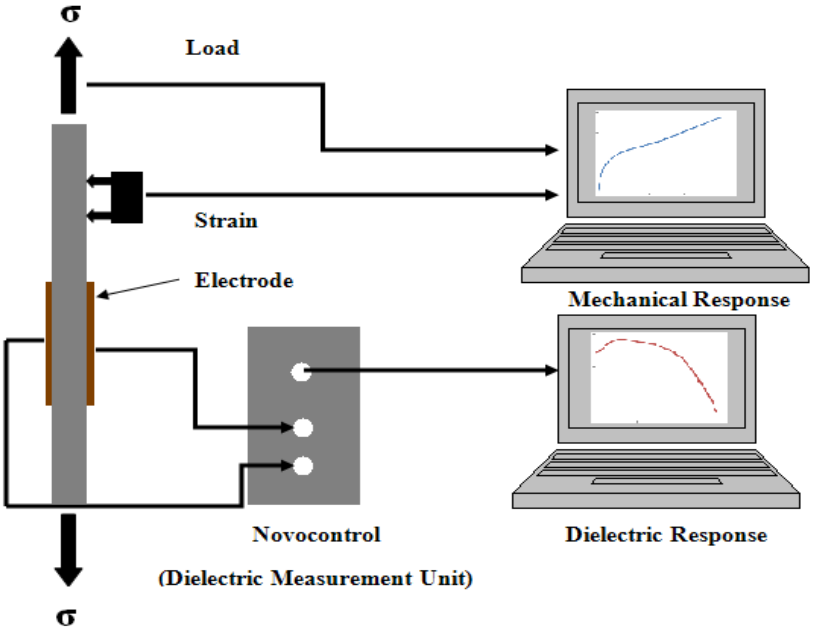

Figure 5.2 Schematic of the experimental setup

5.2 In-situ Tensile Testing Results

Tensile tests of different fiber orientations with respect to the loading direction were performed. Dielectric property changes were measured during the damage accumulation phase until the samples underwent material failure. Figure 5.3 shows the trend of the real part of the permittivity / electrical compliance at a single frequency (10 Hz) which was recorded in-situ during the loading period. For all orientations at the end of the loading period, when fiber fractures lead to the final failure, a sharp decrease in the real part of the permittivity was observed.

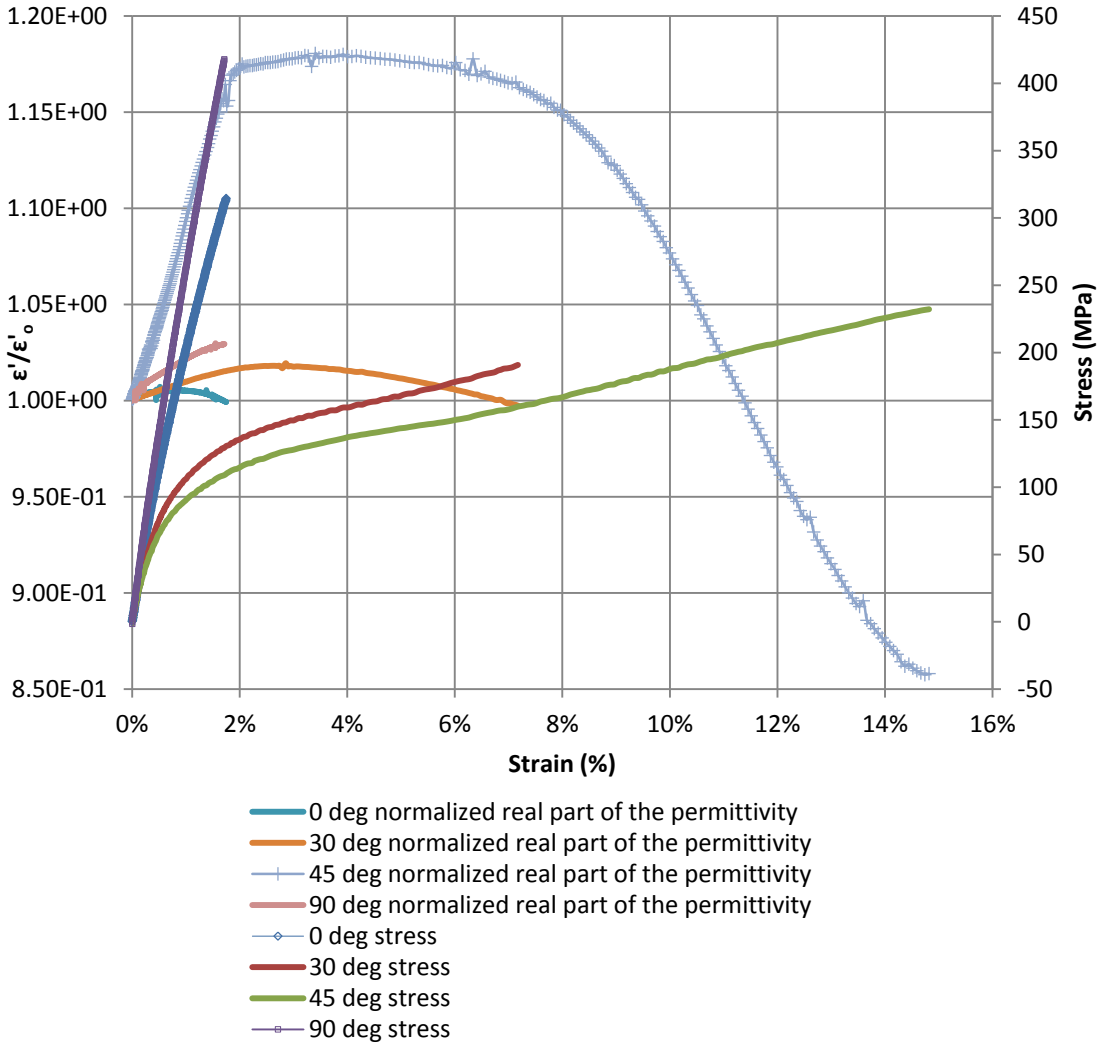

Figure 5.3 Normalized real part of the permittivity and Stress Vs Strain

Changes in the imaginary part of the permittivity during the loading are shown in Figure 5.4. During the early stages loading had a significant effect on the imaginary part of the permittivity which showed an overall increasing trend in these tests . For off axis samples abrupt changes occurred in the loading region where distributed matrix damage occurred.

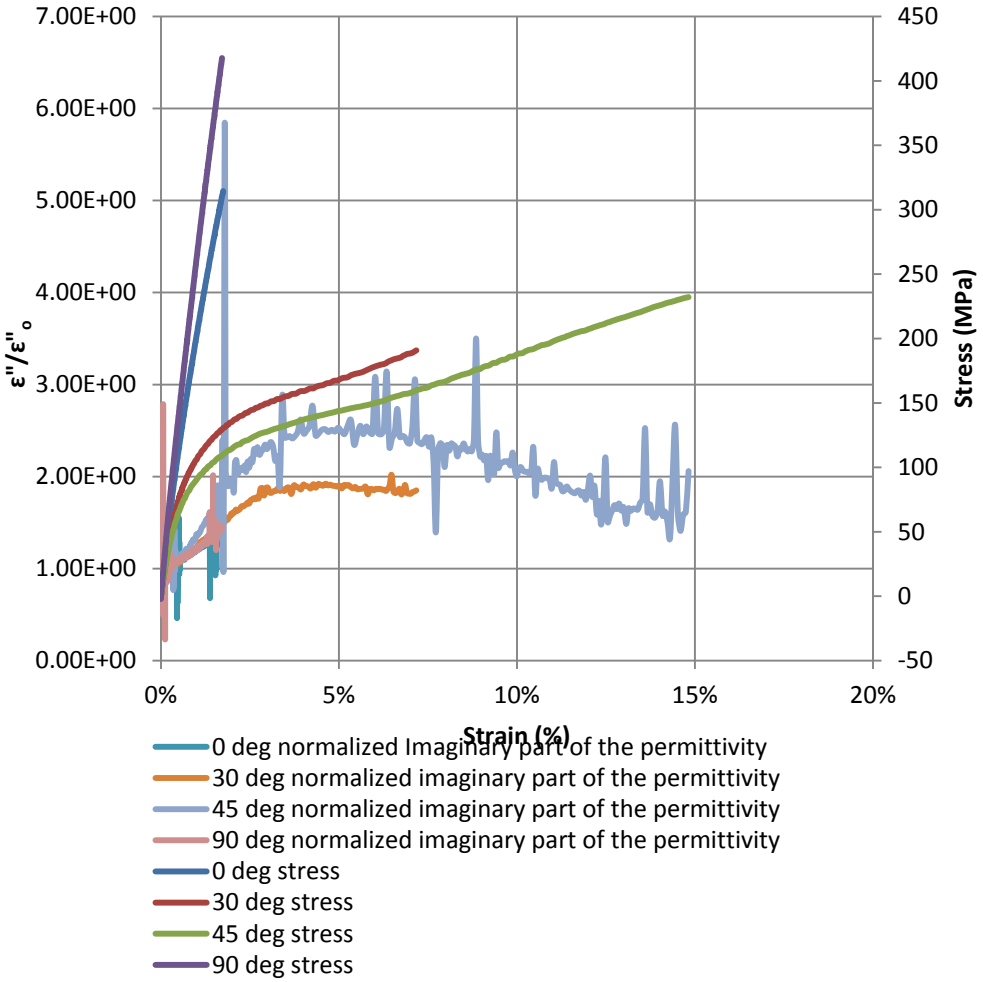

Figure 5.4 Normalized Imaginary part of the permittivity and Stress Vs. Strain

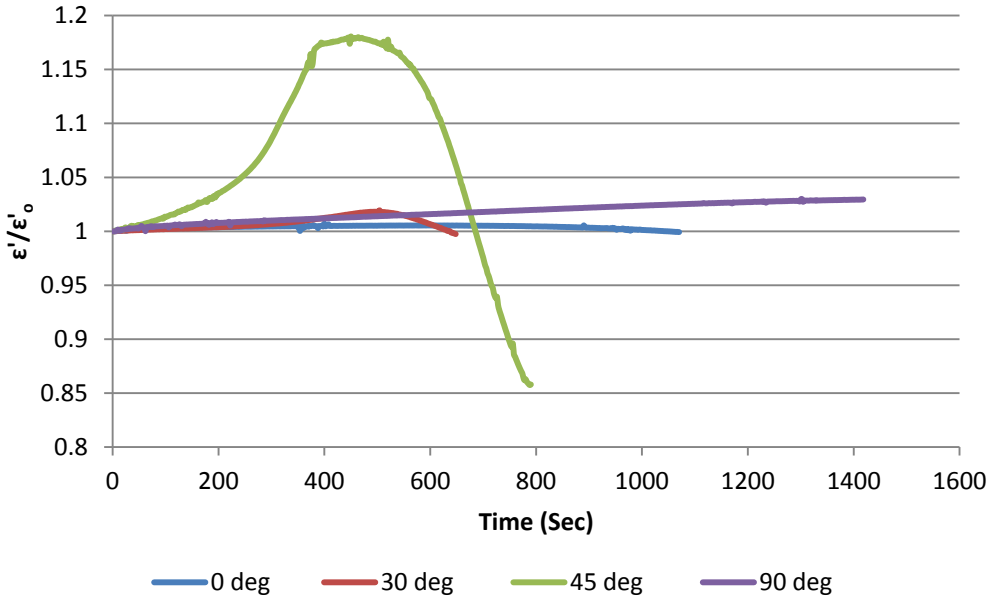

Figure 5.5 Normalized Real Part of the Permittivity Vs Time

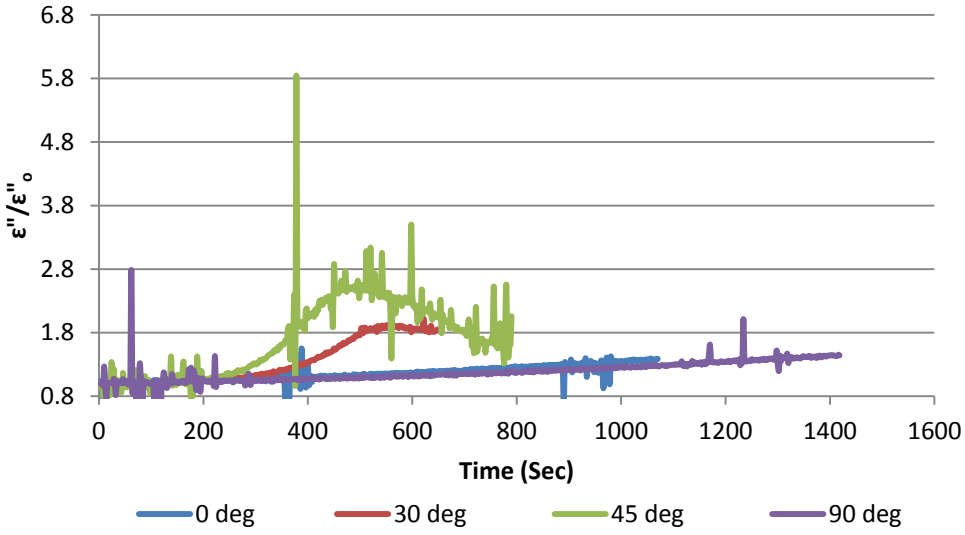

Figure 5.6 Normalized Real Part of the Permittivity Vs Time

In Figure 5.5 and Figure 5.6, the time history of the dielectric properties are also shown.

5.3 Edge Replication: Observation of Damage Progression

In order to recover damage information directly, especially crack initiation and growth, an edge replication method was utilized which is widely used in quantifying crack density [6, 7]. Edge replicas were acquired by pressing an acetone-softened acetate tape against the sample edge. After hardening, the tape reveals permanent details of the sample edge. Images were taken with a Leica™ optical Microscope. Figure 5.7 shows the initialization of damage and progressive accumulation of the damage until material failure.

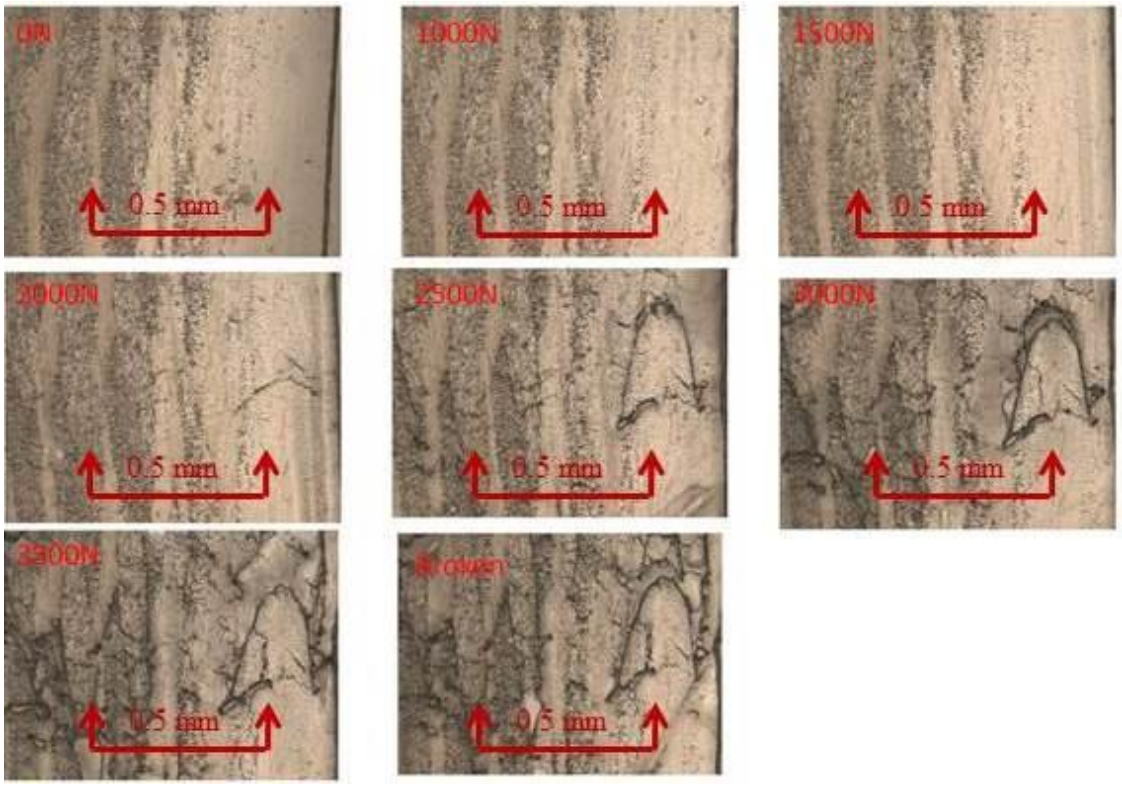

Figure 5.7 Edge replica at different Load

5.4 Rate Dependency of Dielectric Properties:

Xing *et. al.* [8] has demonstrated strain rate effects on the mechanical response of composite materials under similar conditions to those used for the present work. Figure 5.8 illustrates that the dielectric properties are rate dependent in our situation. With higher strain rates, initial damage occurs rapidly and is indicated by the higher permittivity change at higher strain rates.

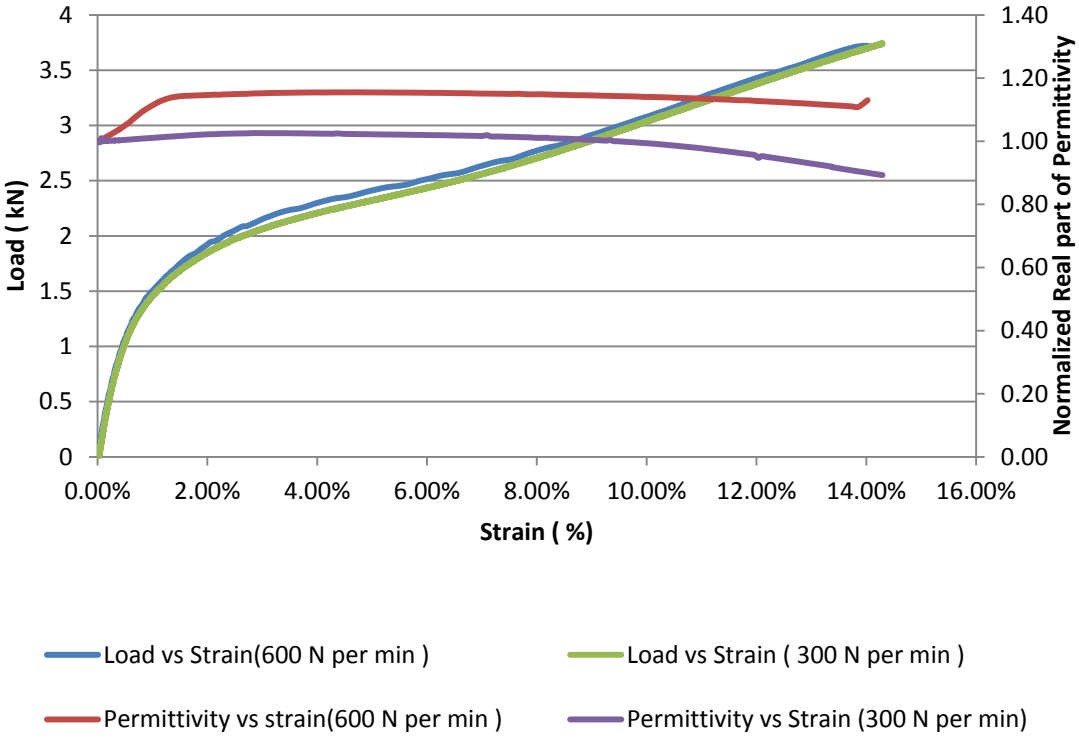

Figure 5.8 Rate dependency of the dielectric property

5.5 Effect of Cyclic Loading on Dielectric Properties:

Several cyclic loading tests were also performed at a frequency of 10Hz when the maximum load and minimum load was 2.5kN and 0.25kN respectively. Figure 5.9, shows that with increasing cycle time, the initial damage had a large impact on the dielectric properties after which the capacitance decreased.

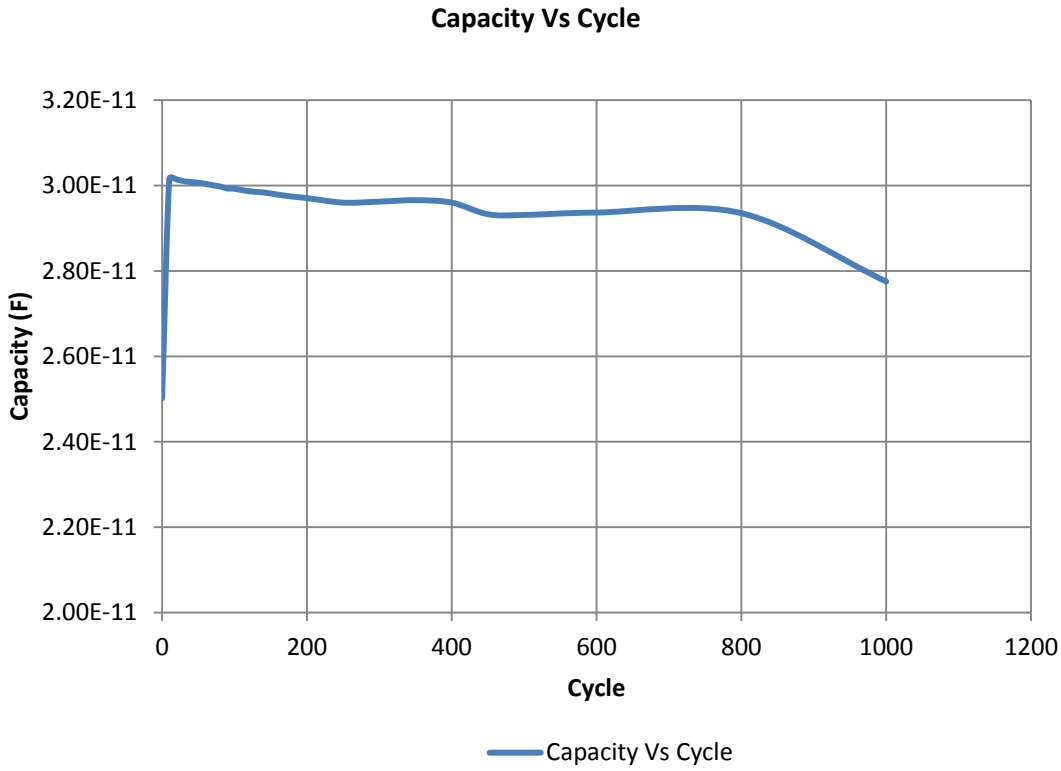

Figure 5.9 Change in capacitance with increasing cycle.

5.6 Effect of Electrode Shape on Dielectric Properties:

Different shapes and sizes of electrodes were used to perform the in-situ dielectric measurements. 10 mm diameter round electrodes yielded the same dielectric property variations during the loading period (300 N/min) as the 50 mm X 10 mm rectangular electrodes. Figure 5.10 represents those results.

The rectangular electrode arrangement had a larger surface area so it was able to capture more material level information than the round electrode arrangement.

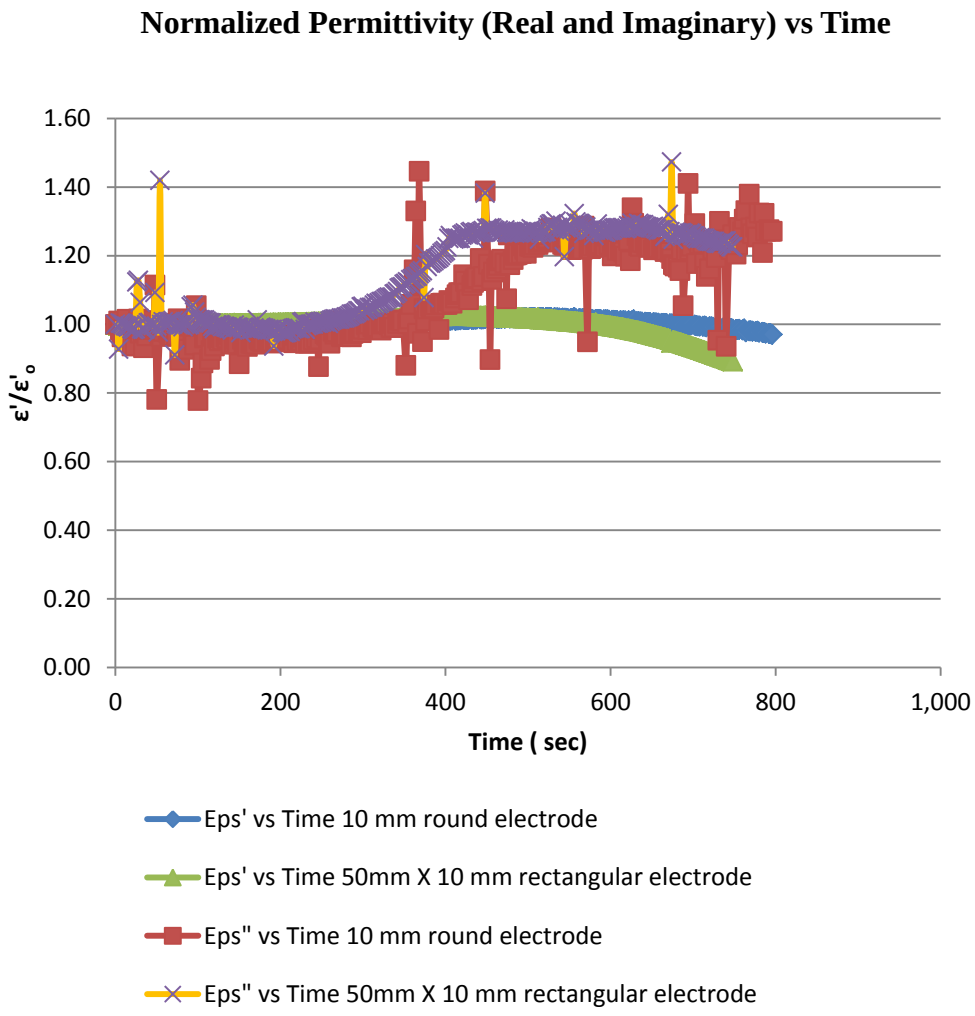

Figure 5.10 Comparison of the dielectric properties for different electrode arrangement.

5.6 Broadband Dielectric Spectroscopy at Different Load and Strain Levels:

At different loads, single- frequency dielectric measurements were taken for 1 min. during which the load was held constant. From Figure 5.11 and Figure 5.12 it is clear that in the non-linear part of the quasi-static stress-strain curve the permittivity increases somewhat at fixed load. In the nonlinear region, the strain increases while the load is constant, causing material state change.

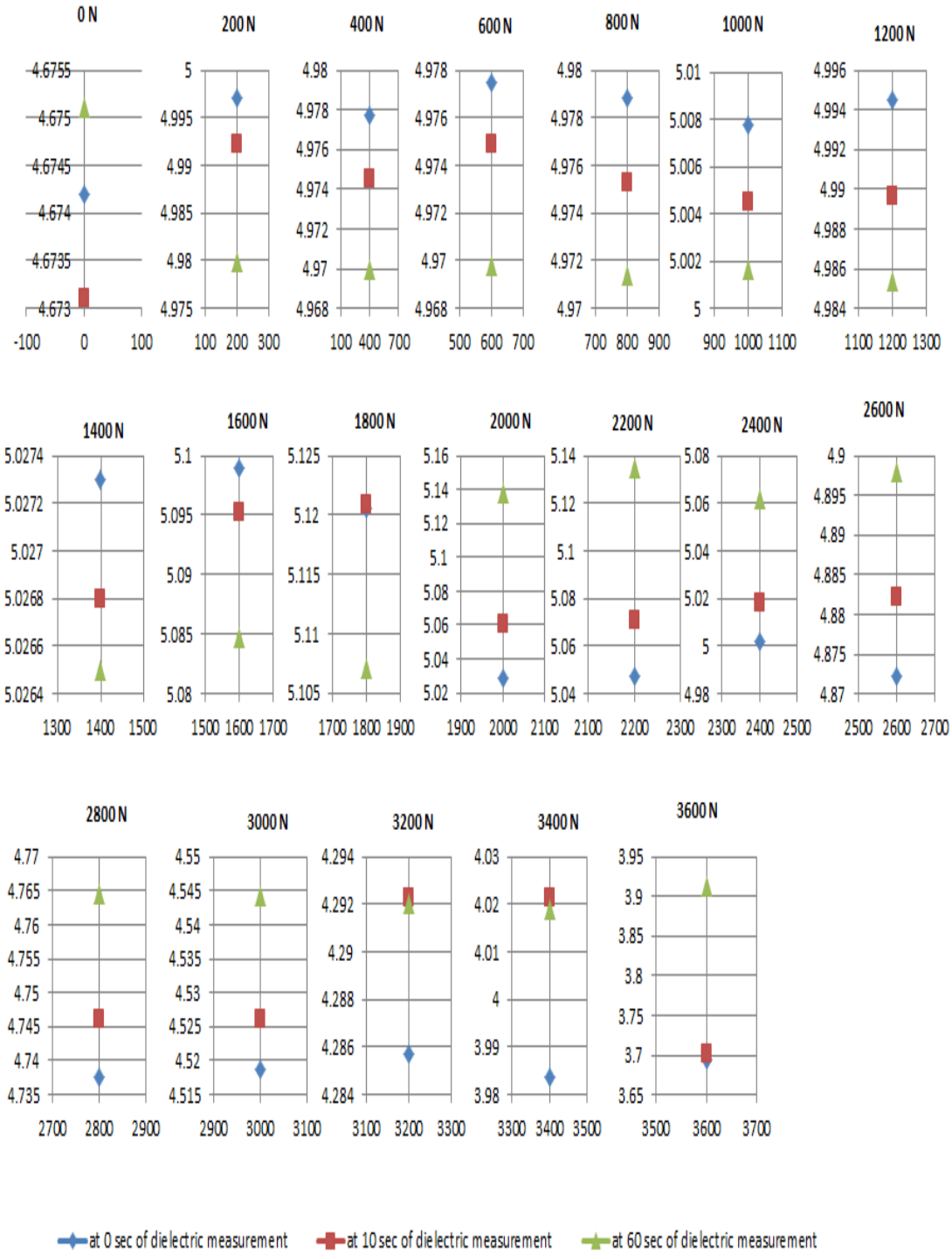

Figure 5.11 Change in Permittivity while load is fixed

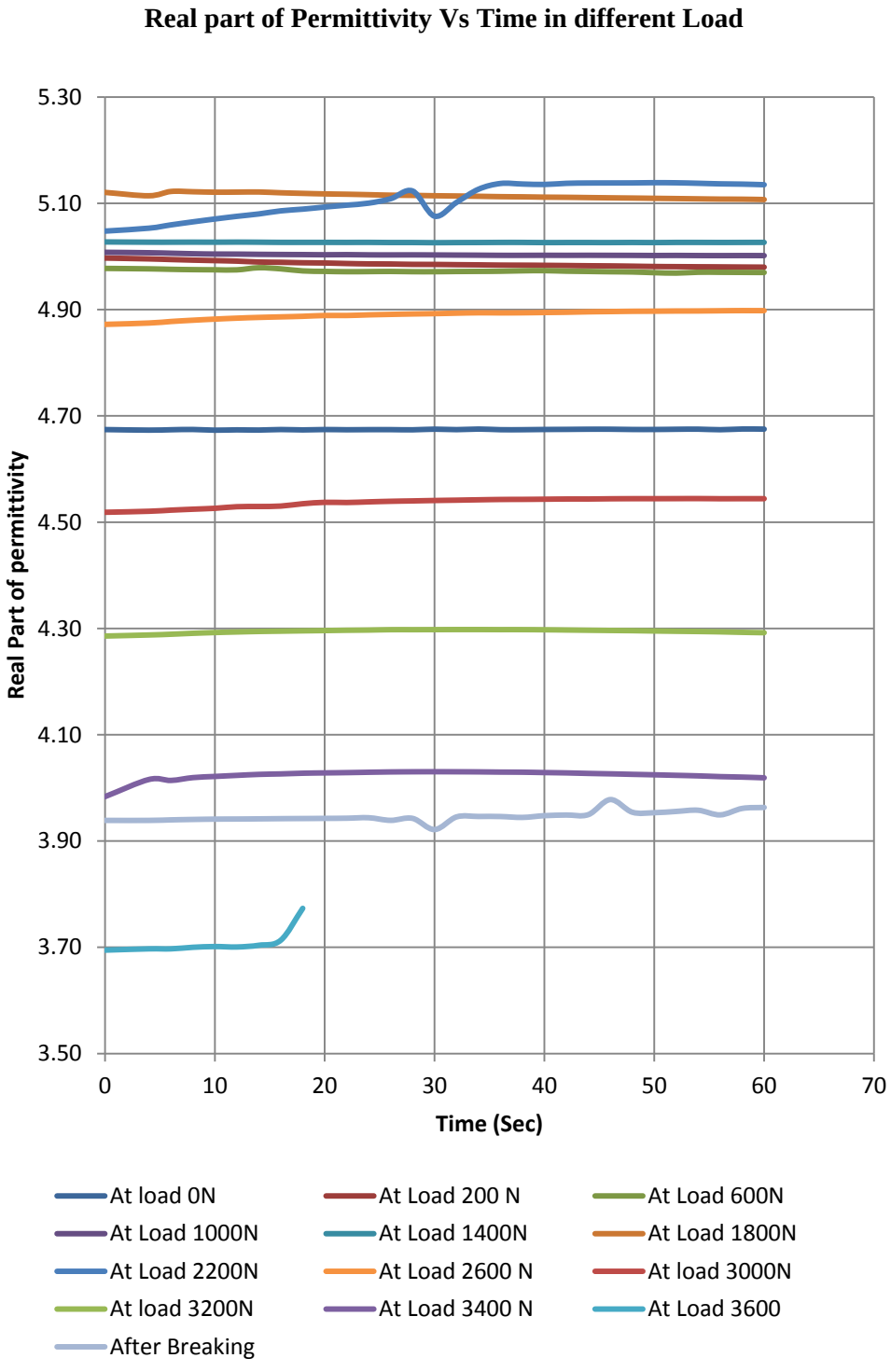

Figure 5.12 Real part of Permittivity Vs Time in different Load

5.7 Effect of Ionic Solution on the Dielectric Properties:

In-situ dielectric properties of a sample that was soaked in 5% KI (Potassium Iodide) solution for three months showed a somewhat different trend compared to the samples stored in room ambient conditions. The conductive solution diffused inside the material through the fiber-matrix interface and made the interfaces more conductive; this is thought to be the reason for the conductive nature of the damaged stage. Figures 5.13-5.15 show the difference in the nature of this in-situ test.

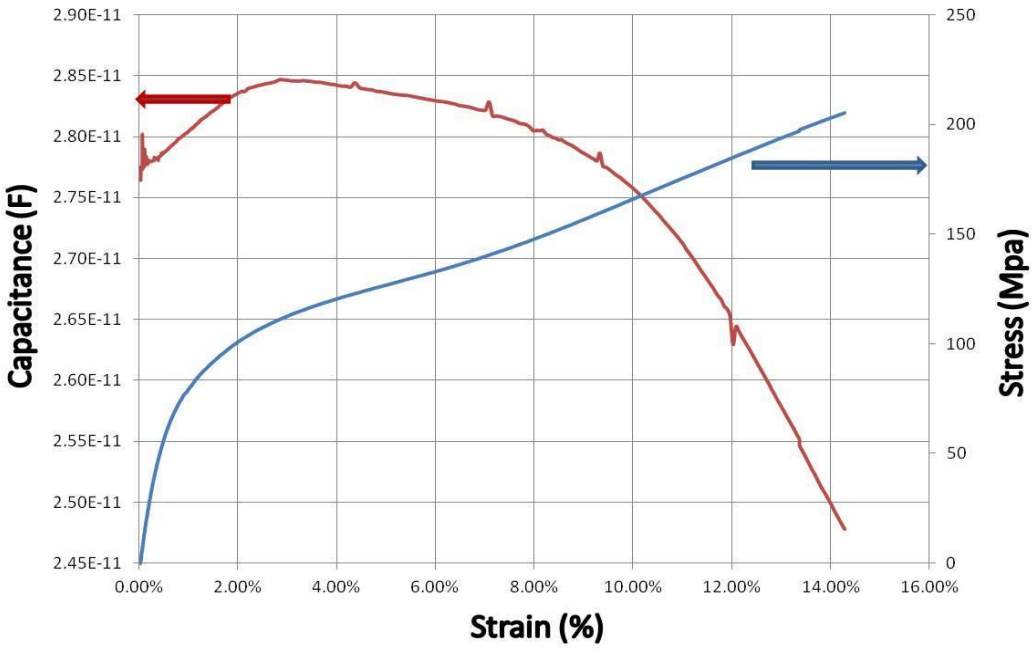

Figure 5.13 In-situ capacitance change of a sample that stored in room condition

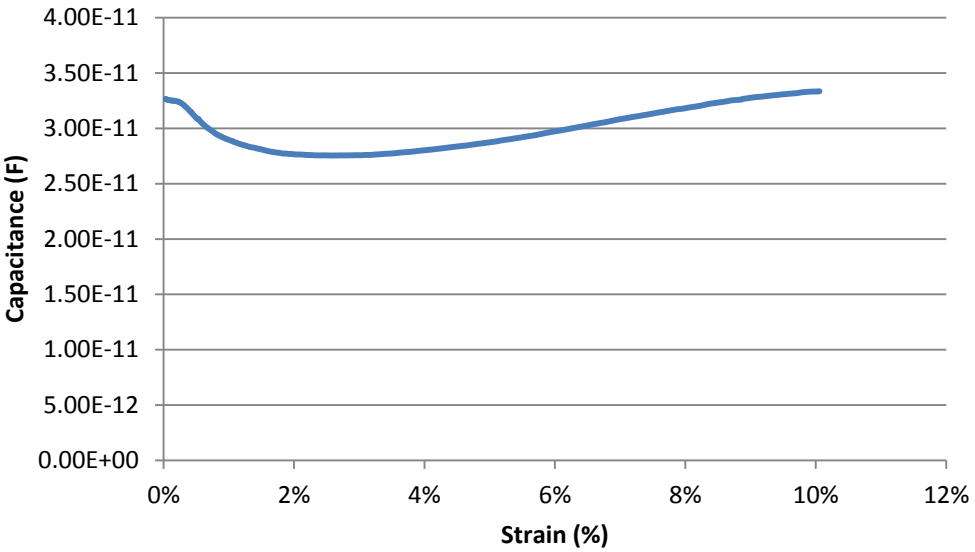

Figure 5.14 In-situ capacitance change of a sample that stored in KI solution

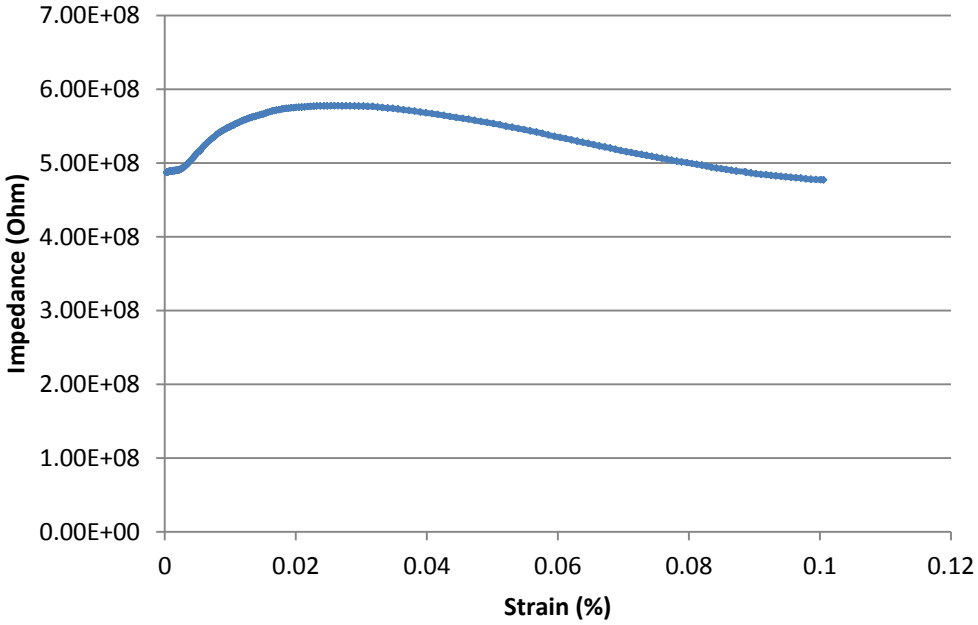

Figure 5.15 In-situ impedance change of a sample that stored in KI solution

5.8 Carbon Fiber Reinforced Composite:

Woven carbon fiber reinforced epoxy composites from Norplex-Micarta were tested to investigate their changes of dielectric properties during a tensile test. These composites had 5 plies. Two types of testing were performed. In one arrangement the electrodes were covered with electrical tape in order to provide an insulating material between the conducting composite and electrodes, and as a control, one test was performed without tape on the electrodes.

Figures 5.16 and 5.17 show the variations of permittivity during the quasi-static loading periods. These are also the same trends as seen for the glass fiber reinforced composites.

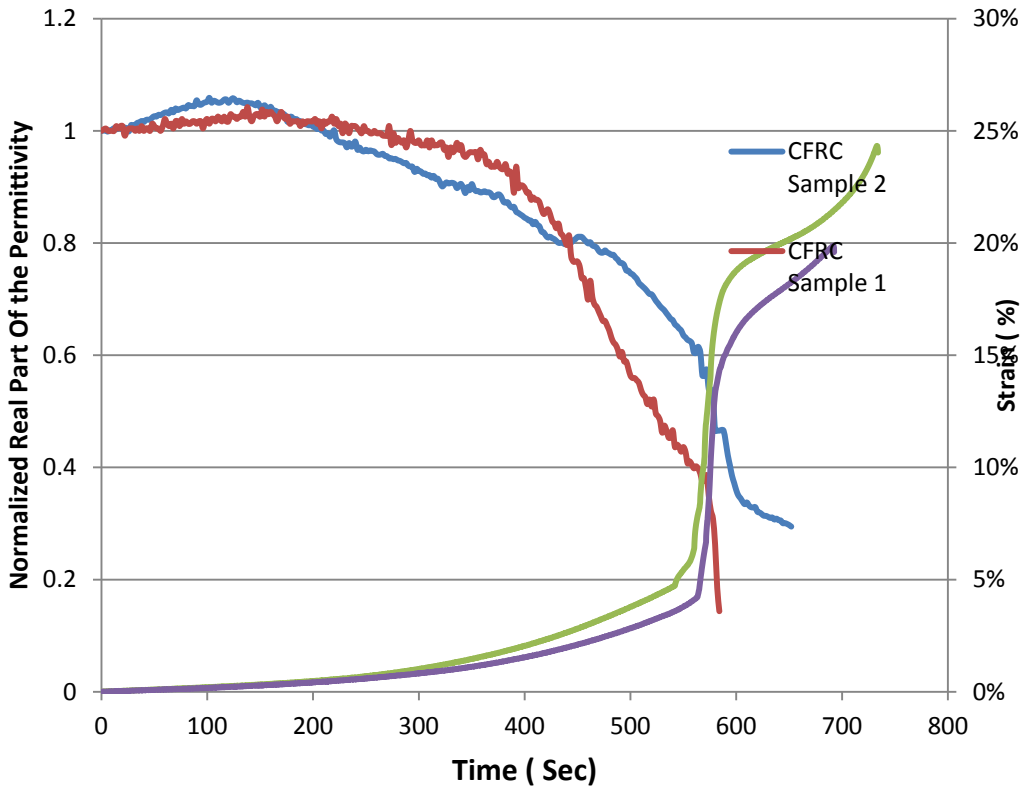

Figure 5.16 Normalized Real Part of the Permittivity Vs Time without tape

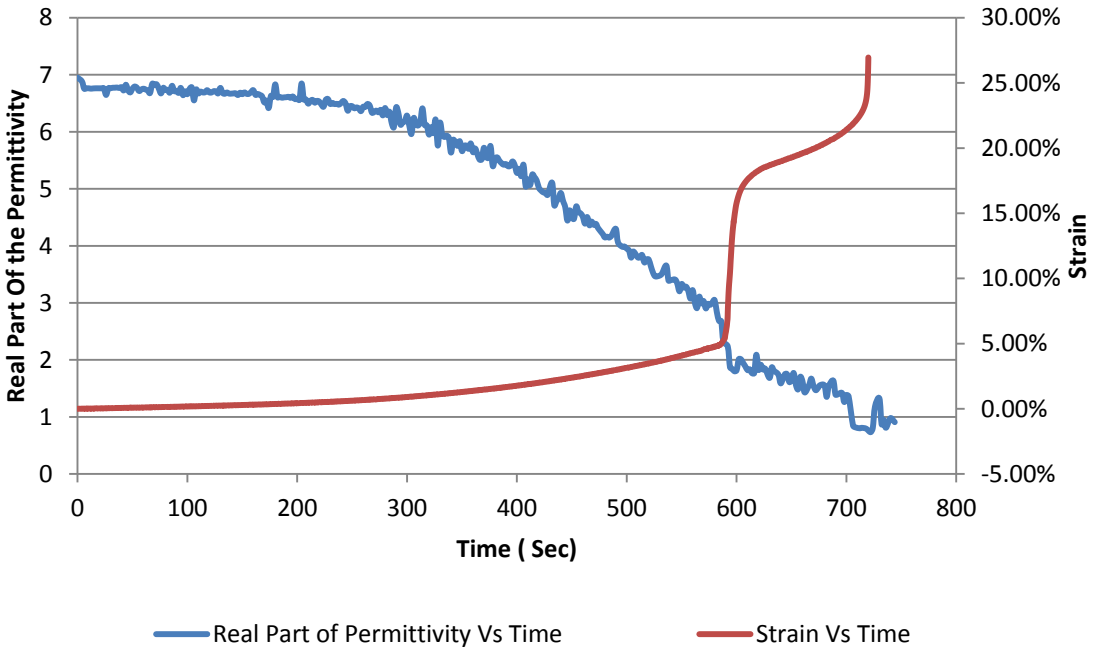

Figure 5.17 Real Part of the Permittivity Vs Time with tape

CHAPTER 6 EX-SITU DIELECTRIC STUDY AND PROGNOSIS BASED ON INITIAL DIELECTRIC PROPERTIES

In the previous chapter we studied the dielectric property changes of the material with mechanical loading, in-situ. At different frequencies, dielectric properties have different significance, and that is the reason Broadband Dielectric Spectroscopy (BbDS) is a strong tool to investigate the material state changes. The complex dielectric function $\varepsilon^*(\omega)$ depends on the angular frequency, $\omega = 2\pi f$ (here f is the frequency of the outer electric field), and temperature. Ex-situ dielectric measurements were done in the frequency range of 0.1 Hz to 1 MHz and in this frequency range interfacial polarization and dipole polarization mechanisms were prevailing.

For different polarization mechanisms there are relaxations which are characterized by a peak in the imaginary part of the permittivity, ε'' , and step like decreases of real part of the permittivity , ε', with increasing frequency. Because of the conduction phenomena or polarization effects (at inner boundaries) there is an increase of the imaginary part of the permittivity, ε'' , or dielectric loss with decreasing frequency. This phenomenon is used to investigate the material system in ex-situ dielectric studies.

6.1 Experimental Set up

To measure the dielectric properties sample cell setup was placed inside of a Faraday cage to avoid electromagnetic noise. Samples were place in between two copper

plates which were attached to a Teflon block, held by a spring loaded leveler that applied a uniform load, Figure 6.1.

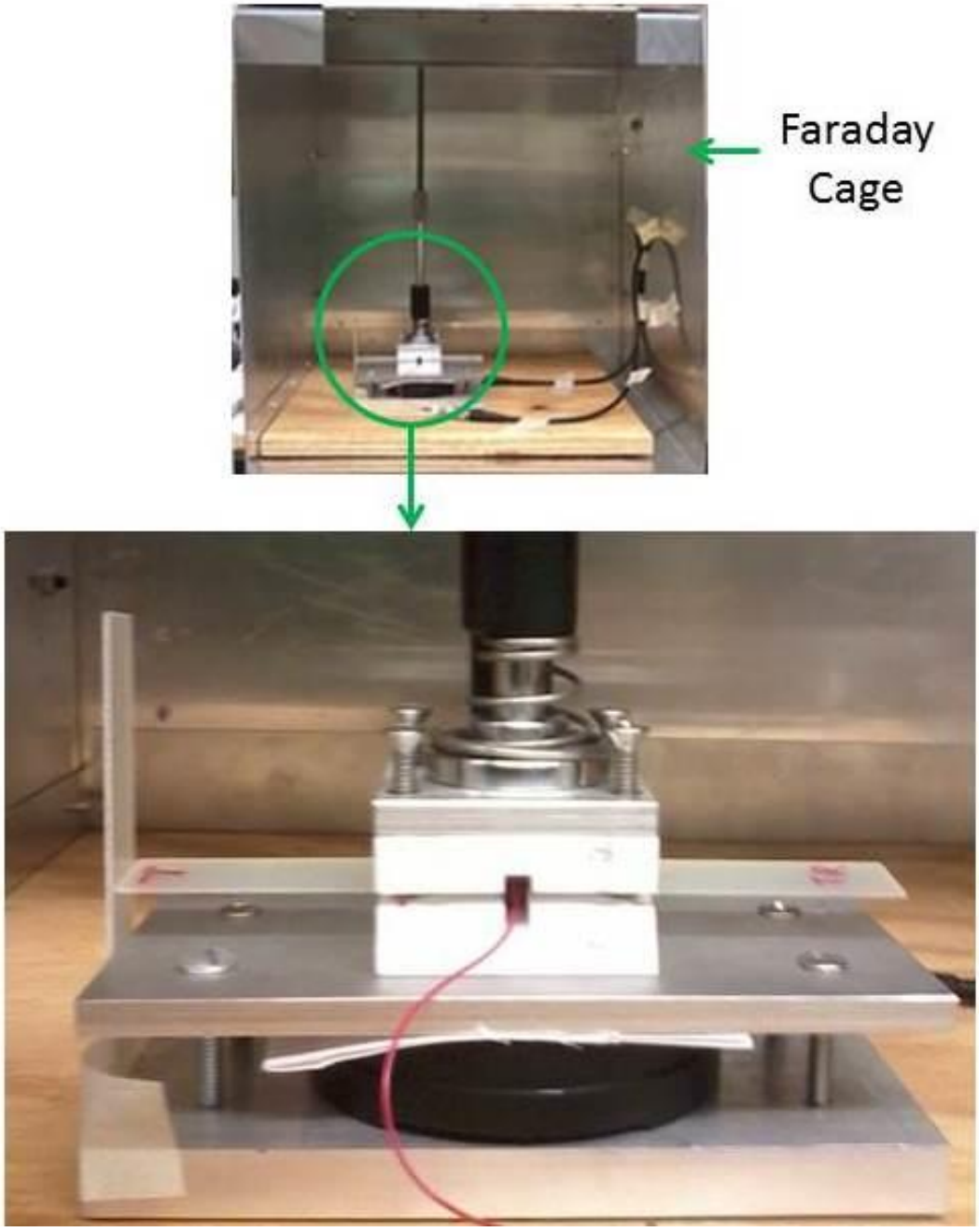

Figure 6.1 Ex-situ Experimental Setup

6.2. Variation of electrode diameter

For the present measurements, both round and rectangular copper electrodes were used. Electrodes were cut from copper plate and polished by very fine grit sandpapers before use. During polishing, the edge of the electrodes were rounded somewhat, so there is a variation of the resulting diameter from the initial measured diameter. The dimension of the rectangular set of electrodes were 12.7 mm (half inch) by 50.4 mm (two inch) and the effective diameter was 28.547mm; the round electrode set's diameter was 12.7 mm. Figure 6.2 shows the variation of the real part of the permittivity (normalized by the real part of the permittivity obtained by using the measured electrode diameter) with the diameter of the electrode.

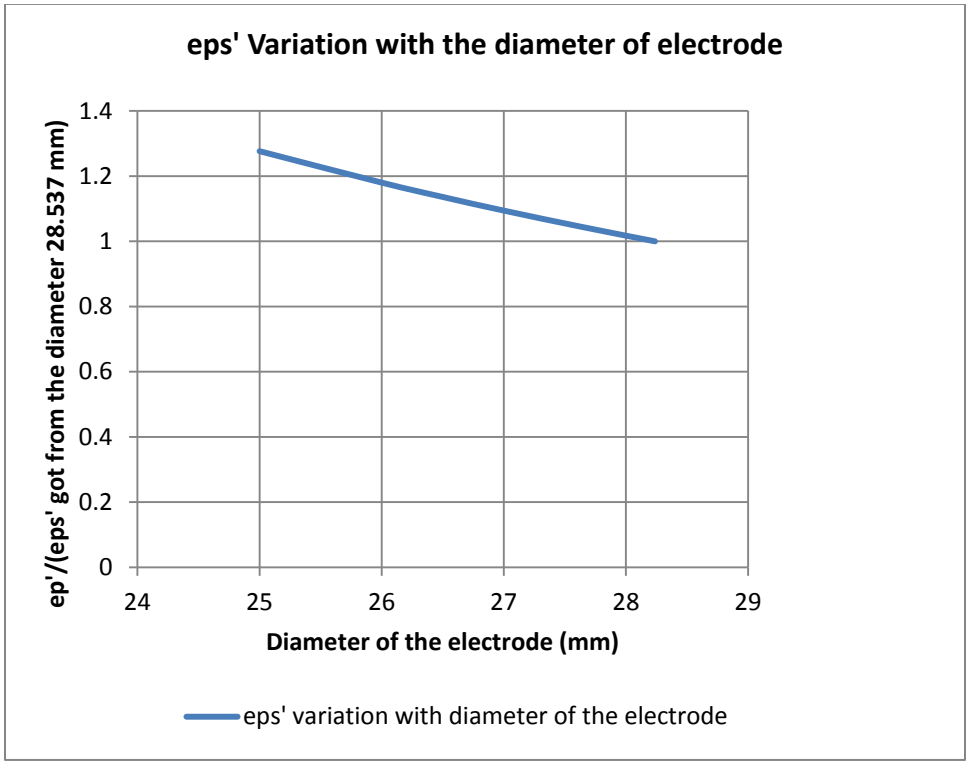

Figure 6.2 Real part of the permittivity variation with the diameter of electrode

6.3 Effect of electrode pressure on the dielectric property measurement

Dielectric properties were measured with different electrode pressure. On the top of the spring load extra dead weight was placed to increase the load pressure on the electrode. There was a measurable increase in dielectric properties measured by the assembly with the increase of the pressure, Figure 6.3.

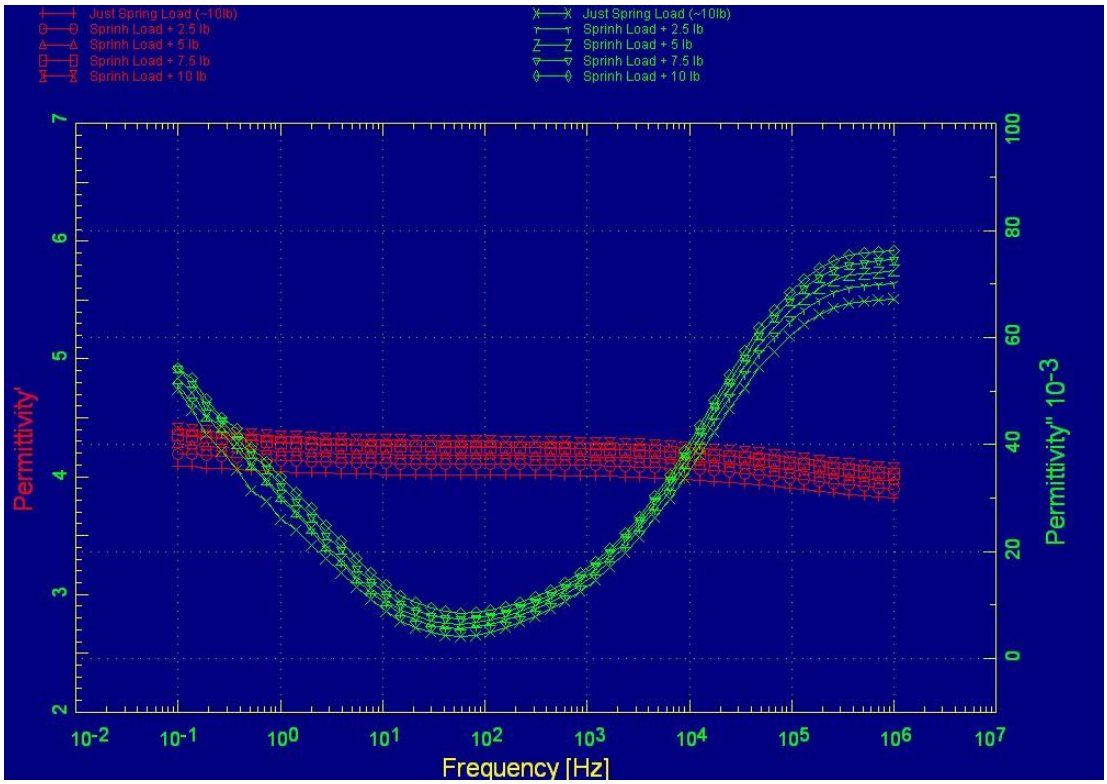

Figure 6.3 Variation of dielectric properties with electrode pressure

6.4 Repeatability of the measurement

To test the repeatability of the measurement, one specimen was tested several times. Each time after the dielectric measurement, the specimen was taken out and kept outside the faraday cage for ten minutes, and then it was placed in between the electrodes and the measurement was taken again. When the properties were plotted against the

frequency, there was a close agreement between all of the measurements which ensured the repeatability of the test system, as shown in Figure 6.4.

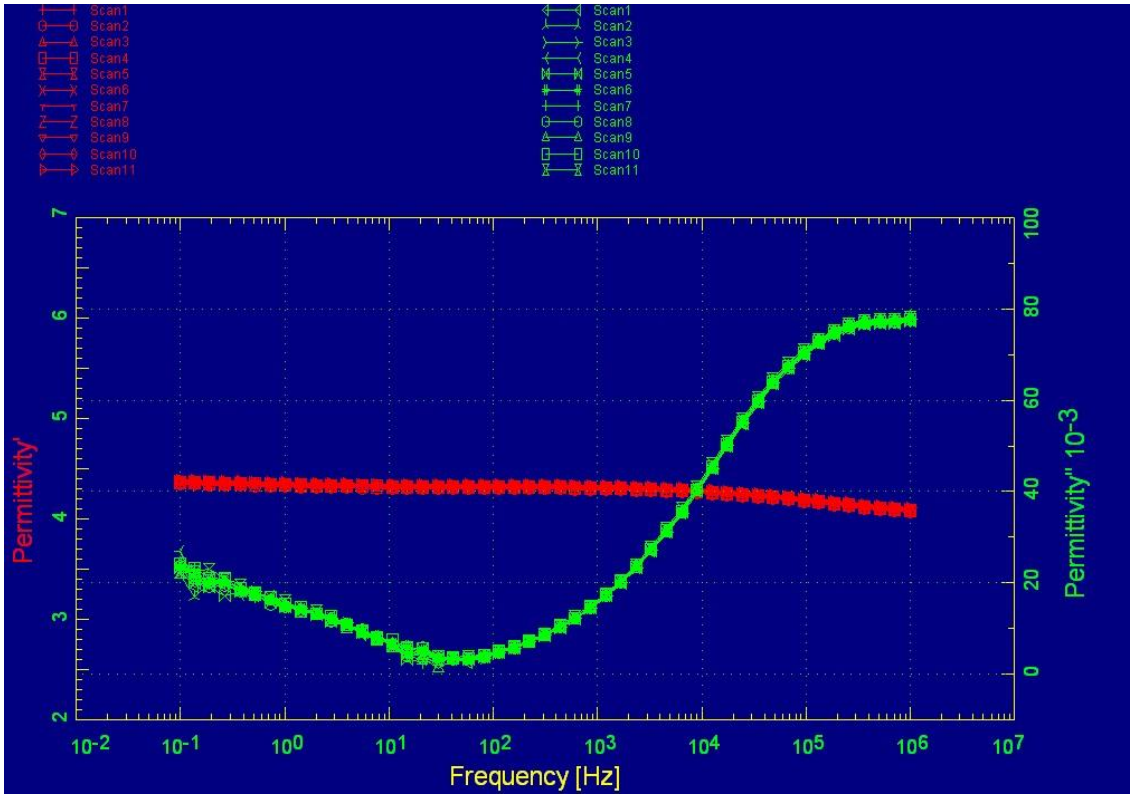

Figure 6.4 Repeatability test

6.5 Dielectric measurement after loading unloading

To observe the change in dielectric properties after certain applied loads, 21 samples (45 degree off axis glass fiber reinforced epoxy composites) were tested with the same dimensions (0.7 inch width, 0.04 inch thickness and 6 inch long, sample layout is shown in figure 5.1). One sample was tested to determine the breaking load/stress and breaking strain of that sample set with a loading rate of 600 N/min; the sample broke after 15.29% strain and 3.39 kN load. Figure 6.5 shows the load-strain curve of the sample.

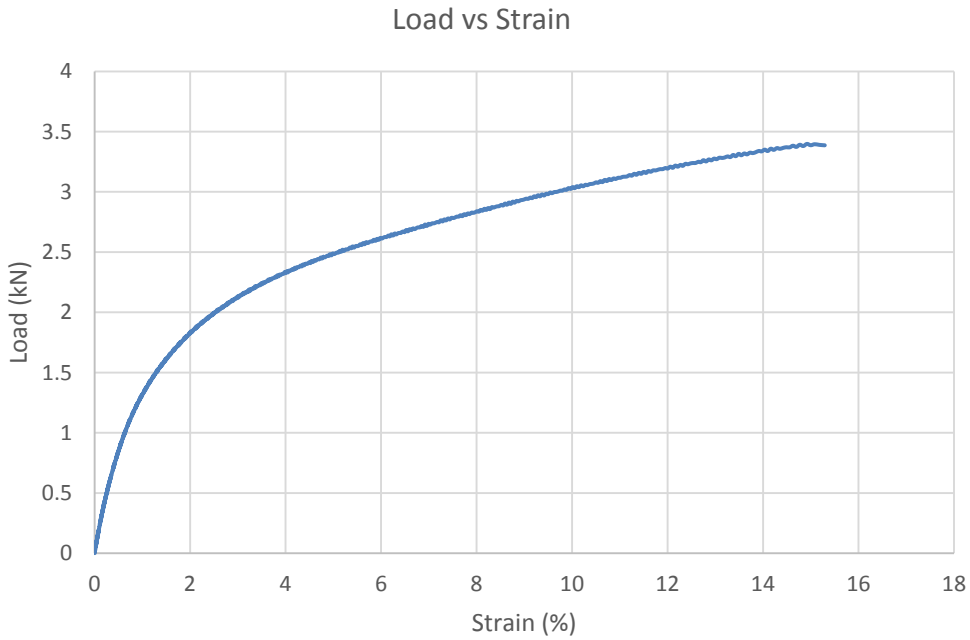

Figure 6.5 Load-strain curve

Among other 20 samples; 5 groups of samples with 4 in each group waere loaded to 1.5 kN (1.2% strain), 2 kN (2.5% strain), 2.5 kN (5.1% Strain), 3 kN (9.6% Strain) and 3.2 kN (12% strain) and then unloaded to 0 N.

Dielectric relaxation strength (DRS), $\Delta\varepsilon$, is the difference of the static permittivity and limiting high frequency dielectric permittivity, as given in equation 6-1.

$$\Delta\varepsilon = \varepsilon_s - \varepsilon_\infty \qquad 6-1$$

where, ε_s is the static permittivity and ε_∞ is the limiting high frequency dielectric constant. To calculate DRS here, the difference between the low frequency real part of the permittivity and high frequency real part of the permittivity were considered. In the frequency range from 0.1 Hz to 1 MHz, interfacial and dipole polarization mechanisms are dominant. During the mechanical degradation process distributed cracks formed

inside the material system. These cracks gave rise to interfacial polarization which leads to the observed increase in DRS.

For every set of samples, the average initial and damage DRS were calculated. Figure 6.6 shows the relationship between the difference of average damage state and initial DRS with damage state of the material system. The initial slope of the curve of Figure 6.6 is higher; it suggests that the rate of increasing polarization is higher, or in other words, the rate of creating new interfaces in the material is higher.

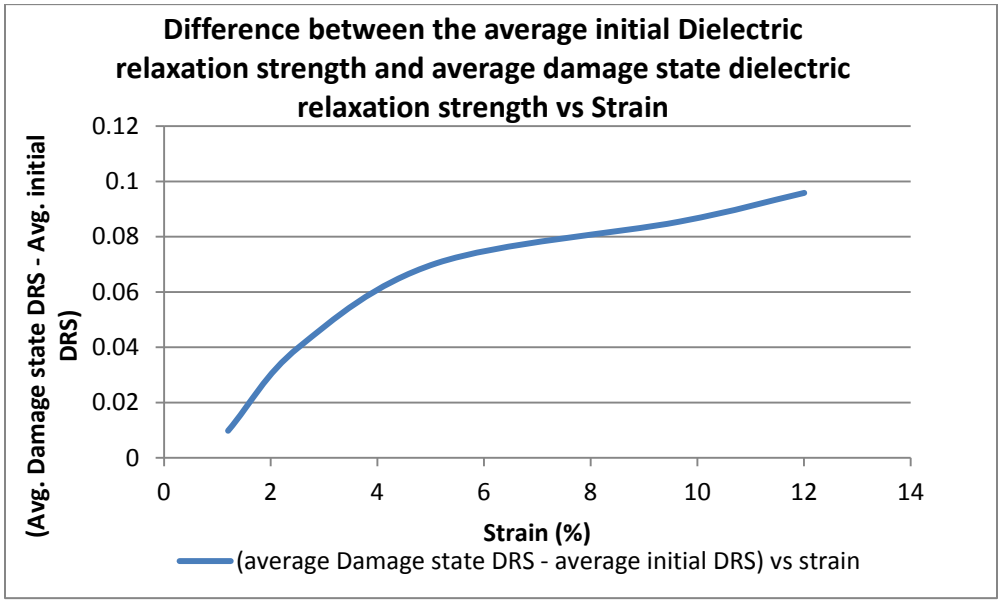

Figure 6.6 Average differences of undamaged and damaged state DRS with strain

For every sample dielectric properties were measured, (i) initially (in undamaged condition) (iii) just after unloading and (iii) after 2 weeks. After unloading, 2 samples from every set were kept at room conditions, and another 2 were kept in 5M NaCl solution; then after two weeks the dielectric properties were measured again. Figures 6.7 to 6.16 show the effect of mechanical degradation and environmental effects on the dielectric properties.

Mechanical and dielectric Properties of the sample 45s101.
Undamaged dielectric properties was measured and then sample was loaded till **1.5 kN** and after Unloading dielectric measurement was taken again and then sample was kept in **room environment**. Also after two weeks dielectric measurement was performed.

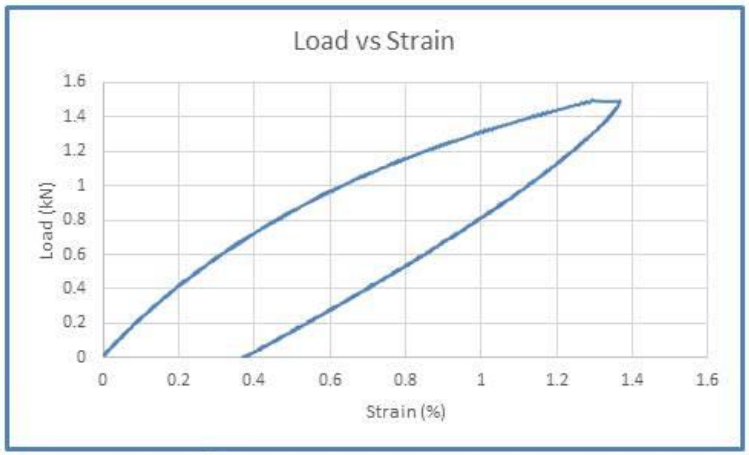

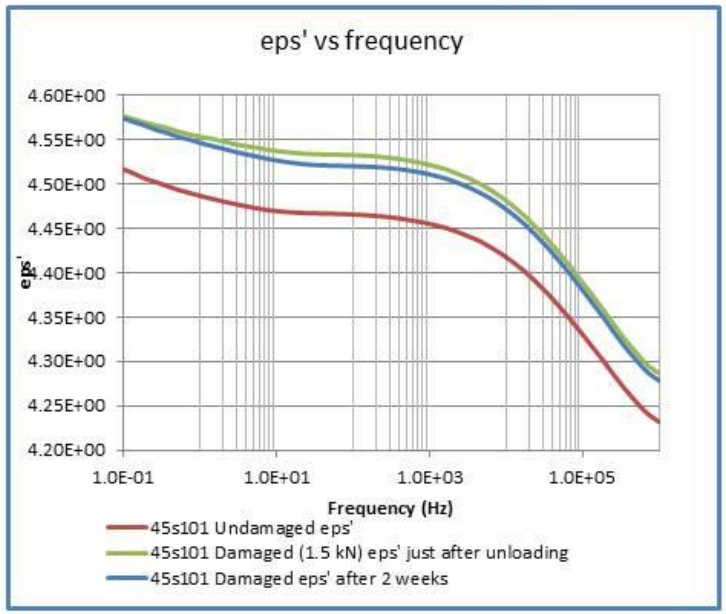

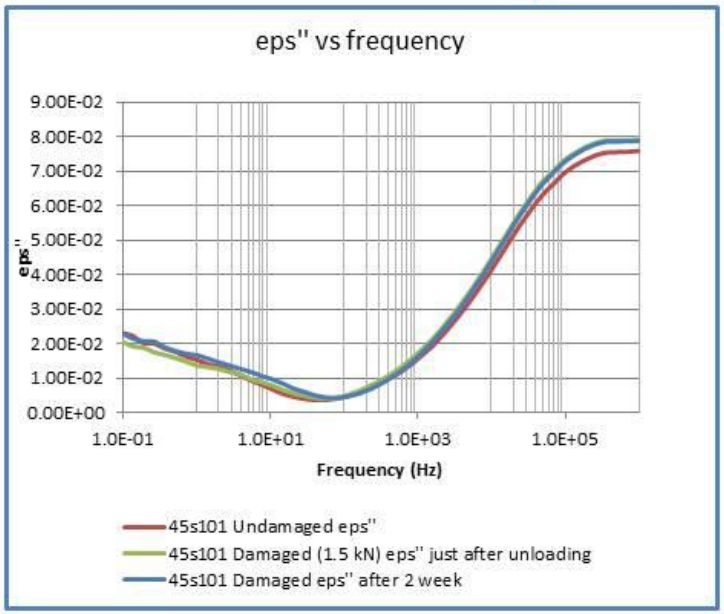

Figure 6.7 Mechanical and dielectric properties of the sample 45s101

Mechanical and dielectric Properties of the sample 45s103.
Undamaged dielectric properties was measured and then sample was loaded till **1.5 kN** and after Unloading dielectric measurement was taken again and then sample was kept in **5M NaCl** solution . Also after two weeks dielectric measurement was performed.

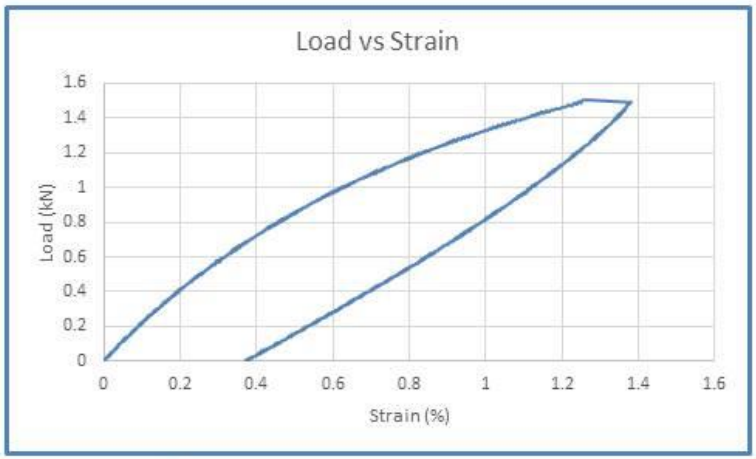

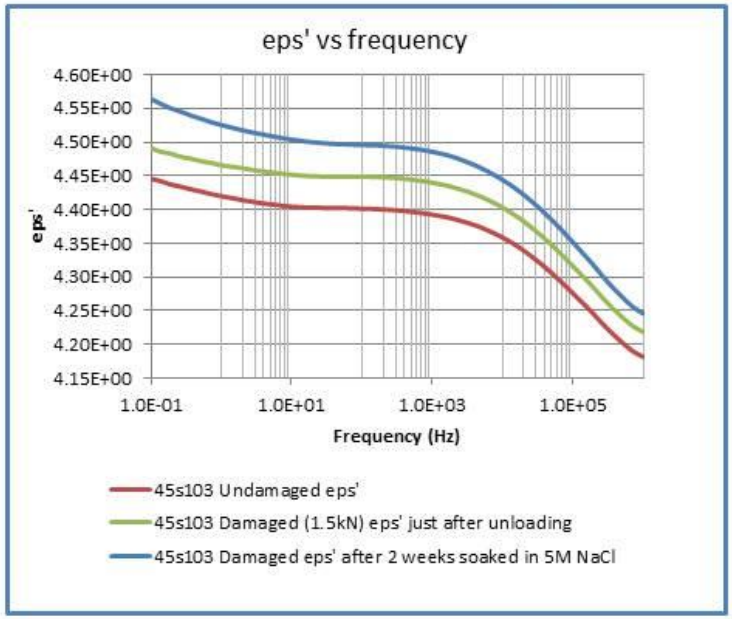

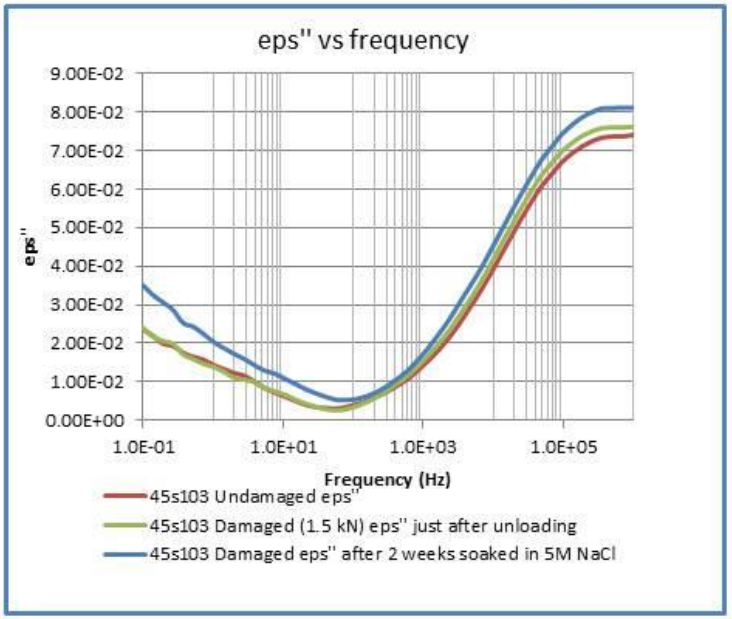

Figure 6.8 Mechanical and dielectric properties of the sample 45s103

Mechanical and dielectric Properties of the sample 45s105.
Undamaged dielectric properties was measured and then sample was loaded till **2 kN** and after Unloading dielectric measurement was taken again and then sample was kept in **room environment**. Also after two weeks dielectric measurement was performed.

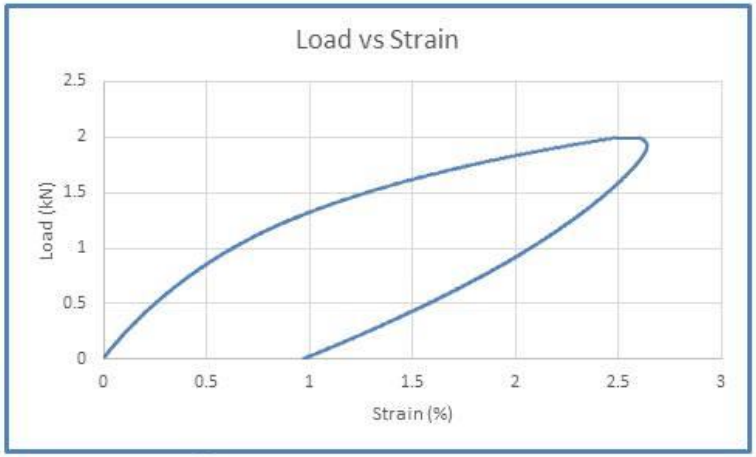

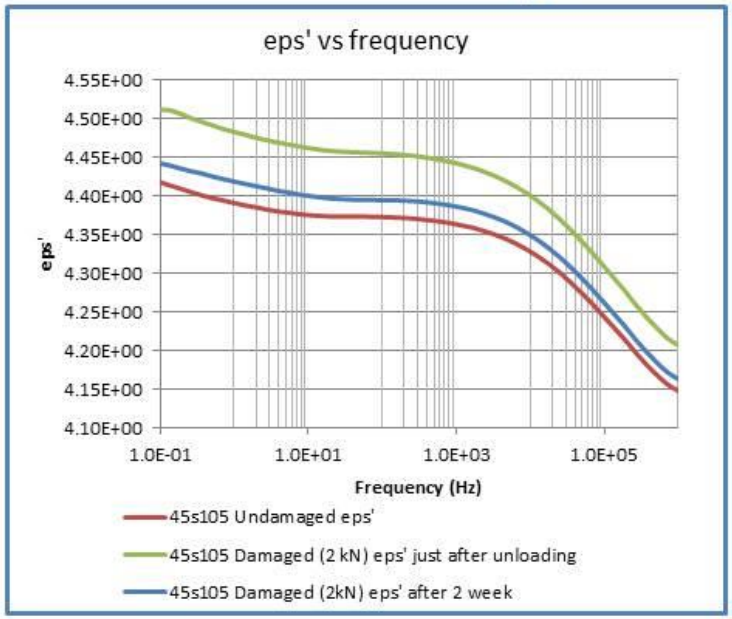

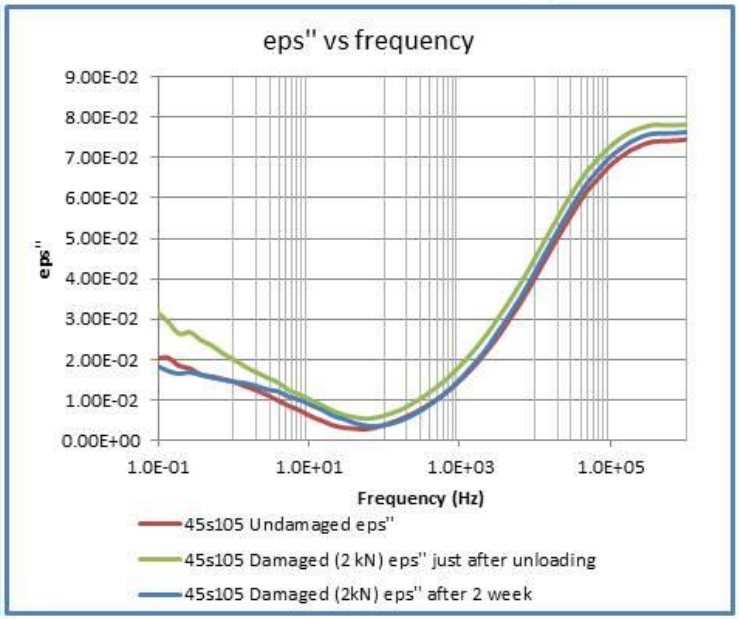

Figure 6.9 Mechanical and dielectric properties of the sample 45s105

Mechanical and dielectric Properties of the sample 45s107.
Undamaged dielectric properties was measured and then sample was loaded till **2 kN** and after Unloading dielectric measurement was taken again and then sample was kept in **5M NaCl** solution . Also after two weeks dielectric measurement was performed.

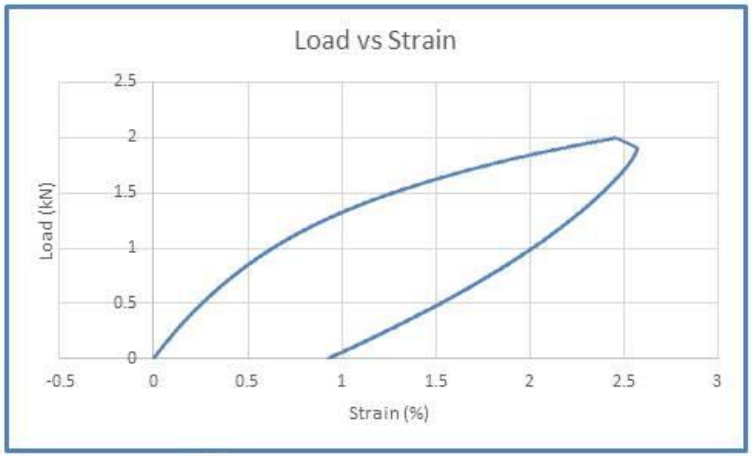

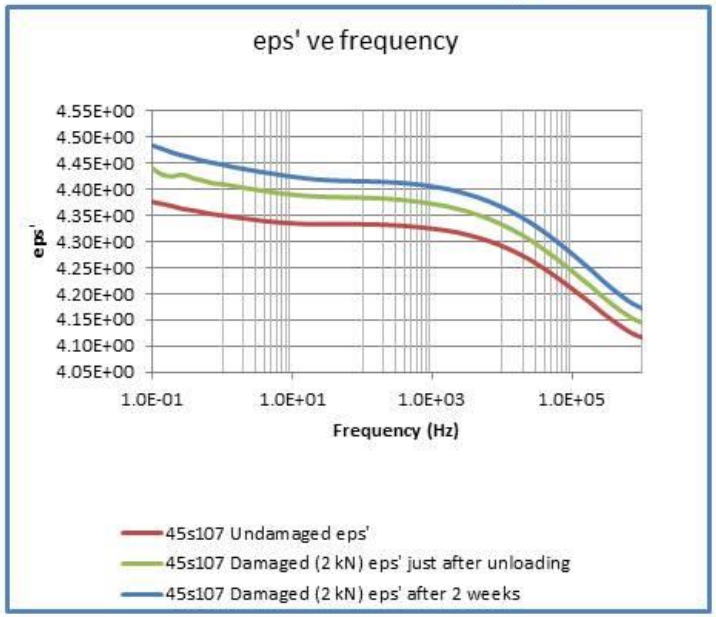

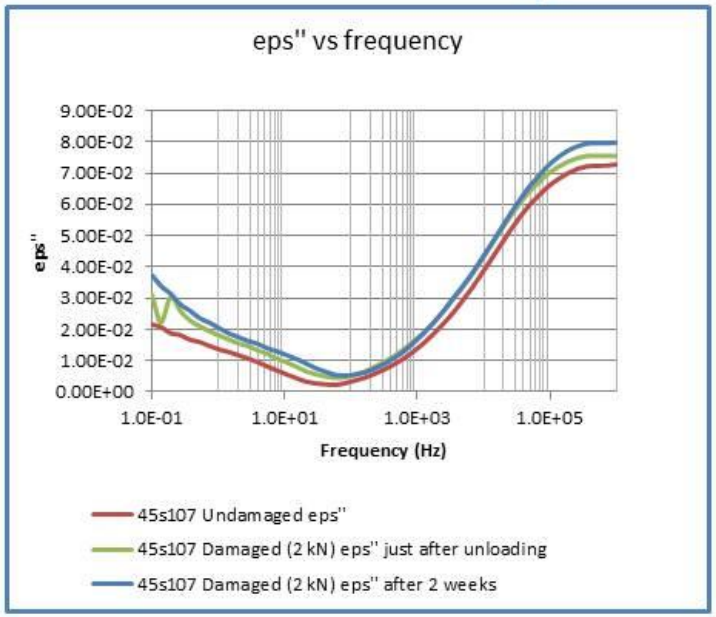

Figure 6.10 Mechanical and dielectric properties of the sample 45s107

Mechanical and dielectric Properties of the sample 45s109.
Undamaged dielectric properties was measured and then sample was loaded till **2.5 kN** and after Unloading dielectric measurement was taken again and then sample was kept in **room environment**. Also after two weeks dielectric measurement was performed.

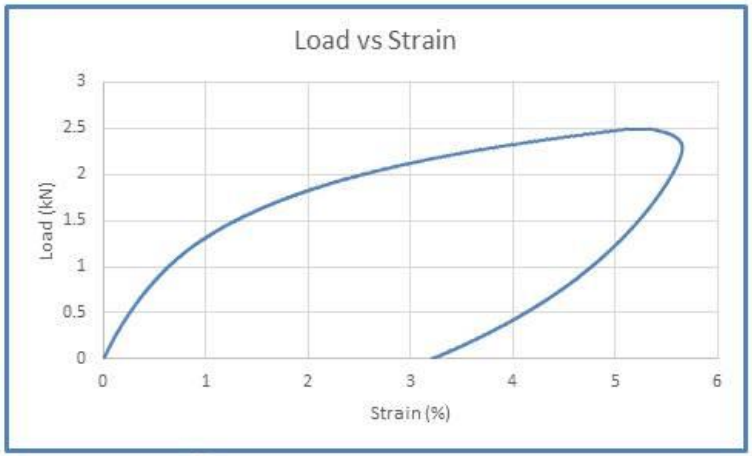

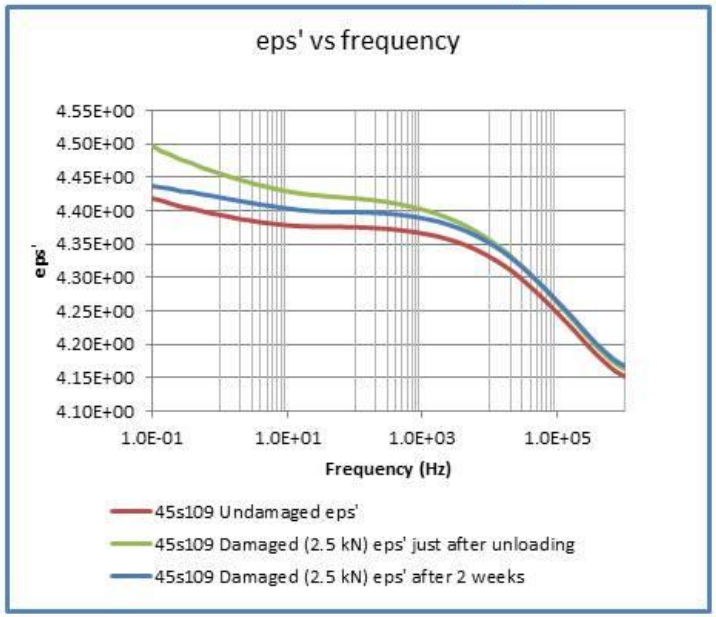

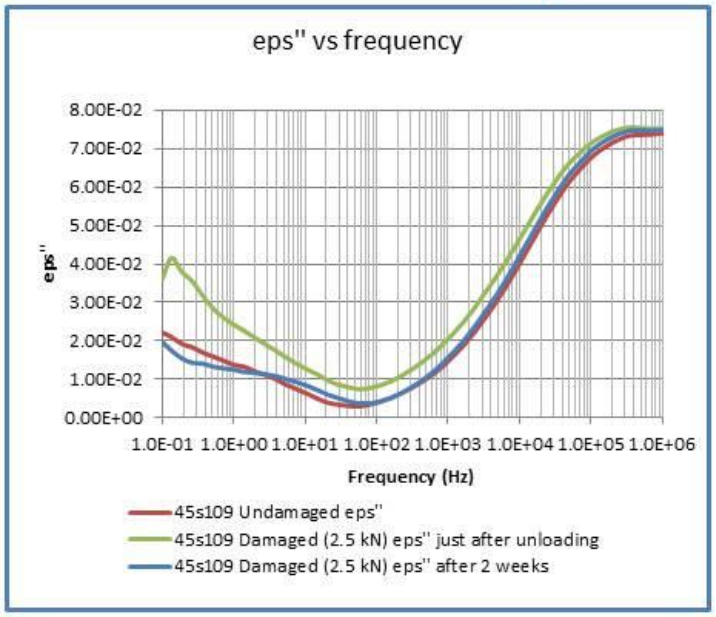

Figure 6.11 Mechanical and dielectric properties of the sample 45s109

Mechanical and dielectric Properties of the sample 45s111.
Undamaged dielectric properties was measured and then sample was loaded till **2.5 kN** and after Unloading dielectric measurement was taken again and then sample was kept in **5M NaCl** solution . Also after two weeks dielectric measurement was performed.

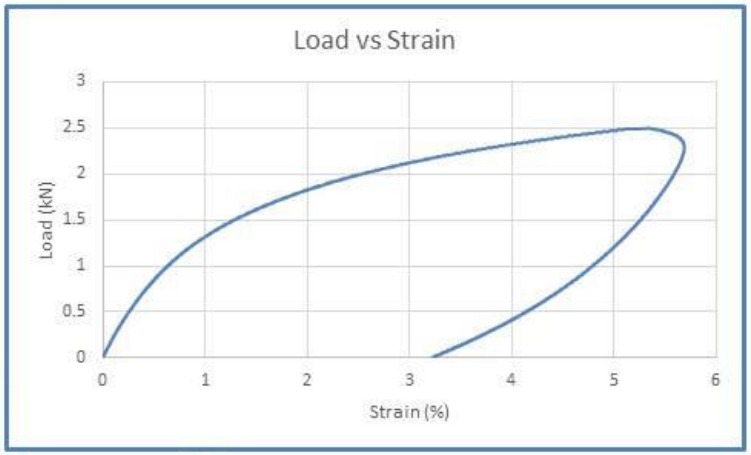

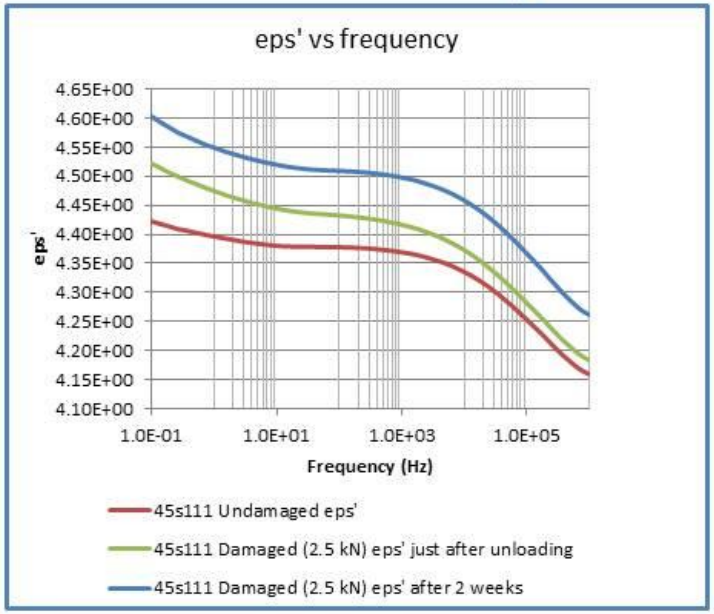

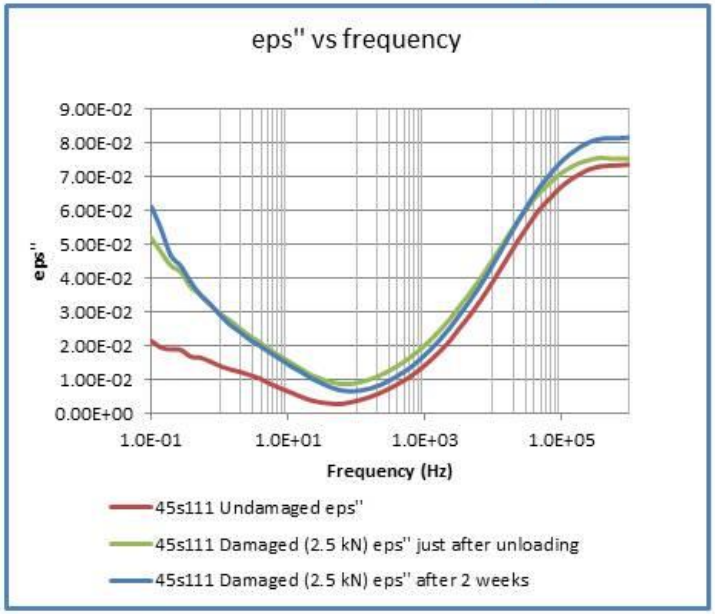

Figure 6.12 Mechanical and dielectric properties of the sample 45s111

Mechanical and dielectric Properties of the sample 45s113.
Undamaged dielectric properties was measured and then sample was loaded till **3 kN** and after Unloading dielectric measurement was taken again and then sample was kept in **room environment**. Also after two weeks dielectric measurement was performed.

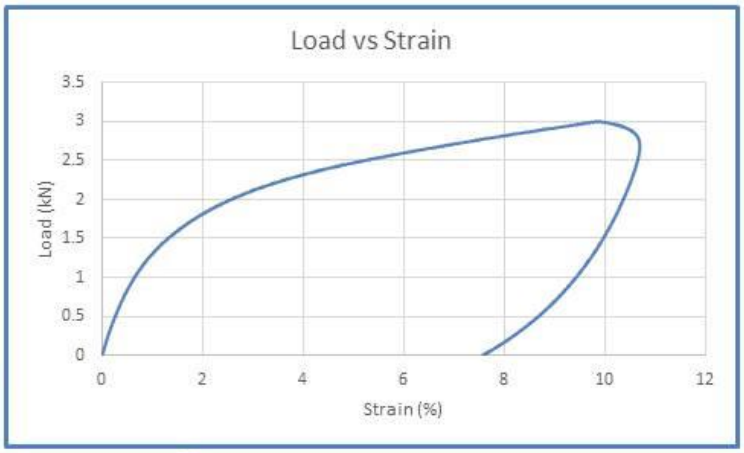

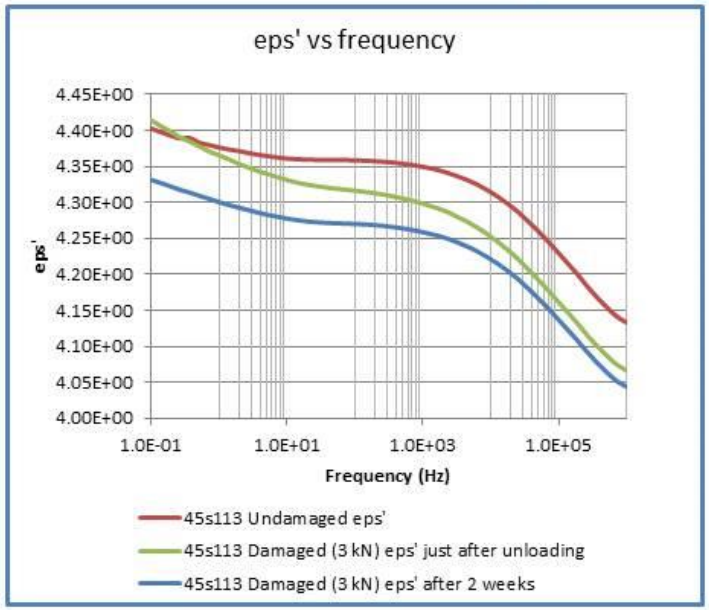

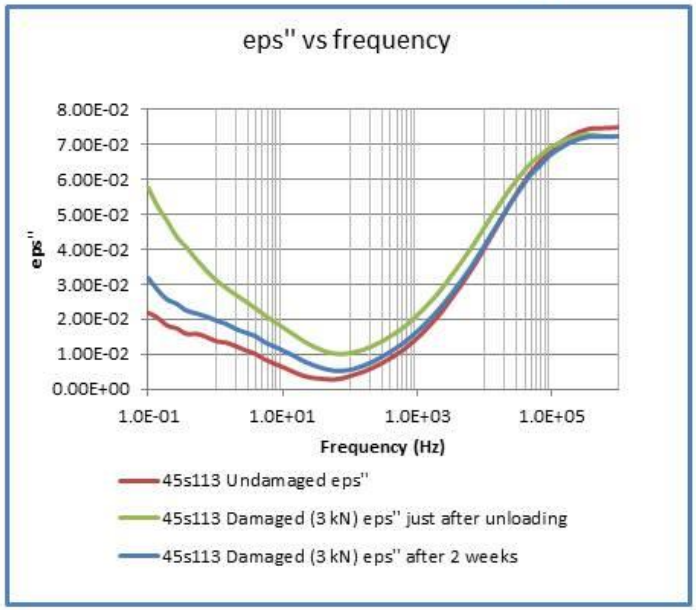

Figure 6.13 Mechanical and dielectric properties of the sample 45s113

Mechanical and dielectric Properties of the sample 45s115.
Undamaged dielectric properties was measured and then sample was loaded till **3 kN** and after Unloading dielectric measurement was taken again and then sample was kept in **5M NaCl** solution . Also after two weeks dielectric measurement was performed.

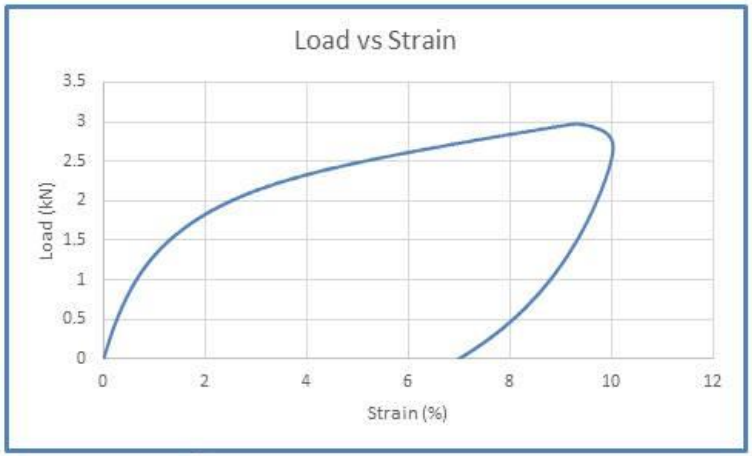

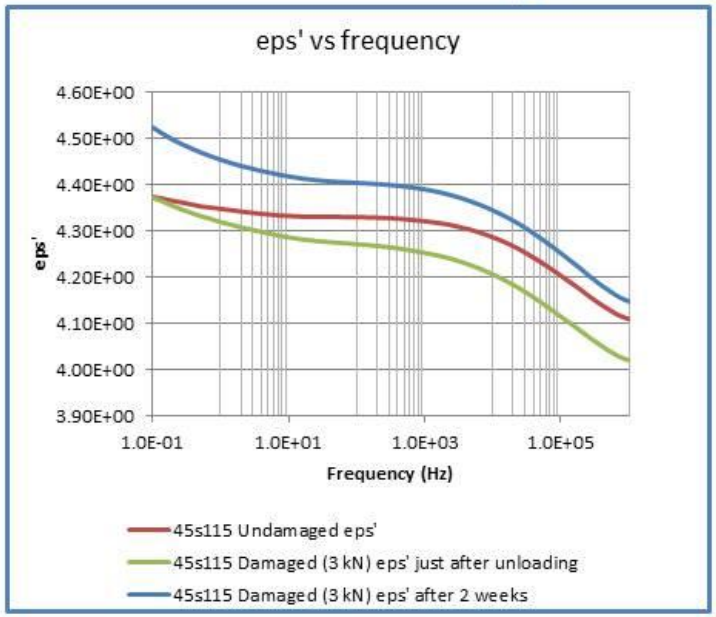

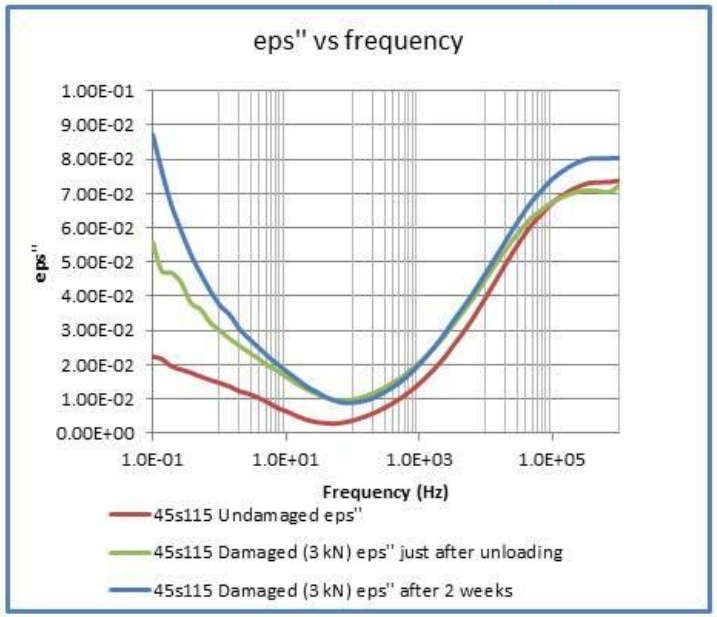

Figure 6.14 Mechanical and dielectric properties of the sample 45s115

Mechanical and dielectric Properties of the sample 45s118.
Undamaged dielectric properties was measured and then sample was loaded till **3.2 kN** and after Unloading dielectric measurement was taken again and then sample was kept in **room environment**. Also after two weeks dielectric measurement was performed.

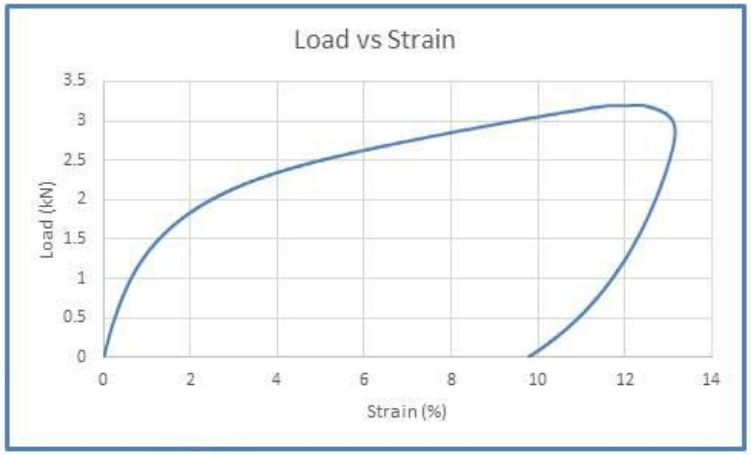

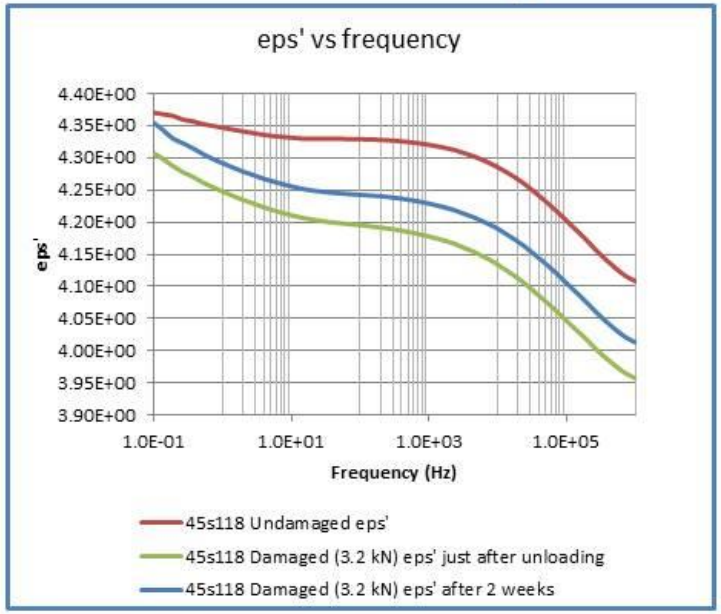

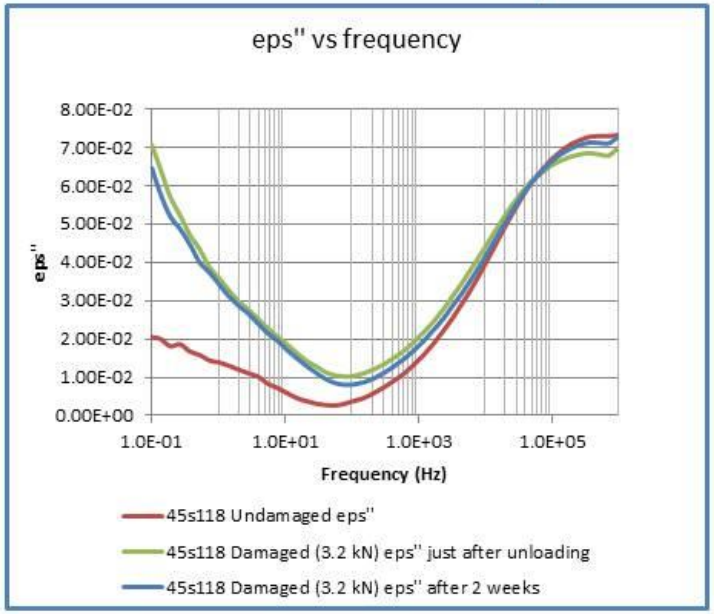

Figure 6.15 Mechanical and dielectric properties of the sample 45s118

Mechanical and dielectric Properties of the sample 45s119.
Undamaged dielectric properties was measured and then sample was loaded till **3.2 kN** and after Unloading dielectric measurement was taken again and then sample was kept in **5M NaCl** solution . Also after two weeks dielectric measurement was performed.

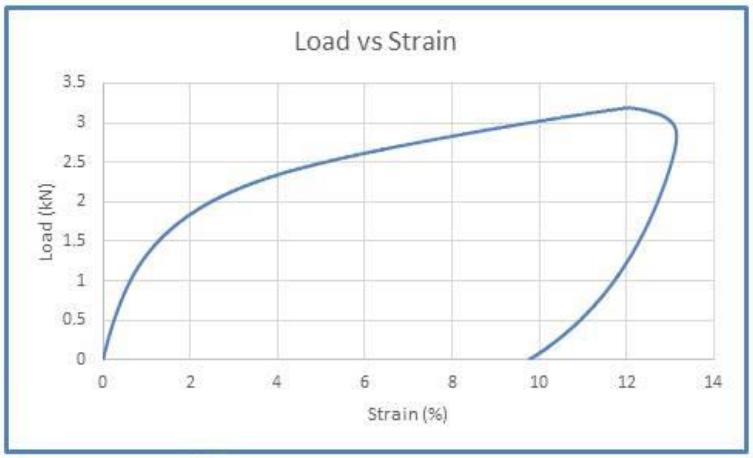

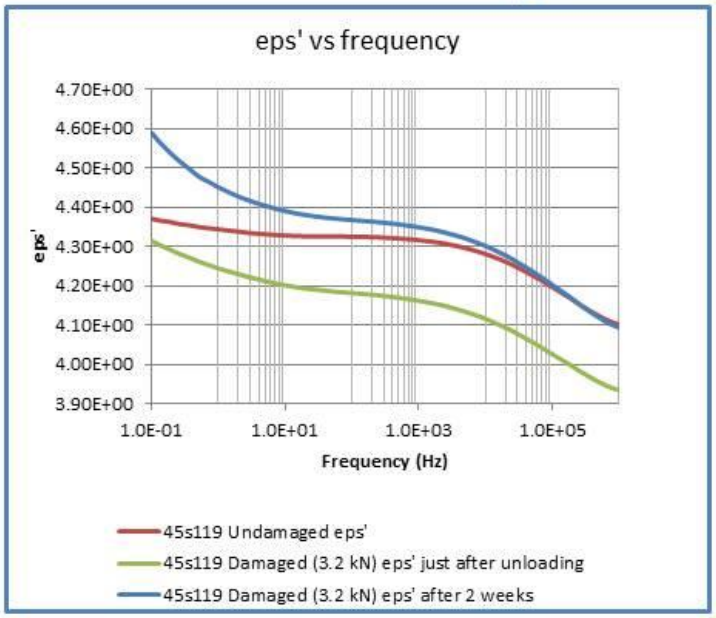

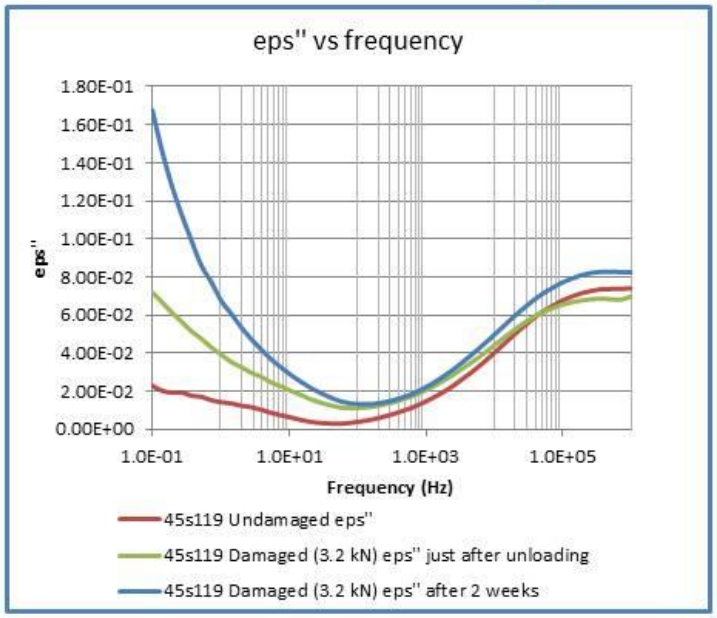

Figure 6.16 Mechanical and dielectric properties of the sample 45s119

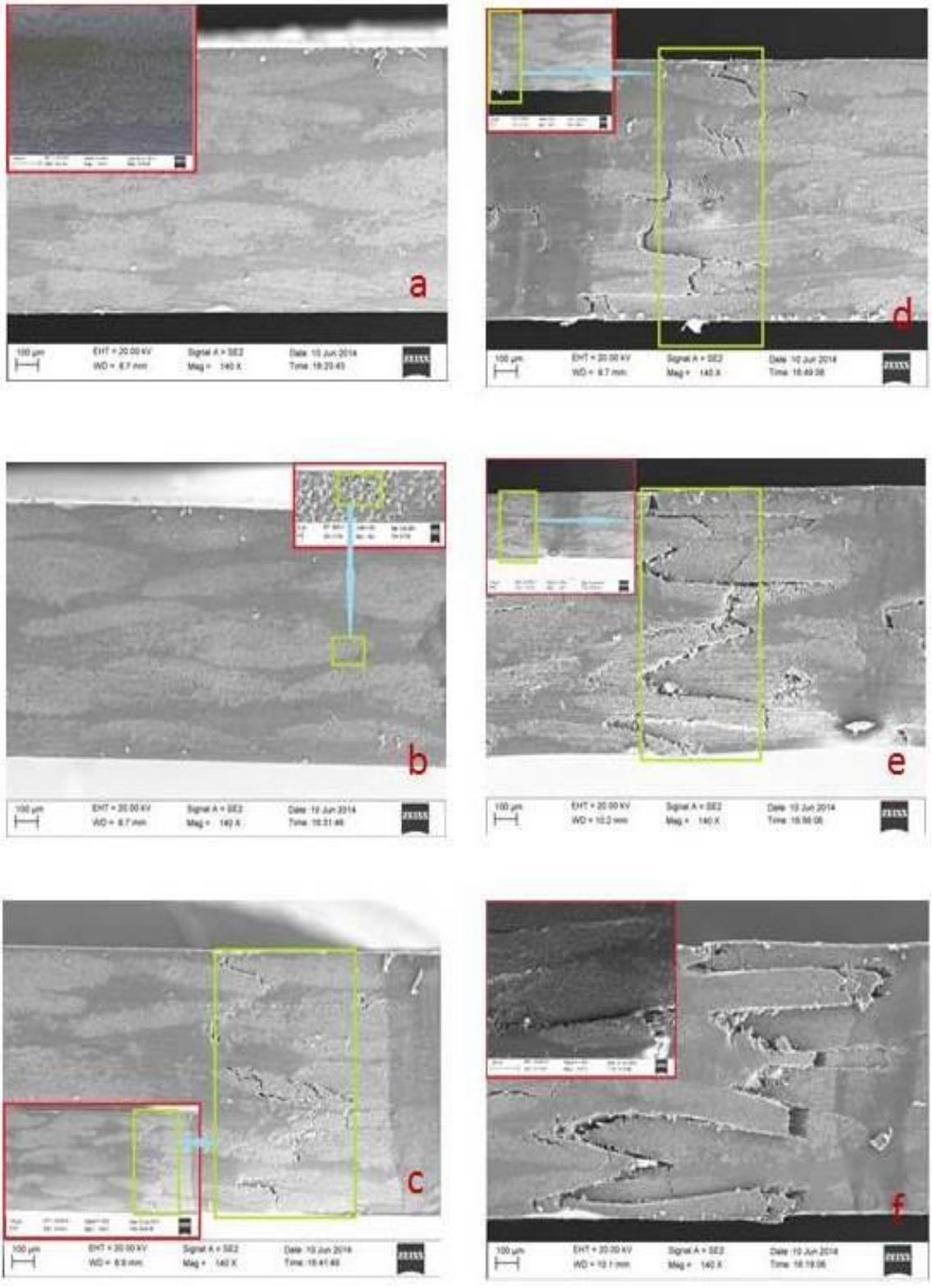

Figure 6.17 SEM images (a) undamaged, (b) 2 kN, (c) 2.5 kN, (d) 3 kN, (e) 3.2 kN (f) failed.

From above figures following things are observable;

- At low strain/load, just after unloading we saw subtle increases in the real part of the permittivity and at the high frequency end there is an increase in dielectric loss, as in Figure 6.7 to Figure 6.10. In chapter 5 we saw in edge replication images (which is an in-situ technique to capture cracks at the edge of the material sample) at low loads there were many distributed micro-cracks in the composite, and we also observe such cracks from the SEM images , Figure 6.17 (b), although the density is less in the SEM images since after unloading the material has had time to relax which leads to the closing of some of the microcracks created in the loading process. We believe that moisture that enters the material via microcrack fissures is adsorbed onto the epoxy surface of the microcracks, which increases the interfacial polarization that leads to increases of the real part of the permittivity. The increase in the dielectric loss at high frequency is also related to the dipole polarization of water/moisture inside the material. At low loads, the total surface fraction of the cracks dominats, rather than the volume fraction of the total cracks. Samples 45s101 and 45s105 were loaded to 1.5 kN and 2 kN respectively and then kept in ambient environment for two weeks so that the material had enough time to relax and close down the microdamage; that is why we observed a drop in the real part of the permittivity and imaginary part of the permittivity at low frequencies compared to the values we observed just after unloading, Figure 6.7 and Figure 6.9. Samples 45s103 and 45s107 were also loaded to 1.5 kN and 2 kN respectively, but just after unloading they were kept in a 5M NaCl solution. Then we can see a rise in both the real part

of the permittivity and the low frequency dielectric loss. This happens because more conductive salt solution diffused into the materials and that leads to more interfacial polarization. And a small rise in imaginary part of the permittivity at the high frequency also observed this is because of the dipole polarization of the water molecules of the solution.

- Samples 45s109 and 45s111 were loaded to 2.5 kN; after unloading, one was kept at room conditions and the second one was kept in a 5M NaCl solution.

- SEM images of a sample that was loaded to 2.5 kN shows bridging of microcracks, Figure 6.17 (c) which means that the volume fraction of the cracks begins to dominate, rather than the surface fraction of the cracks. For both samples we see just after unloading there is an increase in both the real and imaginary part of the permittivity which is prominent in the lower frequency part of the dielectric spectra which is an indication of higher interfacial polarization. Samples which were kept in room environments show a drop in both part of the permittivity, but other samples which were kept in 5M NaCl solution show opposite trends because of the increase of the conductive solution on the surface of the microcracks.

- SEM images of the sample which were loaded to higher load show that the delaminations and volume fraction of cracks increases a significant amount, Figure 6.17 (d) and (e). Though the real part of the permittivity drops because of the dominance of the volume fraction of the cracks compared to the surface fraction of the cracks, at low frequency the slope of the real part of the

permittivity measured just after unloading is higher than that measured initially. On the other hand, the low frequency dielectric loss increased a significant amount. Samples that were kept in room environments showed the usual drop in both real part of the permittivity but not much decrease in the dielectric loss at low frequency. Samples that were kept in a 5M NaCl solution showed very high increases of both real and imaginary parts of the permittivity, because of the conductive solution that was able to enter the material.

6.6 Dielectric measurements after heat treatment

Two sets of samples were used for this experiment and every set had 5 samples. Two types of thermal treatment were done, (i) One set of samples was placed in the furnace at 130 deg C for 5 min.; then those samples were placed in room temperature water and this was done 5 times. (ii) another set of samples was cycled 10 times from temperature 130 deg C to 40 deg C.

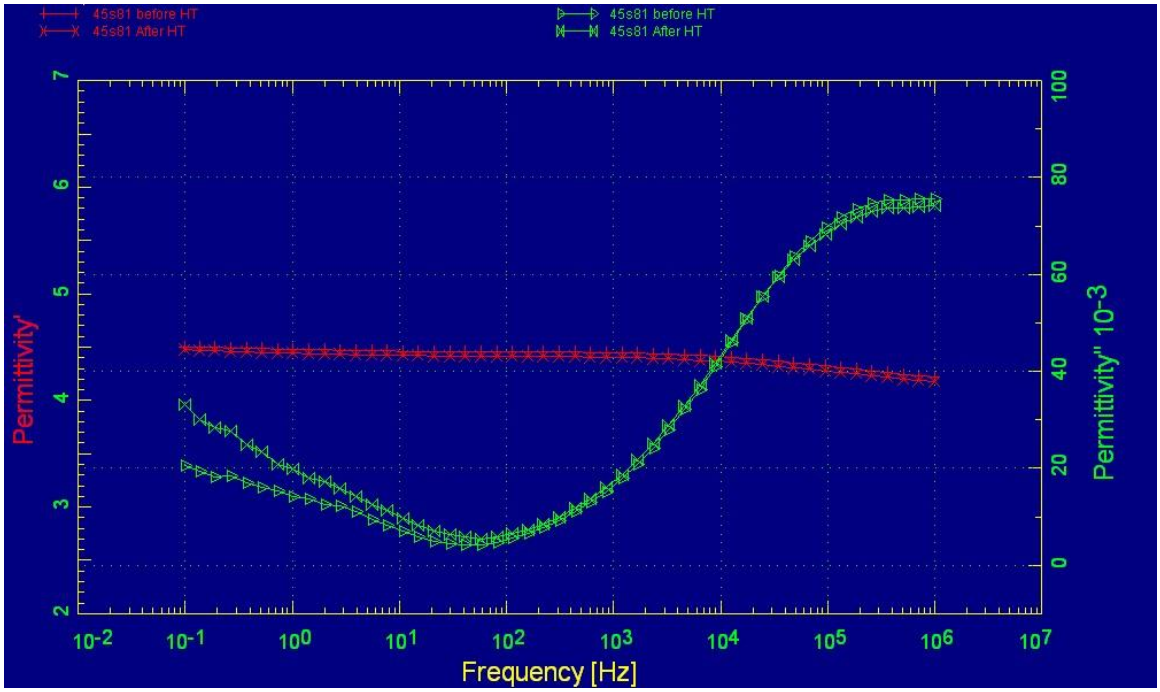

Figure 6.18 Dielectric properties after heat treatment

Woven glass/epoxy composite samples were used for the heat treatment experiment; because of the thermal mismatch between glass fibers and epoxy there is a possibility that there will be interfacial degradation between fiber and matrix which may lead to a dielectric loss increase in the lower frequency range of BbDS, Figure 6.18.

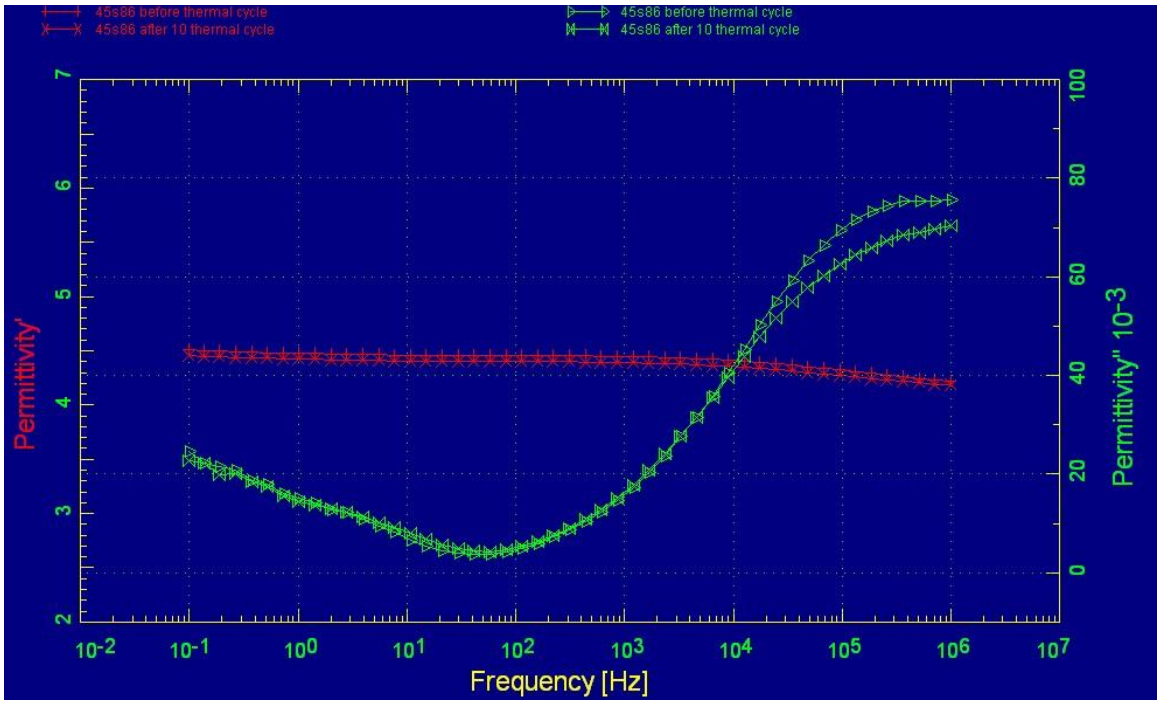

Figure 6.19 Dielectric properties after thermal cycle

Because of the thermal cycling, the percentage of water content inside the material decreased; that is why at the high frequency end of BbDS there is drop in dielectric loss which is related to dipole polarization of the water molecules, figure 6.19.

6.7 Prognosis

6.7.1 Relationship of Dielectric State to Material State

In composite material systems, there are many initial interfaces, and as material damage develops, many new interfaces and surfaces develop. We have shown that each

of these surfaces and interfaces is a location of charge accumulation (and possible motion), and that there is a corresponding change in the local electric field as one passes from one phase to another[99-100]. Moreover, Reifsnider et al.,[101] have shown that the amount of local charge and local field can be calculated from first principles if the properties and morphology of the local phases are known. Hence, the measured permittivity or susceptibility of a given composite material is a state variable that is determined by how the composite is designed and manufactured, initially, and by what changes that material state as defects develop – uniquely according to the history of a given specific physical sample.

In previous chapters and the previous sections of the chapter we have defined a number of parameters that are used to measure and represent the dielectric properties of a material or material system. Those parameters typically include the complex values of dielectric constant or susceptibility, conductivity, capacitance, and various combinations and ratios of those quantities such as the "electric modulus," "dielectric relaxation strength," etc. But how does that help us? Are the dielectric properties related, directly and uniquely, to the mechanical properties of a sample, e.g., are they 'predictors' of strength, life, and durability?

Since dielectric properties should be state variables of a material (unique observables for a given material state), if we can show that one or more of our parameters is directly related to mechanical state variables of interest (e.g., strength, life, stiffness), then it may be possible to directly estimate mechanical properties and behavior from dielectric measurements, for specific specimens, i.e., to sort 'good' specimens from 'bad,' to rank the order of strength and life of a given random sample of specimens, etc.,

before the specimens (or airplanes, etc.) are broken. It would be very valuable, for example, to know "which airplane is going to fail next" in a fleet based on nondestructive dielectric measurements of the as-manufactured material state in each airplane, perhaps as a basis for condition based maintenance, etc. There are many other ways such information can be of great value.

We will consider only the mechanical behavior of plain weave, glass reinforced epoxy coupon specimens, generally five plies thick, 18 mm wide, and 75 mm long in the gage section. Our first evidence considered comes from a series of 50 tests in which many dielectric properties were measured on the as-manufactured specimens, and then compared, for each specimen individually, to the break stress or break strain of those specimens. An example of the results of those experiments is shown in Figure 6.20

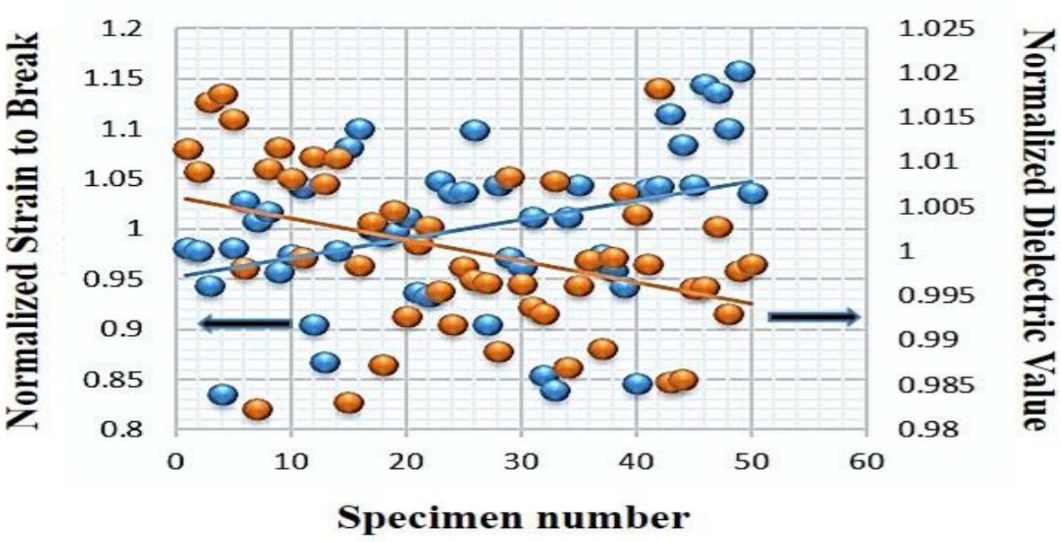

Figure 6.20 Strain to break and corresponding values of initial dielectric permittivity (real part), as vertical pairs, and trend lines showing that there is an inverse relationship between those quantities, with very high significance.

For the example data shown in Fig. 6.20, 39 of the 50 individual pairs of data support the hypothesis that there is an inverse relationship between break strain and the

initial value of the real part of the material permittivity, with very high significance (the two tailed Chi squared P value is less than 0.0001). Other dielectric factors also show good correlation, but this one seems to be best of those tested. It tells us that, with very high reliability, when the dielectric permittivity of a specimen is high, indicating high values of internal polarization, the resulting strain to break is low for that specimen.

A second series of tests was conducted in which sets of 20 specimens were characterized initially by their dielectric properties, and then tested to failure in quasi-static uniaxial loading. The average value of the mechanical strength and strain to break of all specimens tested was compared to the measured value for each individual specimen, and those data were ranked according to their fraction of that average. The average value of the dielectric property of that sample set was then compared to each individual specimen value and those fractions were ranked. Then those respective ranks were compared; an example of those results is shown in Figure 6.21. The maximum error in the predictions of individual specimen strain to break values shown is about seven percent.

These measurements were made as a function of frequency to help us to identify the mechanisms of charge polarization contributing to the interpretation, and thereby, the mechanisms of damage and defects controlling the subsequent physical behavior. Figure 6.22 shows a sequence of three such frequencies of testing for comparison. For the low frequencies discussed here, the correlations are not strongly dependent on frequency of the input electric field. However, our experience has been that low frequency response is more closely tied to the physical damage mechanisms.

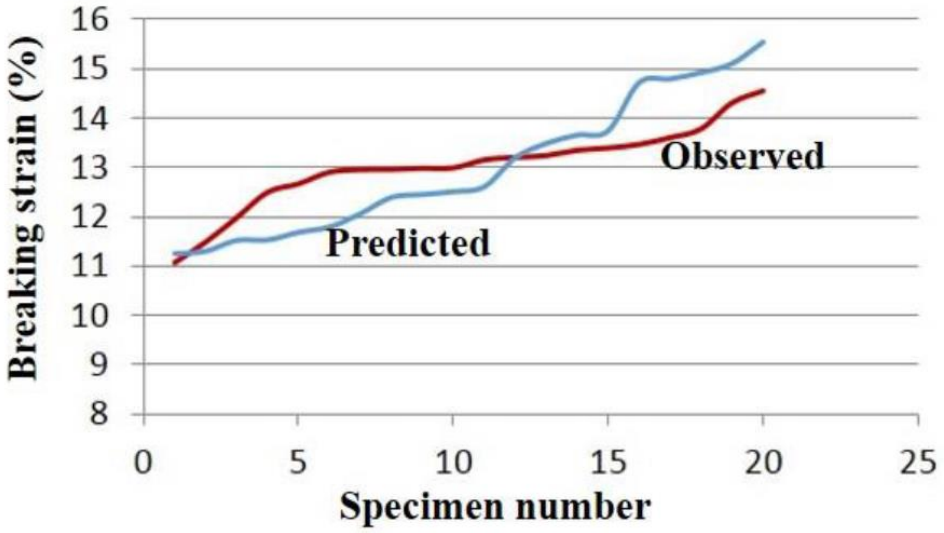

Figure 6.21 Observed and predicted values of strain to break for 20 individual specimens based on initial values of the imaginary part of the permittivity measured through the thickness of those individual specimens before load application

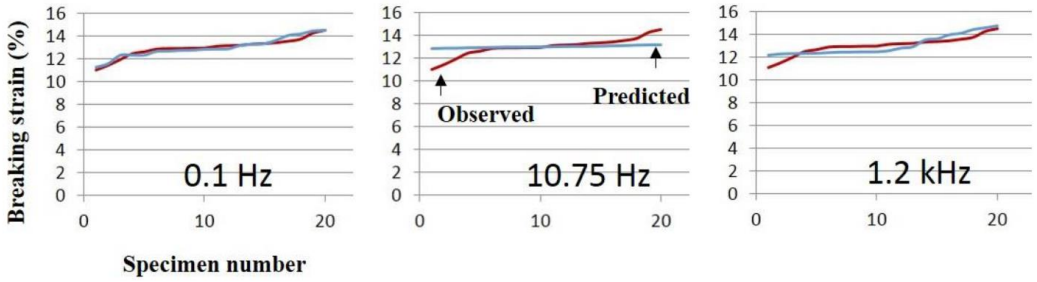

Figure 6.22 Observed and predicted values of strain to break for 20 individual specimens based on initial values of the imaginary part of the permittivity measured through the thickness of those individual specimens before load application for different input frequencies.

6.7.2 Identify a weak area based on the dielectric data

Ten samples were used to identify the weakest part of the sample based on initial dielectric data. Every sample was painted with silver paste in three locations and after curing the paint initial dielectric measurement was taken with a round electrode then all the samples were pulled till failure.

Out of 10 samples 4 samples broke where dielectric relaxation strength is higher. One sample failed between two higher dielectric relaxation strengths but far from the lowest dielectric strength. Three samples failed near the area where dielectric relaxation strength is in between the maximum and minimum dielectric relaxation strength and two samples failed near the area where dielectric relaxation strength is lowest.

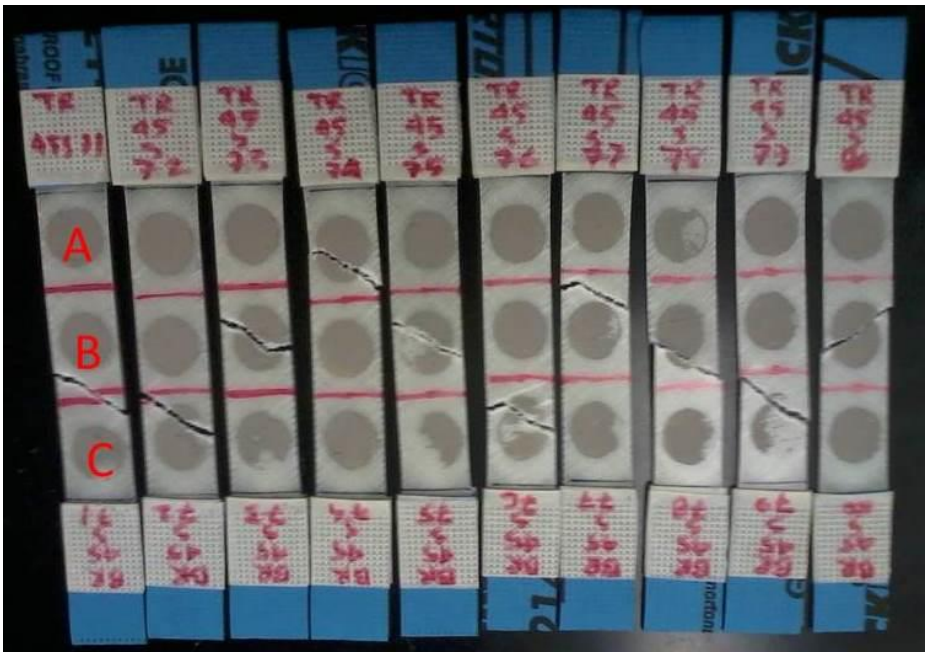

Figure 6.23 Samples tested to identify weak area.

It is not definite but here is a trend that material failed around the area where dielectric relaxation strength is higher. Higher DRS means more interfacial polarization. DRS is expected to be same for all part of the same material. If some parts have microdects and void than the other parts then there is possibility to rise in DRS and microdefects and voids part is the vulnerable part of the material system.

6.8 Summary

In this chapter we saw how the dielectric spectra changes with the material degradation under mechanical, thermal and environmental conditions. From this chapter

it is also evident that the dielectric properties of a composite material provide state variables (observables specific to the material state of specific samples of material) that uniquely define mechanical properties such as strength, life, and durability.

CHAPTER 7 NUMERICAL ANALYSIS

Composite materials are by nature heterogeneous material and consist of chemically different constituents whose morphologies have greater impact on the electric, thermal and mechanical properties. When composite materials go through degradation processes, the morphology of the constituents is changed by introducing new phases in the material system and also by changing the interfaces of the materials constituents. Dielectric properties of the composite materials depend on the space distribution of the phases including voids and cracks inside the materials system. Because of the heterogeneity of the composite materials in the relaxation of the Broadband Dielectric Spectroscopy interfacial polarization, which is known as Maxwell-Wagner-Sillar polarization, is the prominent mechanism which happens in the low frequency range due to the charge accumulation at the interphases of the material system.

There are many examples of using a finite element method (FEM) to model the effective dielectric properties of periodic and random composites containing inclusions of various shapes [102-103]. Tuncer et al. used FEM for 2D binary composite to model dielectric relaxation [86].

In the present work, a computer FEM simulation is performed by using the COMSOL Multiphysics^{TM} to observe the dielectric property changes with the increase and distribution of the inclusion, which here considered as crack in composite, in the frequency domain. To reduce the complicacy in this model, the permittivity and conductivity of the inclusions and material are considered to be frequency independent

and the dielectric loss is considered as purely ohmic, i.e., it is considered that the only polarization mechanism that is present is interfacial polarization.

7.1 Basic Theory

In dielectrics relation between the applied electric field **E** and the dielectric displacement **D** is linear and can be expressed as,

$$\mathbf{D} = \varepsilon_o \varepsilon_r \mathbf{E} \qquad 7-1$$

Where, ε_o is the permittivity of the free space and ε_r is the relative permittivity of the dielectrics.

If ρ is the charge density, from Maxwell equations we know that dielectric displacement follows the following relation

$$\boldsymbol{\nabla}.\mathbf{D} = \rho \qquad 7-2$$

For current density **J** we can get the following from the continuity equation

$$\boldsymbol{\nabla}.\mathbf{J} = -\frac{d\rho}{dt} \qquad 7-3$$

From also Ohm's law we know

$$\mathbf{J} = \sigma \mathbf{E} \qquad 7-4$$

Here σ is the conductivity of the material.

So from equation 7-2 and 7-3 we get

$$\boldsymbol{\nabla}.\left(\mathbf{J} + \frac{d\mathbf{D}}{dt}\right) = 0 \qquad 7-5$$

Now using 7-1, 7-4 and 7-5 we can have the following

$$\boldsymbol{\nabla}.\left(\sigma\mathbf{E} + \frac{d(\varepsilon_o \varepsilon_r \mathbf{E})}{dt}\right) = 0 \qquad 7-6$$

In case of sinusoidal electric field **E** of angular frequency ω

$$\boldsymbol{\nabla}.(\sigma + i\omega\varepsilon_o\varepsilon_r)\mathbf{E} = 0 \qquad 7-7$$

We know

$$\mathbf{E} = -\nabla\Phi \qquad 7-8$$

From equation 7-7 and 7-8 we get

$$\nabla.\left[(\sigma + i\omega\varepsilon_o\varepsilon_r)\nabla\Phi\right] = 0 \qquad 7-9$$

From equation 7-9, we can tell that in a heterogeneous material the product of the physical properties (some form of the conductivity and permittivity) and the slope of the potential must be a constant as we cross material boundaries. For the quasi-static case with harmonic inputs fields, the gradient of that product vanishes. The interacting field is a result of the charge difference at the interface, and unless the conductivity and permittivity of adjacent material phases are identical, there is a disruption of charge transfer at the material boundary which results in internal polarization.

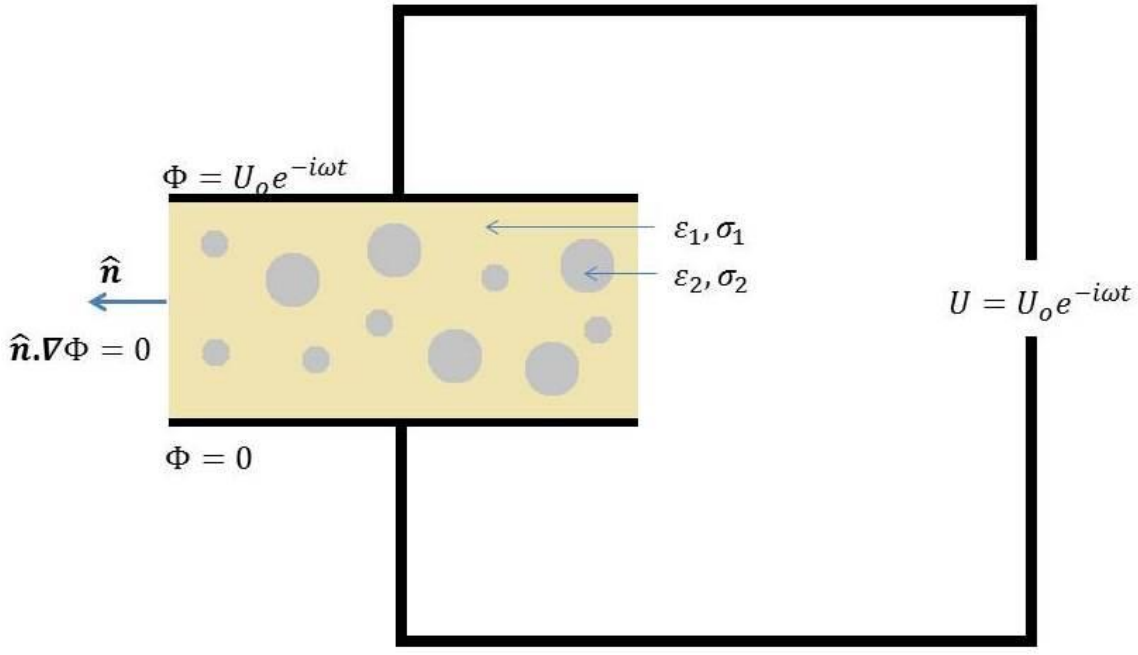

Figure 7.1 Schematic of the calculation of effective dielectric properties of composites.

To solve equation 7-9 potential on the top electrode is,

$$\Phi = U = U_o e^{-i\omega t} \qquad 7-10$$

And on the bottom electrode,

$$\Phi = 0 \qquad 7-11$$

Boundary conditions on the interfaces are,

$$\Phi_1 = \Phi_2 \qquad 7-12$$

$$\varepsilon_1 \hat{\mathbf{n}}.\boldsymbol{\nabla}\Phi_1 = \varepsilon_2 \hat{\mathbf{n}}.\boldsymbol{\nabla}\Phi_2 \qquad 7-13$$

Where $\hat{n}$ is the unit vector normal to the interface surface. To eliminate fringe effect on the side plane,

$$\hat{\boldsymbol{n}}.\boldsymbol{\nabla}\Phi = 0 \qquad 7-14$$

Here $\hat{n}$ is the unit vector normal to the side plane.

7.2 Results and Discussions

7.2.1 Two Phase Model

For this model undamaged composite material is considered as a homogeneous materials and the cracks (here as circular inclusions) are considered as the second phase inside the homogeneous material system. Permittivity and ohmic conductivity of the host material were taken to be $\varepsilon_1 = 5$ and $\sigma_1 = 10^{-13}$ S/m and for the inclusion permittivity and ohmic conductivity, $\varepsilon_2 = 2$ and $\sigma_2 = 10^{-15}$ S/m, were chosen close to the ambient air permittivity and conductivity. Because of the difference in the permittivities and conductivities of the phases, the accumulation of charge at the interphase boundaries causes an undulation of the space distribution of the potential which is shown in the figure 7.2 and Figure 7.3. In the figure 7.2 shows the potential distribution around the inclusion and figure 7.3 shows the potential distribution along the line and it is visible

that around the boundary of the phases there is a potential nonlinearity (in the picture nonlinearity is shown inside two ellipse) which is caused by the charge accumulation at the interface on host material and inclusion. Figure 7.4 shows that the space charge accumulation is higher, which is caused by the dissimilarity of the material properties around the inclusion boundary in the presence of the applied electyric field.

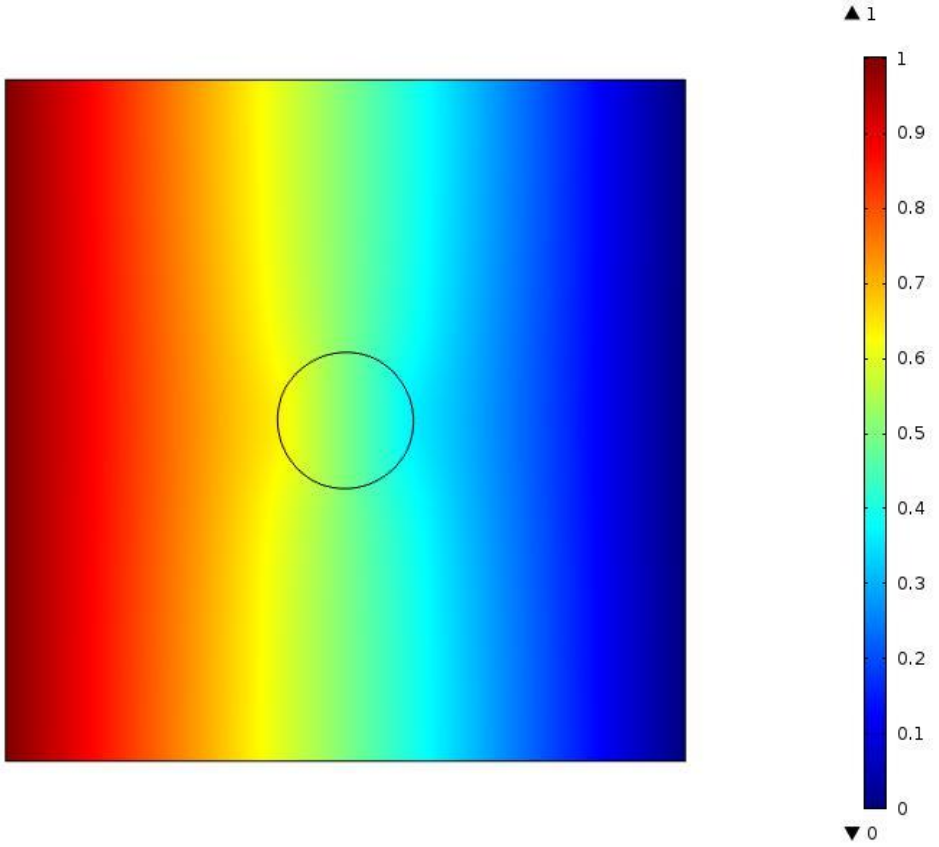

Figure 7.2 Potential distributions around the inclusion

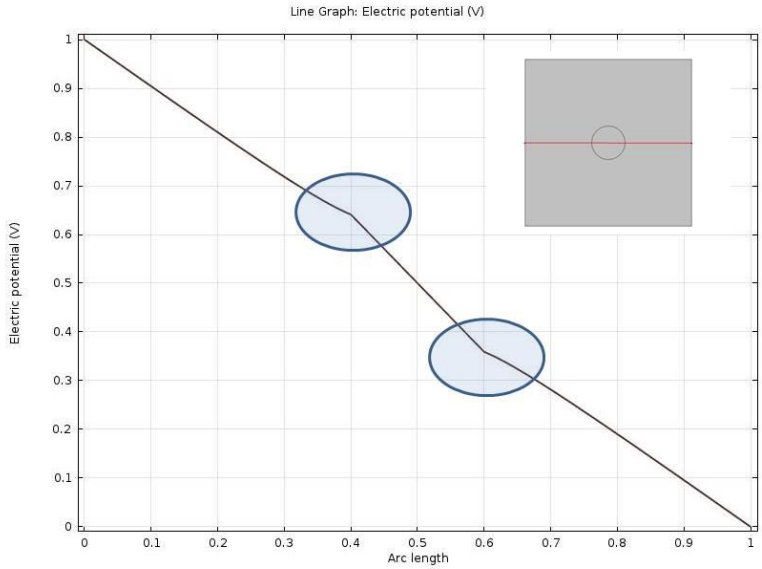

Figure 7.3 Potential distributions along the line.

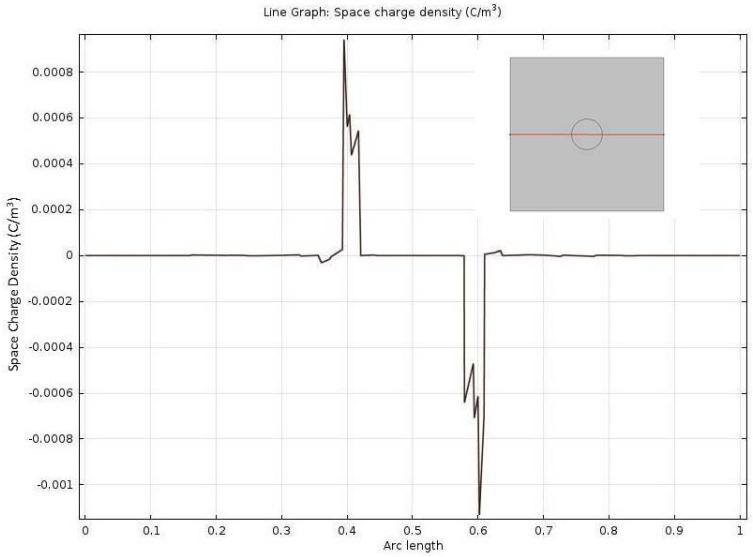

Figure 7.4 Space charge densities along the line.

Computer simulation was performed for different volume fraction of the inclusion. Figure 7.5 shows space charge density increases with the increase of the inclusion volume fraction. In the frequency range above 1 Hz the space charge density is constant but below 1 Hz a nonlinear increase is observed in the space charge density around the inclusion interface as shown in figure 7.6.

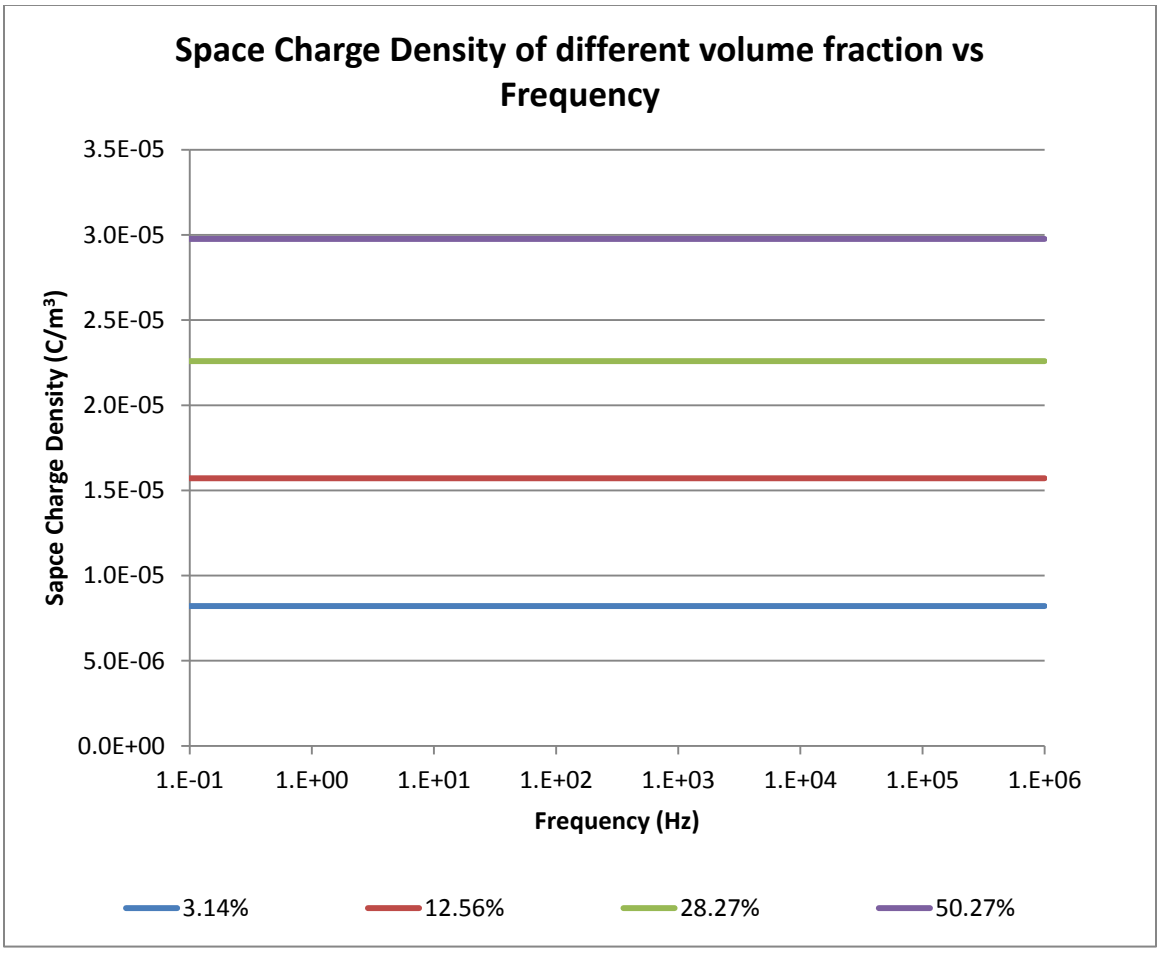

Figure 7.5 Space charge densities around the inclusion interface of different volume fraction in different frequency.

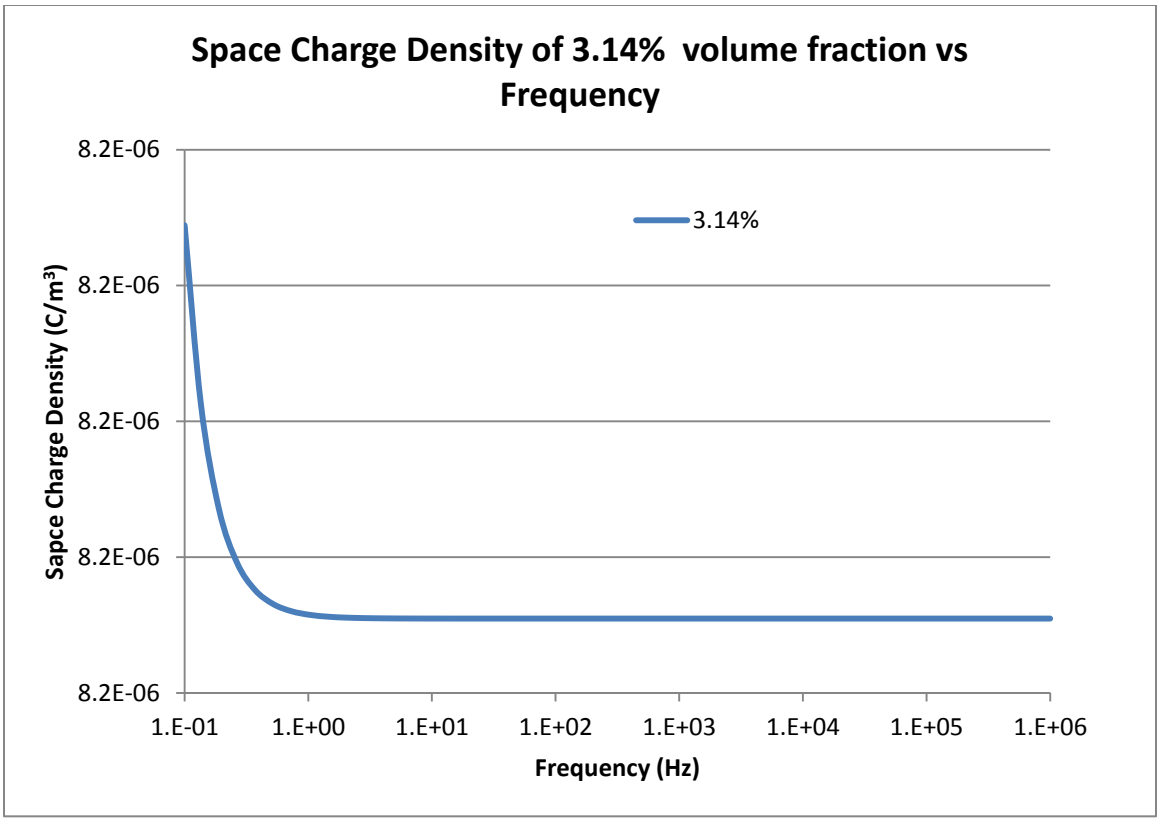

Figure 7.6 Space charge density change of 3.14% volume fraction of inclusion with frequency.

Figure 7.7 shows the change of real and imaginary part of permittivities with the increase of volume fraction of the inclusion with frequency. At a high frequency the period of potential oscillations is not sufficient for charge accumulation but at low frequency charge has enough time to accumulate around the interface which leads to interfacial polarization (Maxwell-Wagner-Sillar polarization) and that is why there is an increase in real part of the permittivity (shown in figure 7.8) and dielectric loss in the lower frequency.

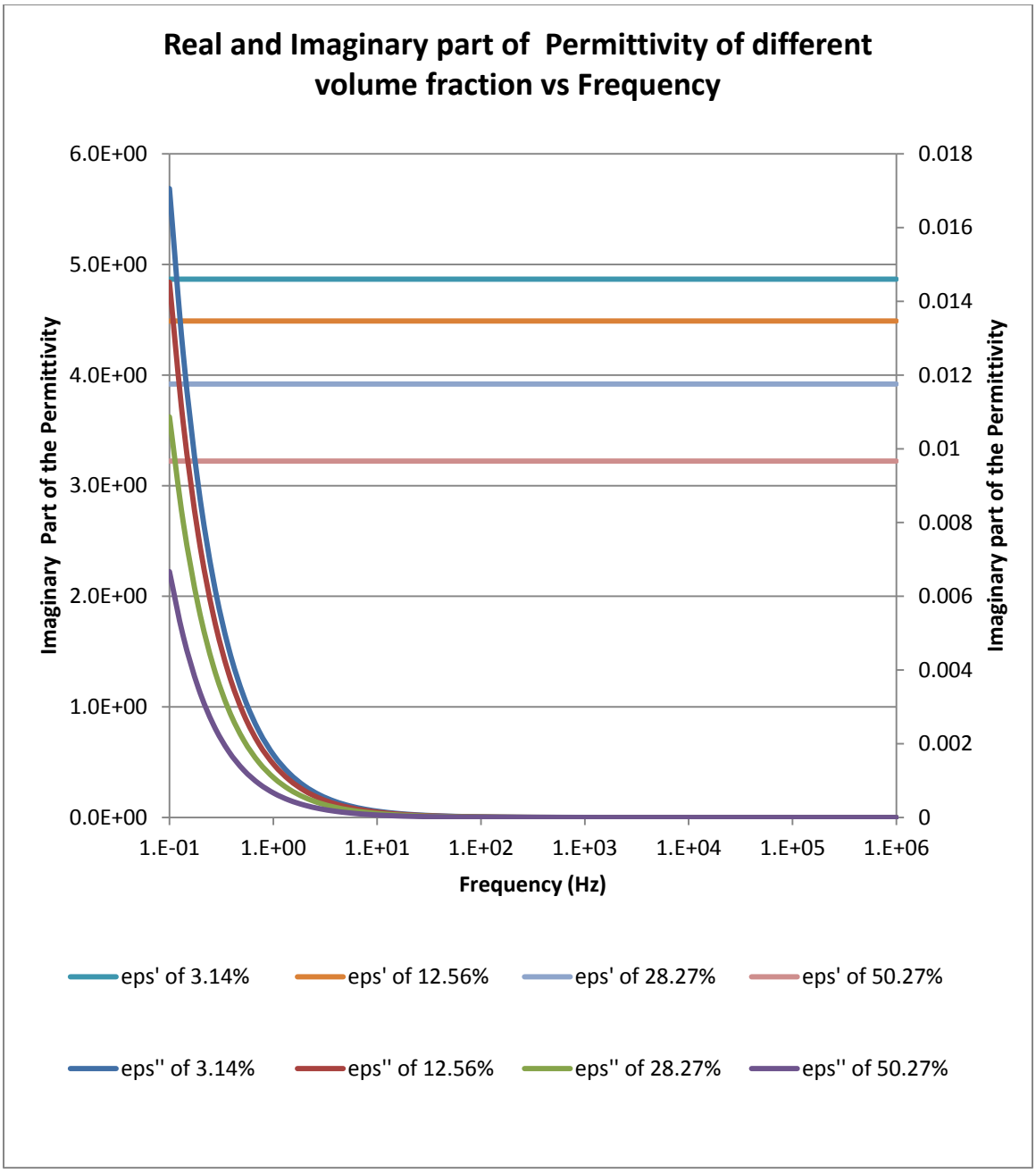

Figure 7.7 Real and Imaginary part of the permittivity with different volume fraction of the inclusion.

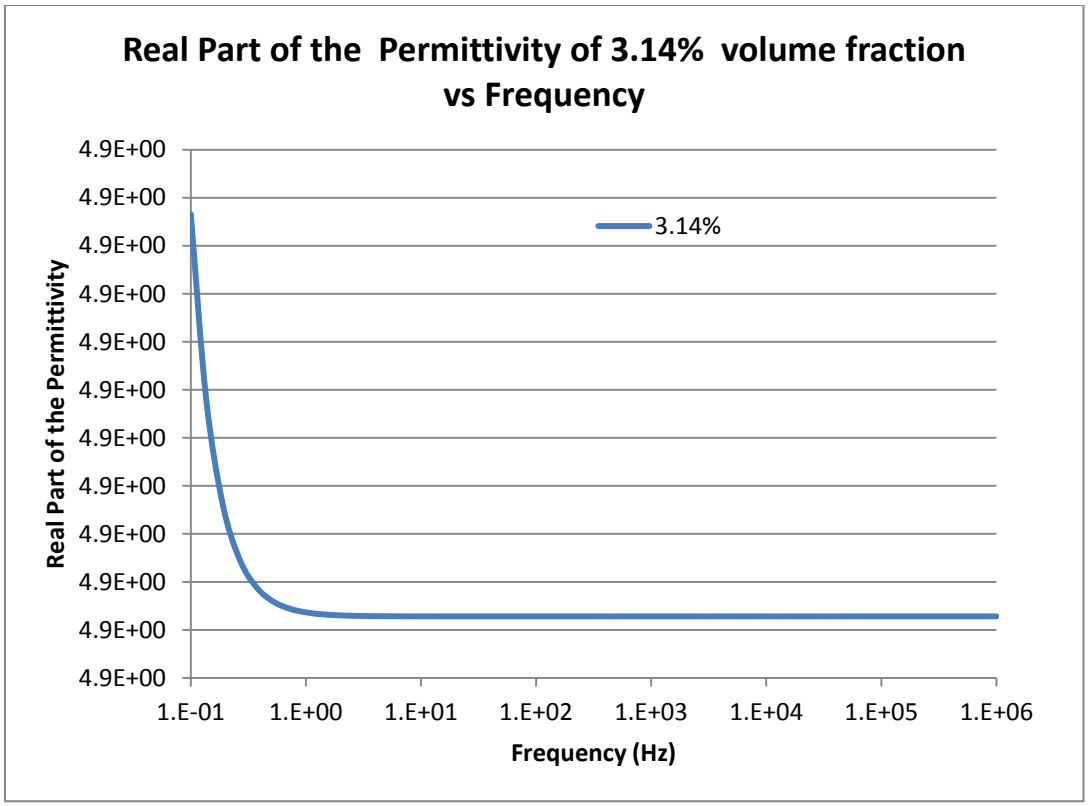

Figure 7.8 Real part of the permittivity of the material with 3.14% volume fraction of inclusion.

For different volume fractions of inclusion, the real part of the permittivity was calculated from the computer simulation for the frequency of 10 Hz. Figure 7.9 is the comparison of real part of the permittivity change with increasing volume fraction of the inclusion. The relation between the real part of the permittivity and volume fraction is almost linear, but when the real part of the permittivity is plotted with surface area fraction (surface area fraction is the ration of inclusion surface to the material surface) of the inclusion there is clear nonlinear relationship observed. For low volume fraction the effect of surface area fraction of the inclusion is more dominate than the volume fraction but in the higher volume fraction it is opposite.

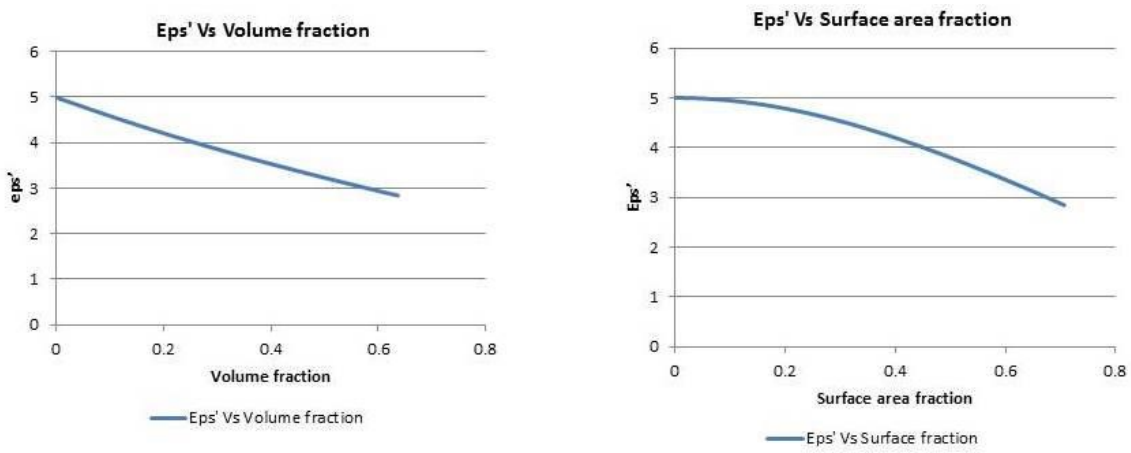

Figure 7.9 Eps' comparison with volume fraction and surface area fraction of the inclusion.

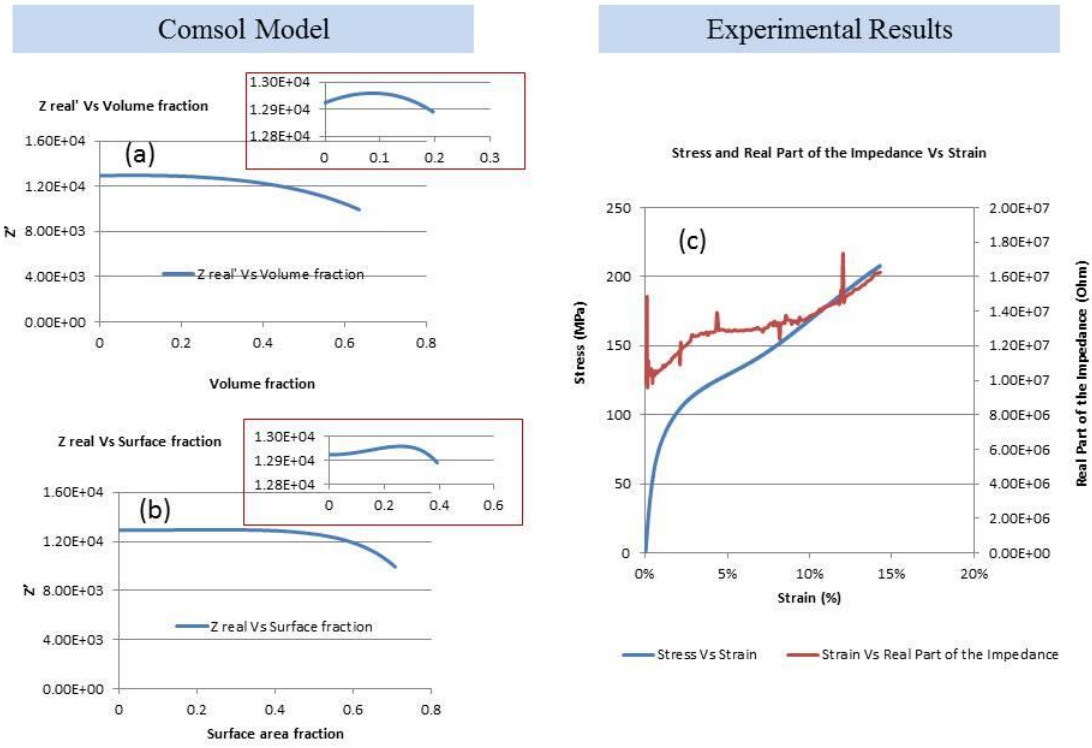

Figure 7.10 Comparison of Comsol™ simulation result and experimental results.

Figure 7.10 illustrates the comparison between computer simulation results with increasing inclusion volume/surface-area fraction and experimental results. 7.10 (a) and

(b) show slight increases in real part of the impedance in low volume/ surface-area fraction. 7.10 (c) shows the experimental results of real part of the impedance change with the strain. The real part of the impedance increases below the low strain (below 5%) for the off axis sample where matrix microcracking is dominant and distributed throughout the material system.

7.2.2 Three Phase Model

Composite materials are filled with filler material to achieve the desire mechanical, thermal and electrical properties. Typical filler materials used for the modeling is carbon or glass fiber. The use of these fibers as filler material introduces a water sensitive component into the polymer composites. Glass fibers are well known for their water affinity on the surface. Currently, epoxies are widely used matrix materials in composite industries which has the potential of being exposed to moist conditions or a humid environments. Soles and Yee [104] found that a network of nanopores that is inherent in the epoxy structure helps water traverses the epoxy and the average size of nanopores diameter to vary from 5 to 6.1 Å and account for 3–7% of the total value of the epoxy material. The approximate diameter of a kinetic water molecule is just 3.0 Å, so via the nanopores network moisture can easily traverse into the epoxy. They also found that the volume fraction of nanopores does not affect the diffusion coefficient of water and argued that polar groups coincident with the nanopores are the rate-limiting factor in the diffusion process, which could explain why the diffusion coefficient is essentially independent of the nanopore content. In the Figure 7.11 they explain how the water transport happens in epoxy networks.

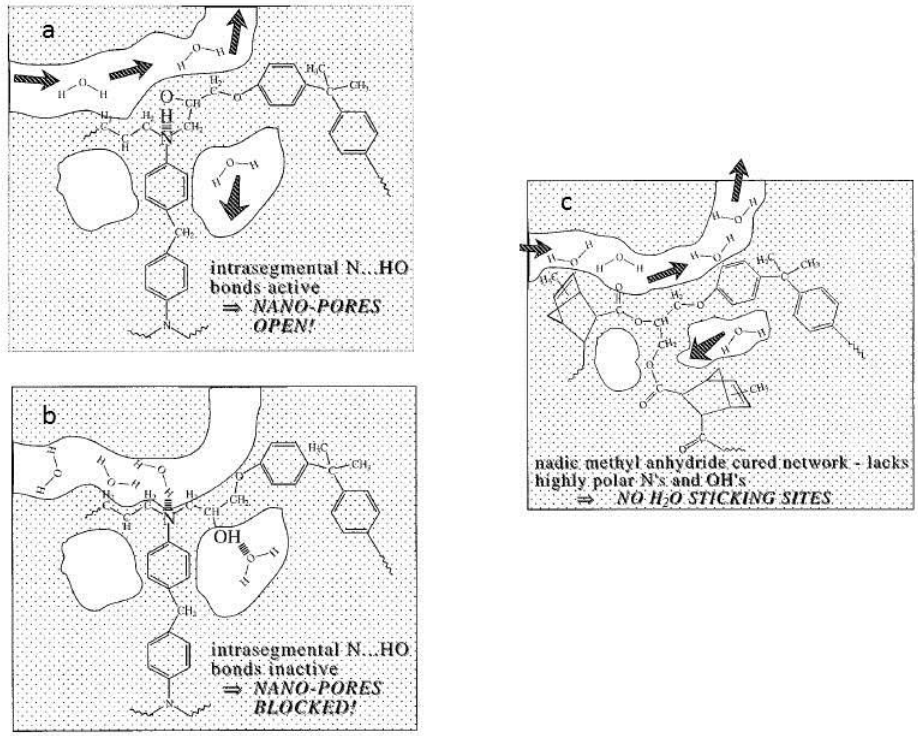

Figure 7.11 A plausible picture of moisture diffusion through the nanopores of an amine-containing epoxy [104]

There are many theories about the state of water molecules in polymers. Adamson [105] suggested that moisture can transfer in epoxy resins in the form of either liquid or vapor. It is proposed by Tencer [106] that it is also possible that vapor water molecules undergo a phase transformation and condense to the liquid phase. This condensed moisture was stated to be either in the form of discrete droplets on the surface or in the form of uniform monolayer [107].

Water has a higher dielectric permittivity and conductivity than the glass fiber and matrix, so it has strong effects on the dielectric properties, i.e. relative permittivity and dielectric loss, of the material system. In literature it is well established that water

absorption increase the dielectric constant of the dielectric material [108-112]. This dielectric loss observed in low frequency range and water diffused through the interface and weakens the interfacial strength of filler and matrix.

When composite materials go through degradation processes, microcracks typically form and these microcracks can be filled with moist air, and condensed or adsorbed water layers can form on the surface of the defects. In our two phase model we saw an interfacial polarization (Maxwell-Wagner-Sillars polarization) that is present in the low frequency region of the frequency spectra. If a water layer is present on the surface of the defect it will become electrically conductive. Since the host material and defect have electrical conductivity and permittivity is not significantly high, this will give rise to interfacial polarization.

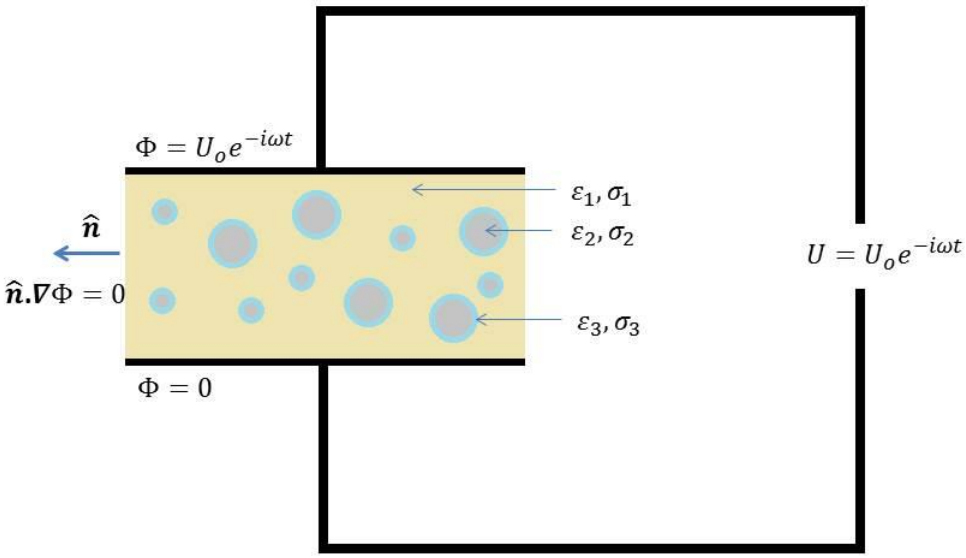

Figure 7.12 Tri-layer model

Above figure, Figure 7.12, illustrates the tri-layer computational model used for the study where yellow, gray and blue part represent respectively the host material, defect and a conductive layer. Permittivity and ohmic conductivity of the host material were taken to be $\varepsilon_1 = 5$ and $\sigma_1 = 10^{-13}$ S/m and for the inclusion permittivity and ohmic conductivity, $\varepsilon_2 = 2$ and $\sigma_2 = 10^{-15}$ S/m. For the conductive layer different permittivity ε_3 and conductivity σ_3 (higher than host and defect properties) was used to see the effect on the effective dielectric properties of the material system.

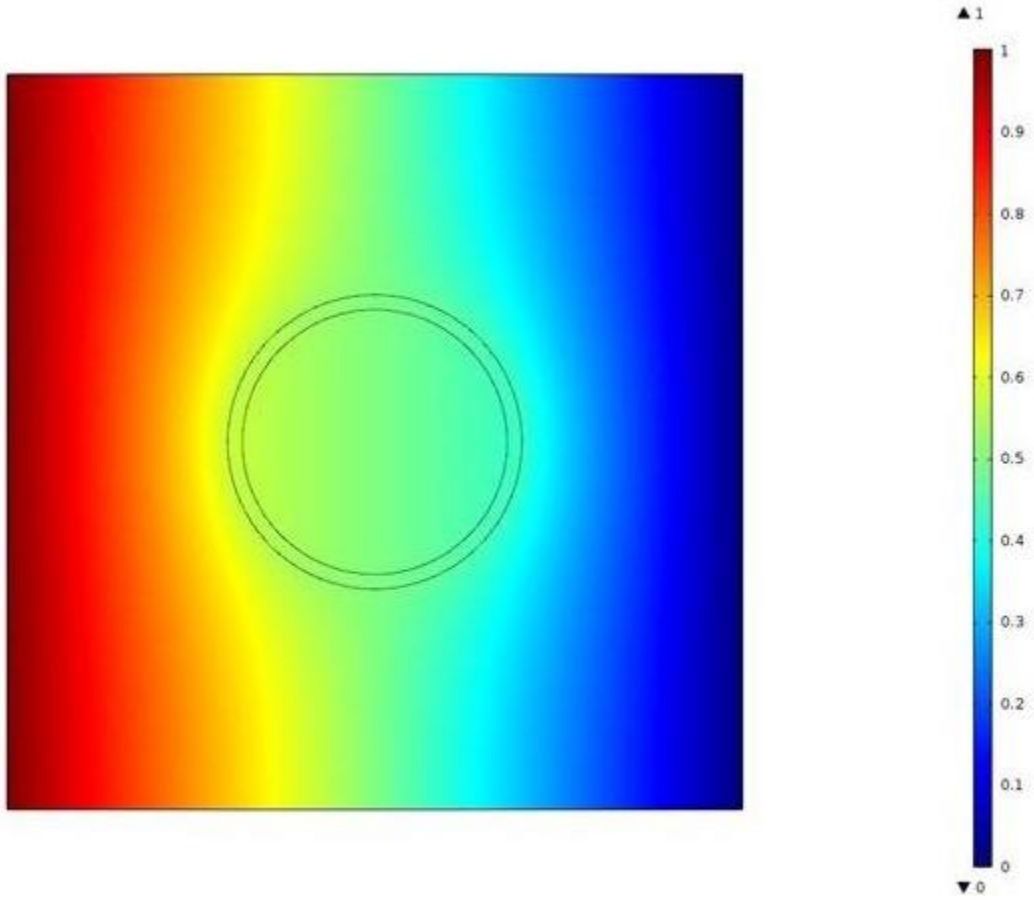

Figure 7.13 Potential distributions around the inclusion with a conductive layer

Above figure, Figure 7.13, shows the potential distributions around the inclusion of the tri-layer model which is different than the potential difference shown in Figure 7.1 for two phase inclusion model. Because of the conductive layer around the inclusion there is a large undulation of the space distribution of the electric potential.

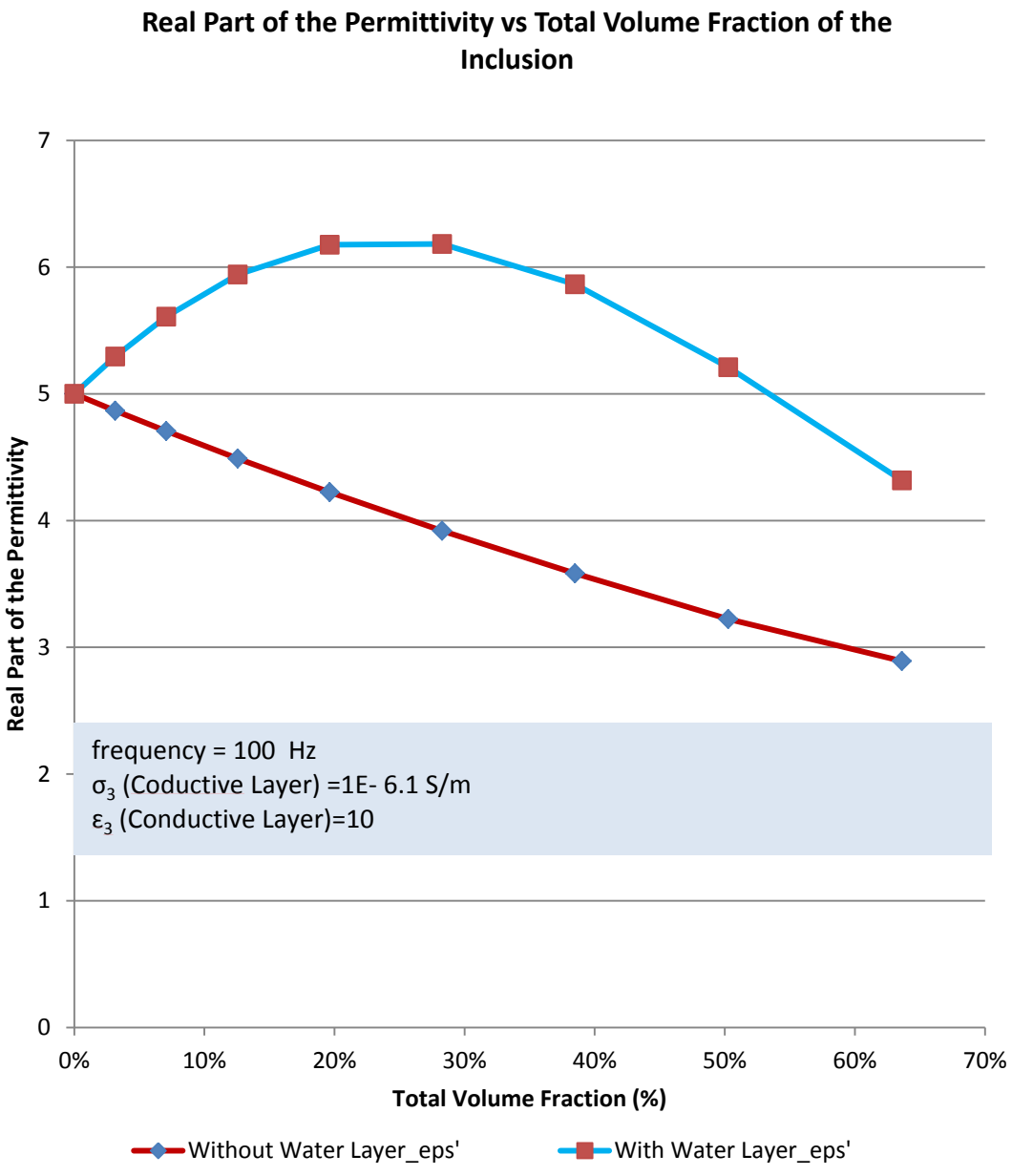

Figure 7.14 Variation of real part of the permittivity with increasing volume fraction

For the tri-layer model, total volume fraction is the sum of the volume fraction of defect and the volume fraction of the conductive layer. For all the cases of tri-layer modelling conductive layer thickness was kept 0.5 micro meter. We saw that for two phase model real part of the permittivity was almost linear but in Figure 7.14 we can see that there is a increase in real part of the permittivity for lower volume fraction and then a decreasing trend. As there is a conductive layer in between the defect and the host matrix interfacial polarization plays a vital role for this type of behavior. Decrease of the real part of the permittivity for higher volume fraction is because of the dominance of the volume of the defect is higher than the interfacial polarization contributing by the conductive layer.

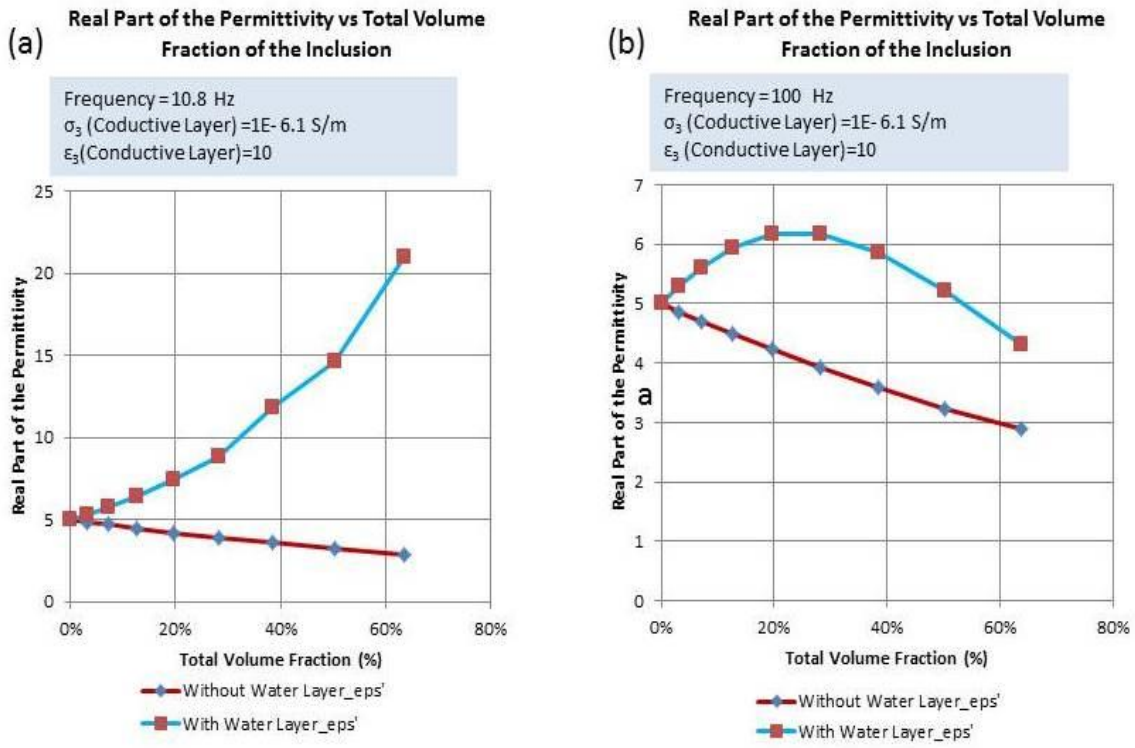

Figure 7.15 Frequency dependency of the real part of permittivity for different volume fraction

This is clear from Figure 7.15 that for same conductivity and permittivity of the conductive layer for low frequency, real part of the permittivity of the material system is higher than higher frequency.

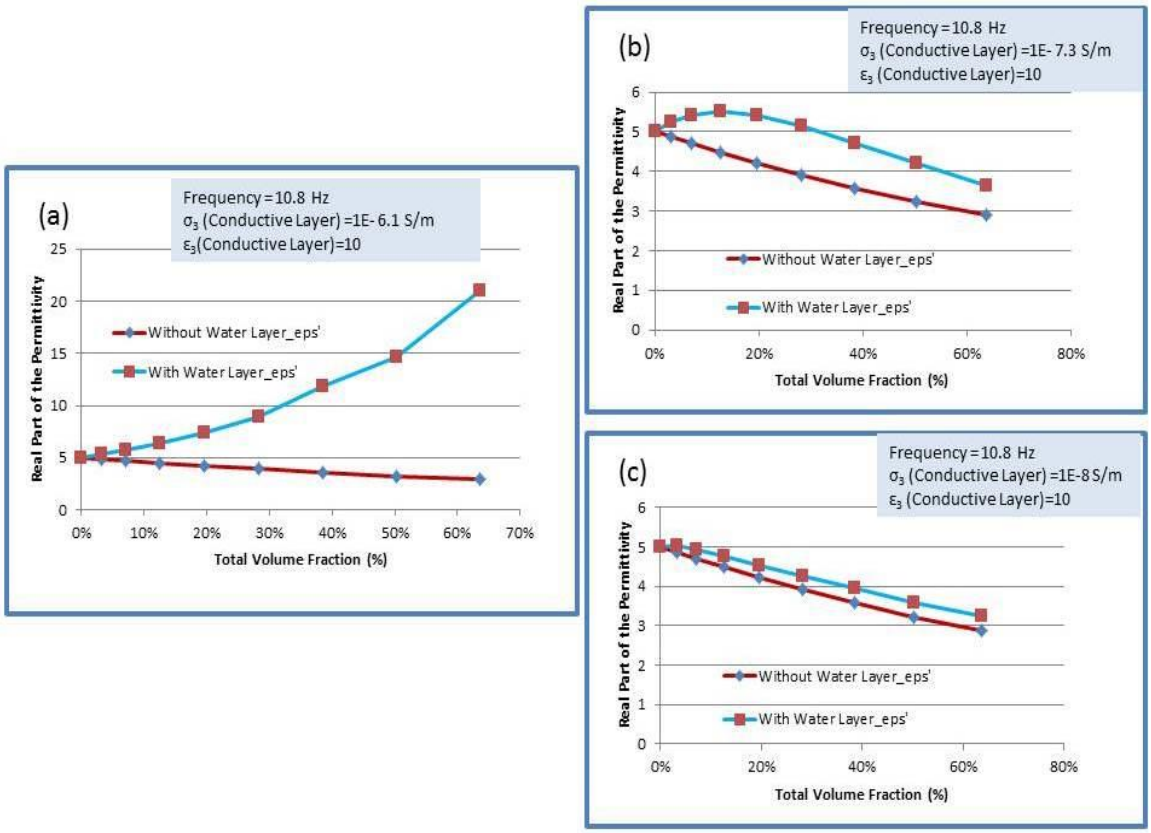

Figure 7.16 Dielectric properties dependence on the conductivity

Figure 7.16 shows the dependence of dielectric constant on the conductivity of the conductive layer. Real part of the permittivity at different volume fraction for same permittivity and frequency behave differently.

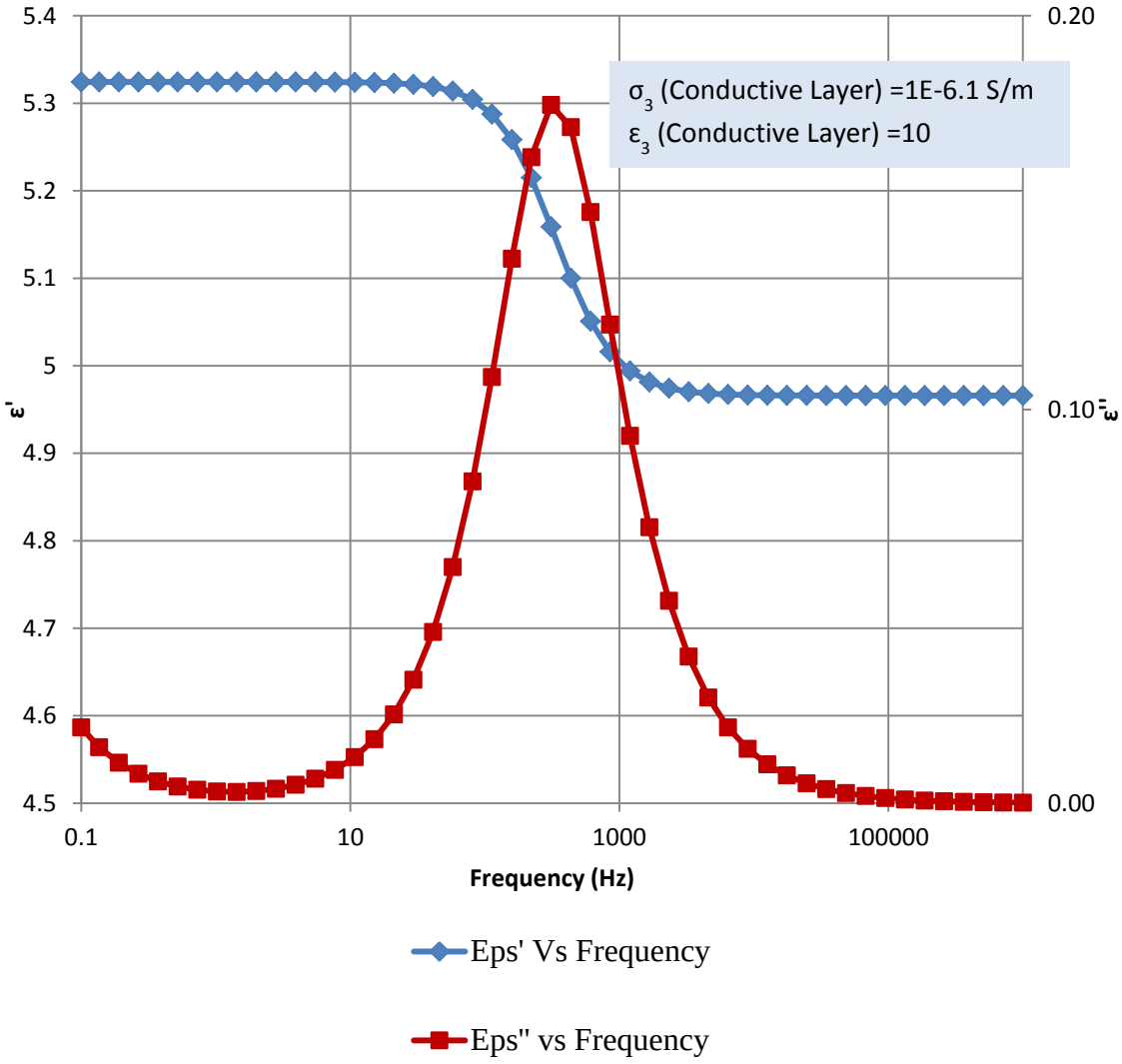

Figure 7.17 Real and Imaginary Part of the Permittivity Vs Frequency for 3.14 % total volume fraction of the inclusion

For same volume fraction of the inclusion there is a step like increase of the real part of the permittivity and dielectric loss also has the peak in that part, this is where the Maxell-Wagner-Sillars polarization happen.

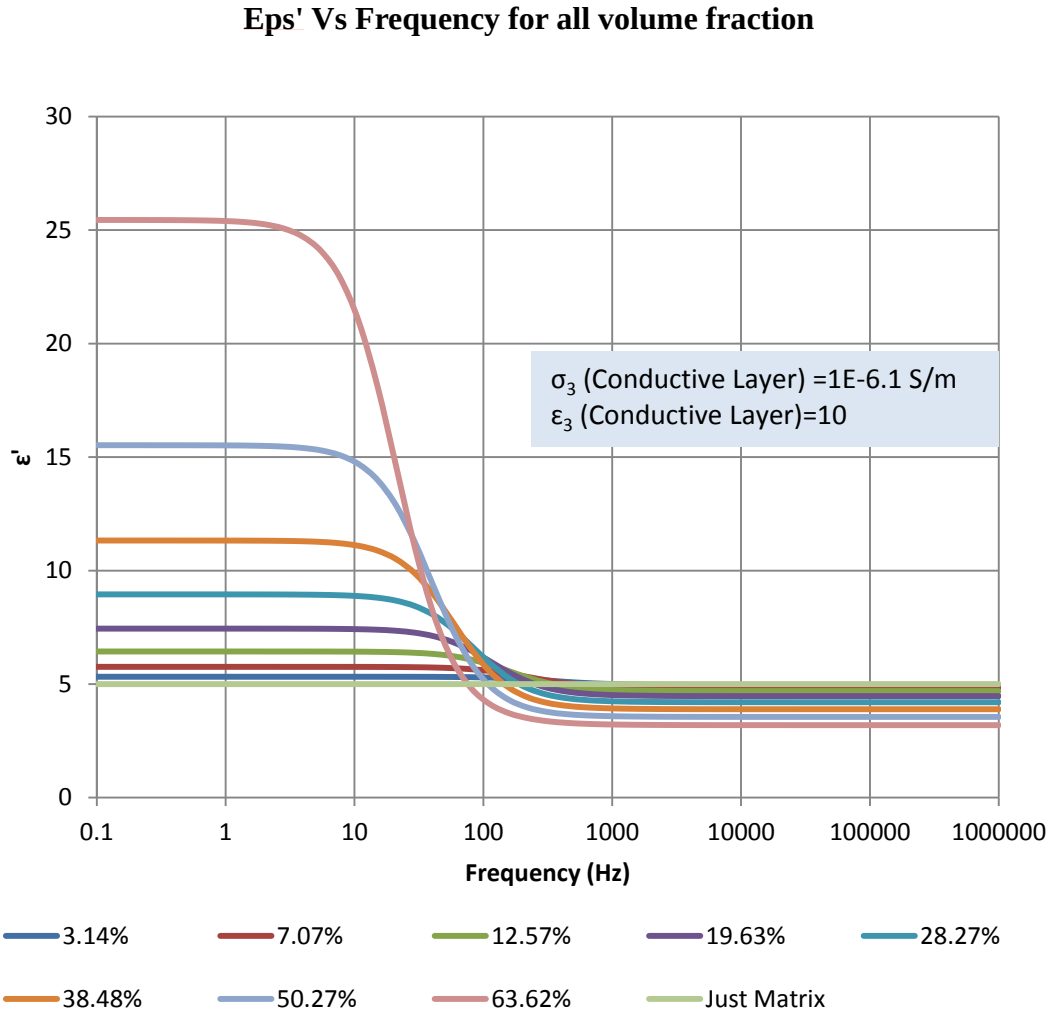

Figure 7.18 Real part of the permittivity in frequency spectra of all volume fractions

Figure 7.18 shows the relation of real part of the permittivity with the frequency for all volume fractions of the inclusion. Simulation was also done for the just matrix (this is host material, as we consider it homogeneous) material, as there is no other phase there was no chance of for charge to accumulate so there is no change of the dielectric constant for matrix. We can see for higher volume fraction dielectric relaxation strength (difference between the real parts of the permittivity at low frequency and high

frequency) also increase. At higher frequency real part of the permittivity drops for volume fraction because charge accumulation doesn't happen at the interface.

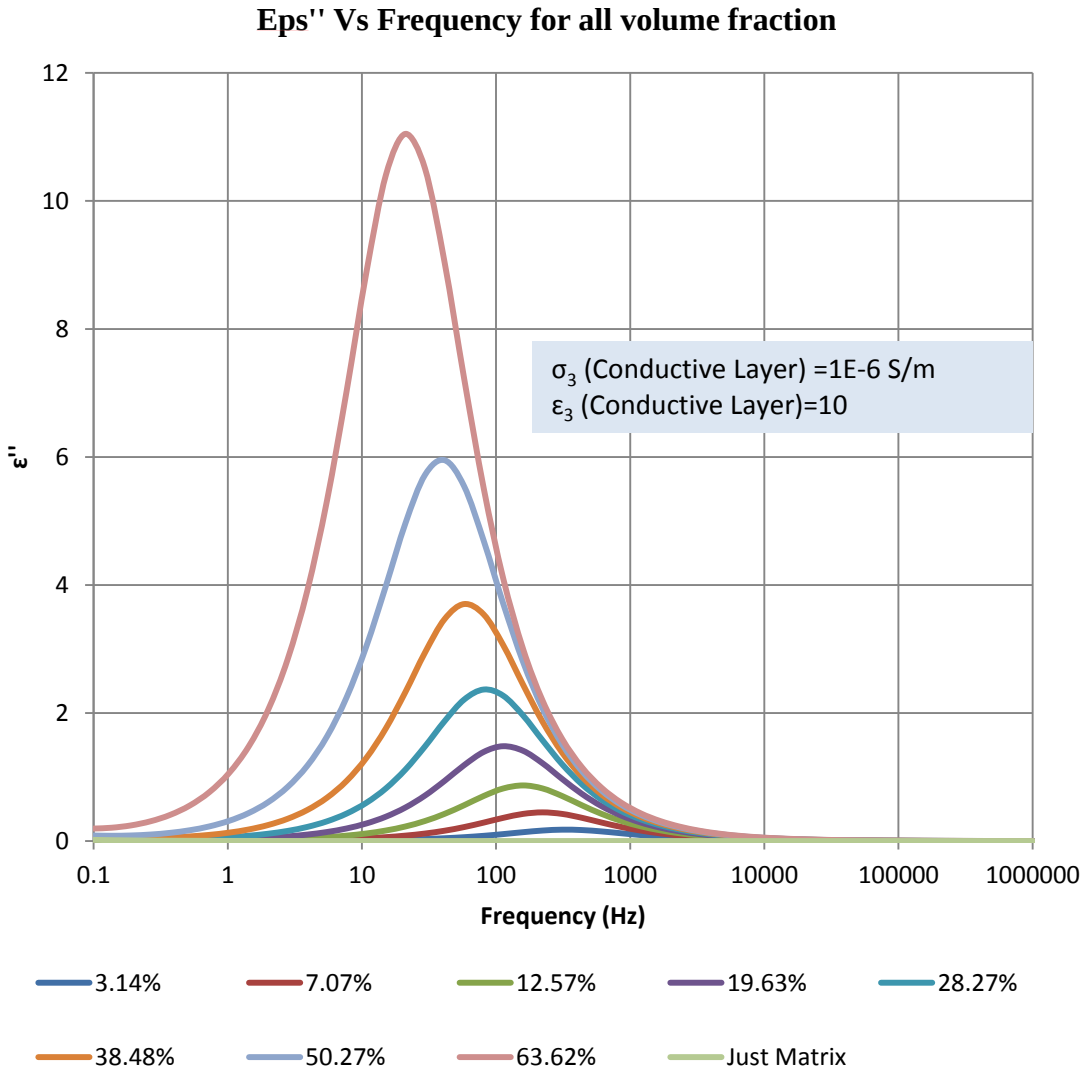

Figure 7.19 Imaginary part of the permittivity in frequency spectra of all volume fractions

Dielectric loss (imaginary part of the permittivity) also varies with volume fraction and it illustrates in Figure 7.19. For high volume fraction dielectric loss shifted and the peak of the loss also increase.

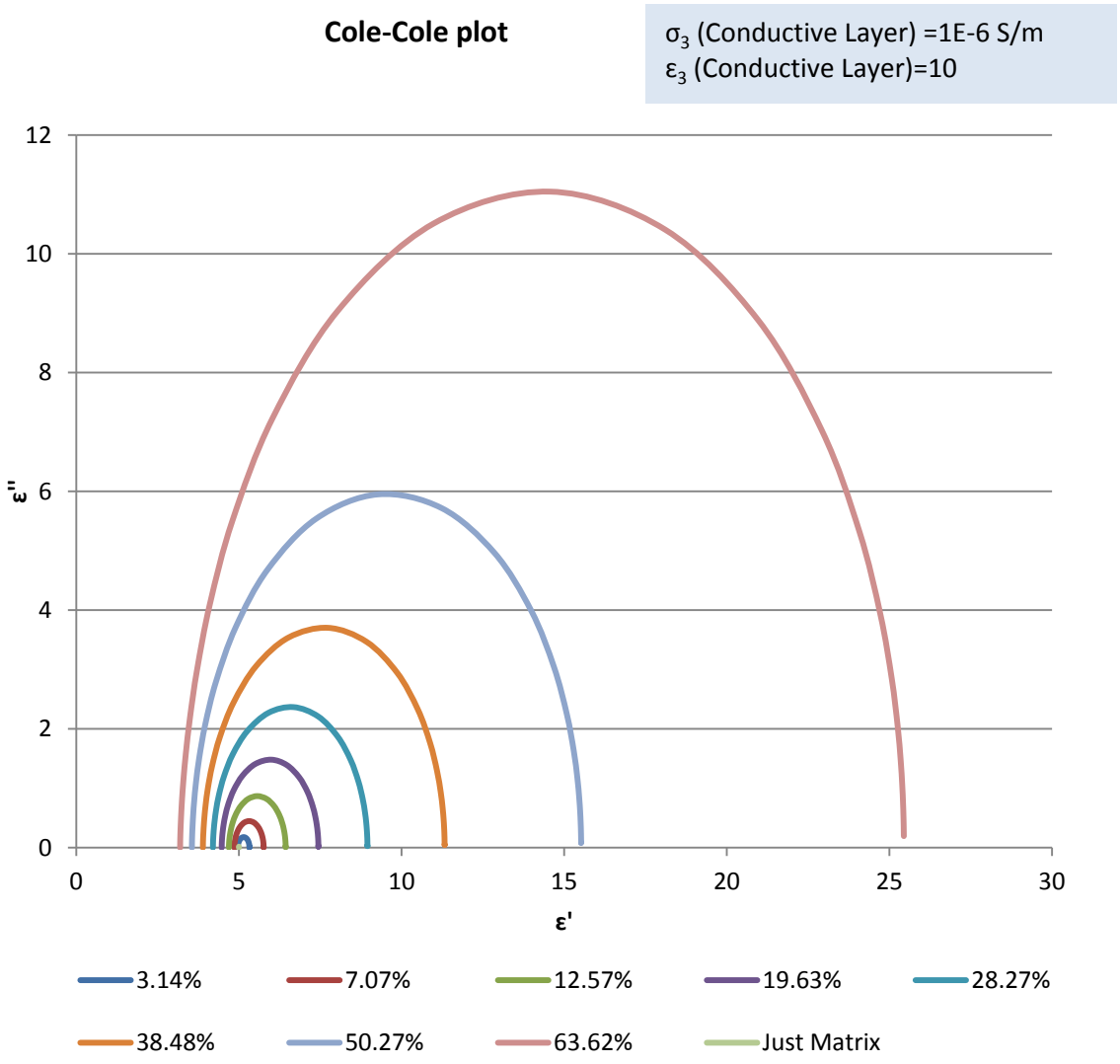

Figure 7.20 Cole-Cole plot of different volume fraction

Cole-Cole plot, Figure 7.20, also shows the shift in relaxation for different volume fraction.

7.2.3 Distributed Damage

A distributed damage model was created to see the effect of the distribution of the damage. Dielectric study was performed a certain volume fraction of inclusion and that inclusion was divided in 10 inclusion but keeping the volume fraction same.

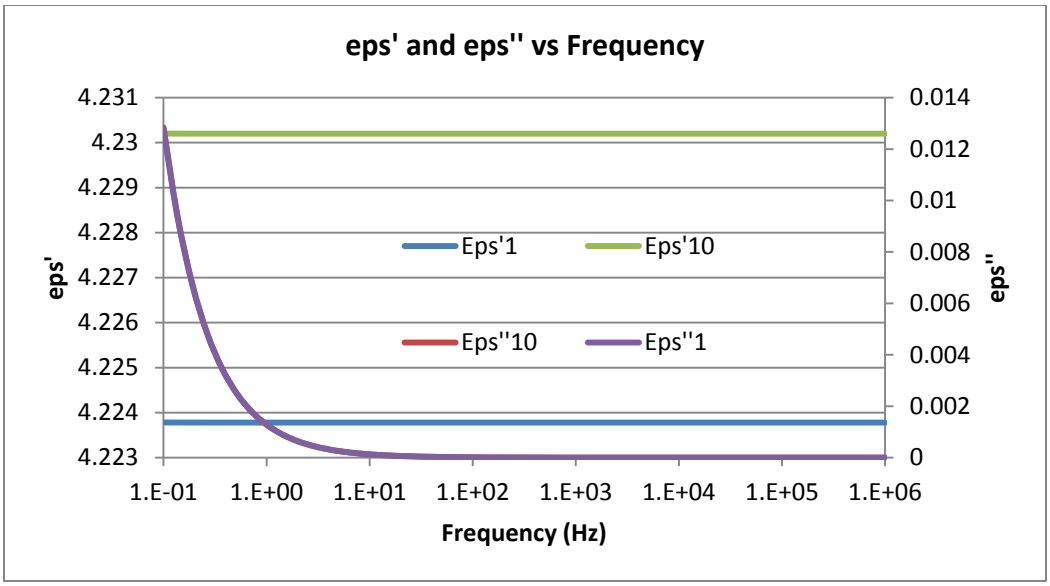

Figure 7.21 Dielectric Properties without conductive layer for same volume fraction but different number of inclusion

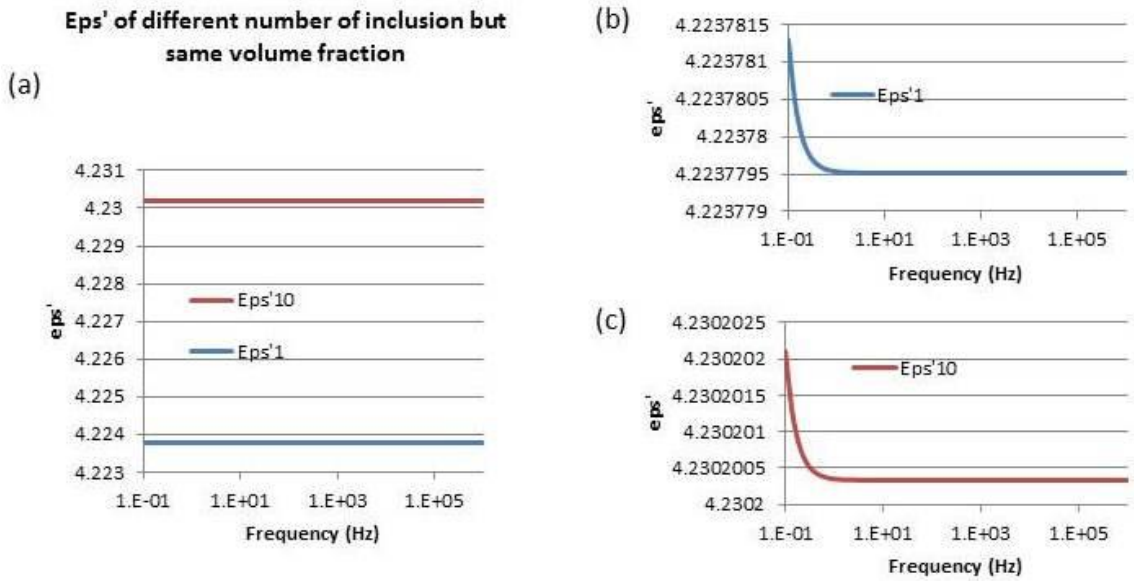

Figure 7.22 Real Part of the permittivity for different number of inclusion but same volume fraction

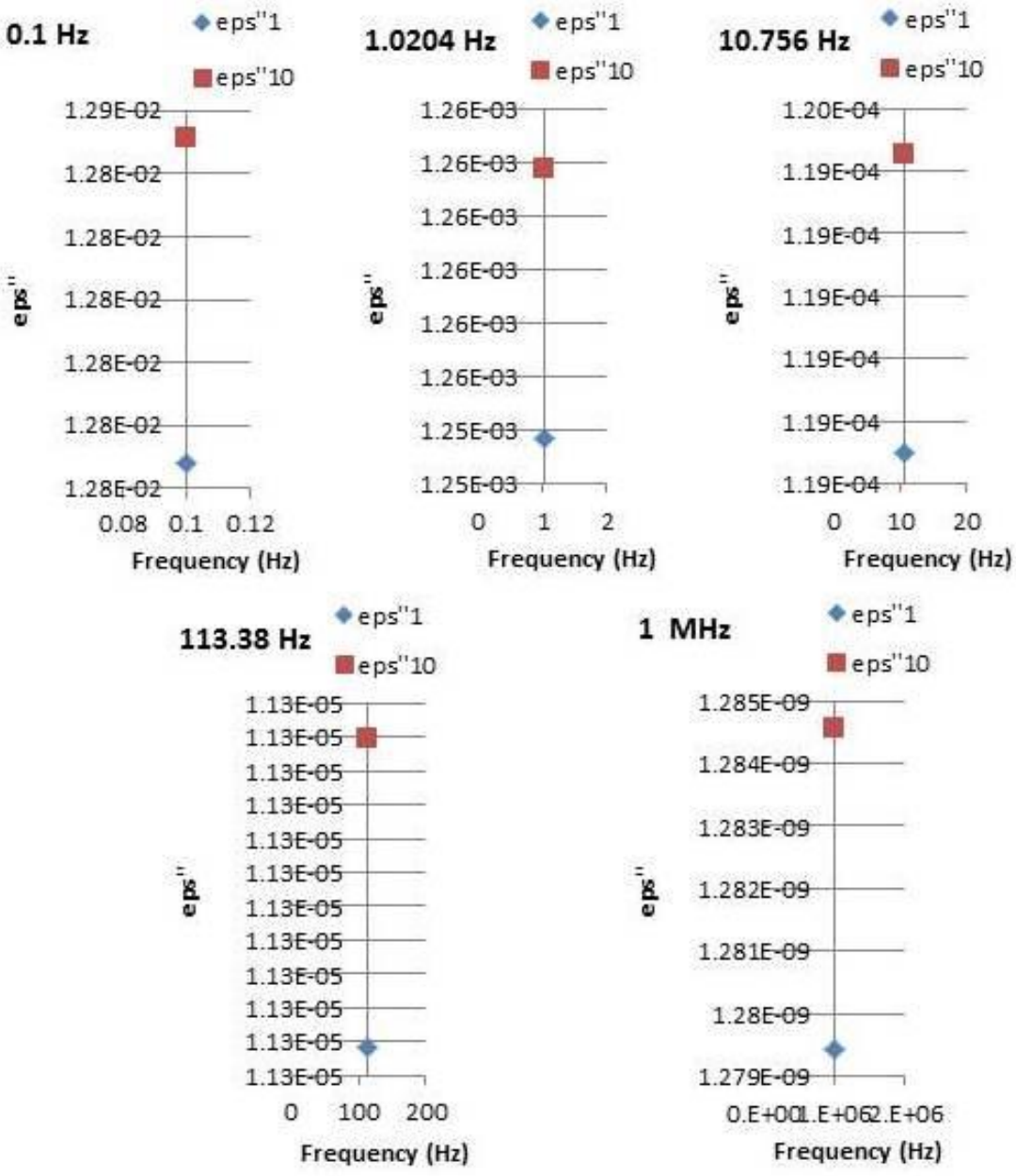

Figure 7.23 Dielectric losses at different frequency for different number of inclusion but same volume fraction without any conductive layer.

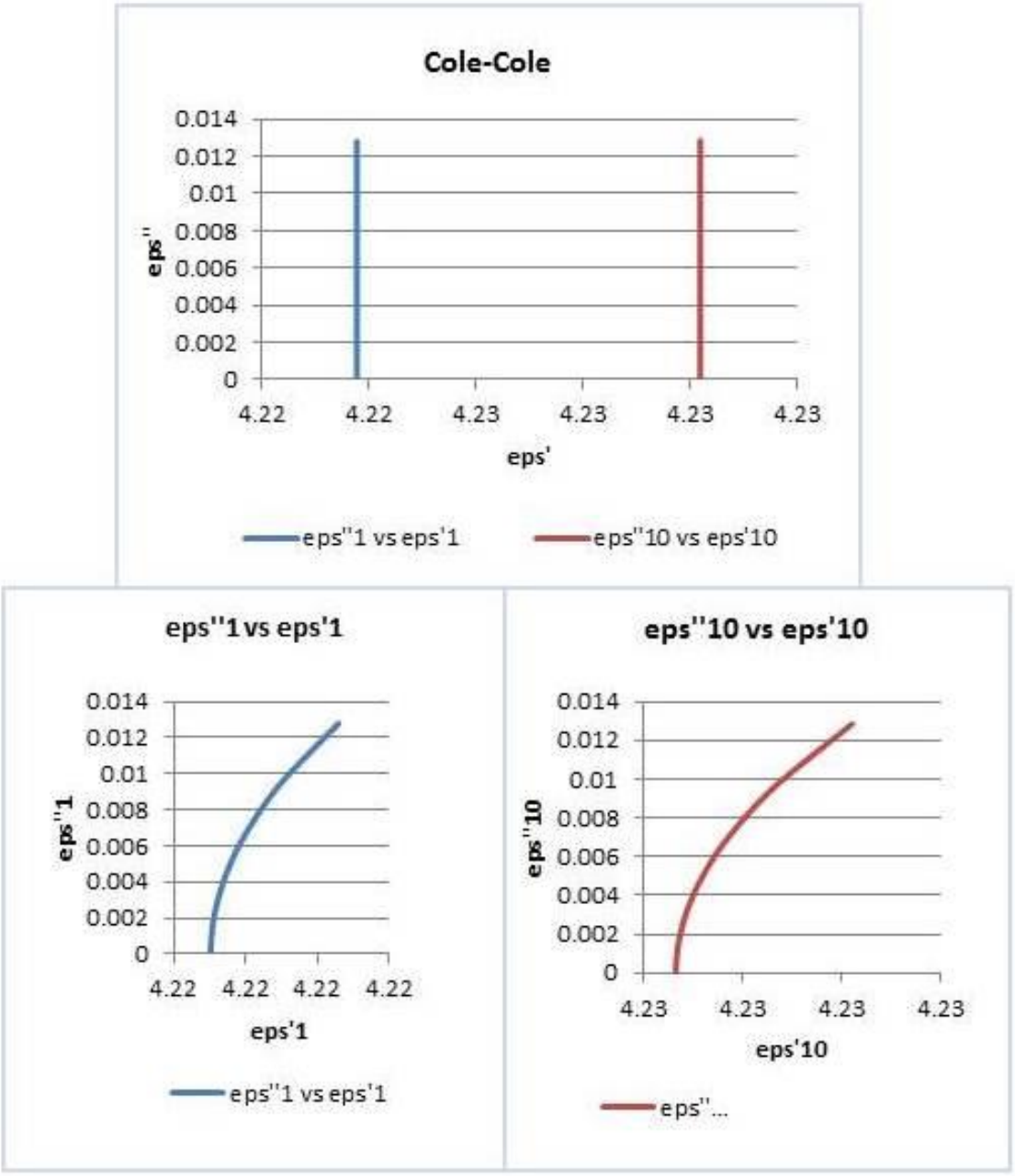

Figure 7.24 Cole-Cole plot of different number of inclusion without conductive layer

From Figure 21-24 show the change of dielectric properties of a single damage and distributed damage with same amount of volume fraction without any conductive layer around defect. Dielectric loss increased for the distributed damage because of more interfacial polarization.

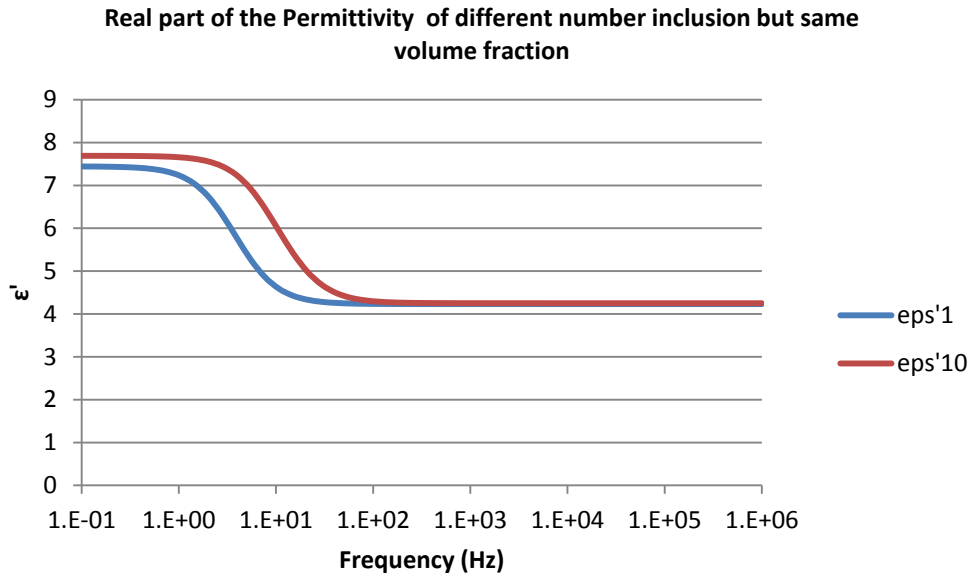

Figure 7.25 Real part of the Permittivity of different number inclusion but same volume fraction with conductive layer

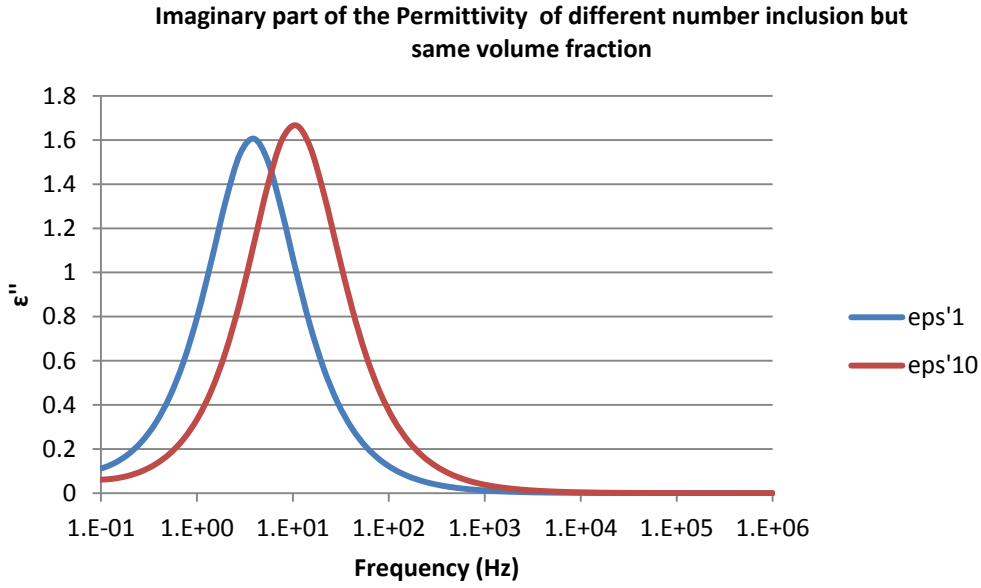

Figure 7.26 Imaginary part of the Permittivity of different number inclusion but same volume fraction with conductive layer

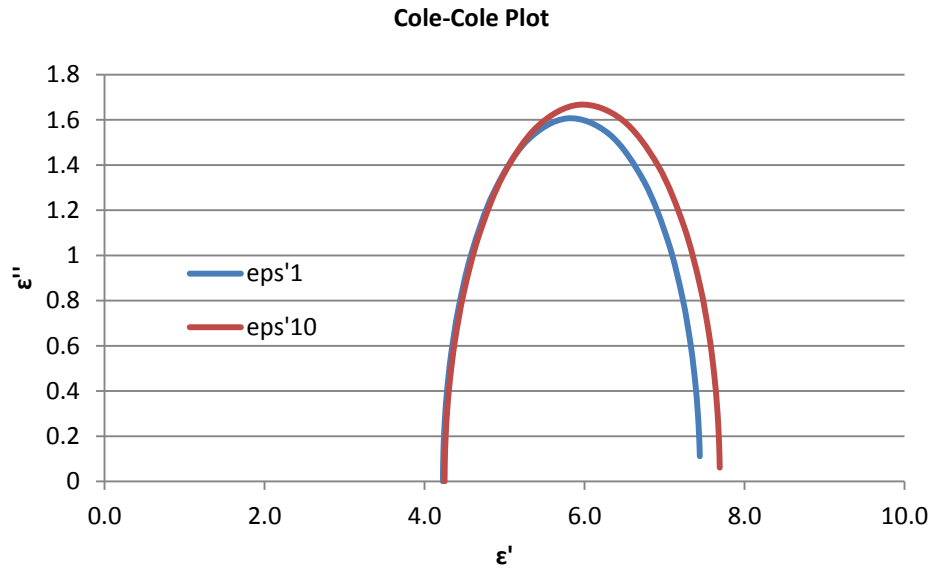

Figure 7.27 Cole-Cole plot of different number of inclusion with conductive layer

From Figure 25-27 show the change of dielectric properties of a single damage and distributed damage with same amount of volume fraction with a conductive layer around the defect. Dielectric loss increased for the distributed damage because of more interfacial polarization and it is more evident because of the conductive layer around the defect leads to interfacial polarization.

CHAPTER 8 CONCLUSION

In this research work we utilized Broadband Dielectric Spectroscopy (BbDS) of different heterogeneous material systems to understand the relationship between the internal microstructural mechanisms in the material and the dielectric properties.

We studied SOFC composite materials without the presence of any electrochemistry to understand the damage state during thermal loading and also how the local features significantly influence the performance of the SOFC. Consequently, in this study, we explored i) how different morphology of electrodes in an SOFC changes BbDS characteristics at different temperatures ii) how can we predict such response utilizing the local morphology iii) and how actual material state changes may be visualized and characterized non-destructively to study degradation mechanisms. The present work demonstrated that broadband dielectric spectroscopy techniques can be used to extract direct material level information that forms the elementary foundation for designing the morphology of electrode materials and subsequent durability analysis.

The major objectives of the research were to understand the changes of dielectric properties of composite materials during progressive degradation and failure induced by applied mechanical loading. To enable this research, we have introduced a newly developed in-situ, in-operando dielectric measurement method to measure dielectric property changes with increasing micro-crack density and other damage induced by mechanical loading. It is determined that the size, shape and orientation of microdamage as well as the dielectric character of the defect volume and the interfaces created are all

individually distinguished by the method. Observed changes were not monotonic with loading history, and were specific to the dominant damage mode as a function of load level.

In our ex-situ study of fiber reinforced composite materials we showed that the damage state can be detected and characterized by BbDS, and we introduced a dielectric parameter, Dielectric Relaxation Strength (DRS), to correlate the damage state of the materials system caused by uniaxial quasi-static tensile loading to the strength of individual specimens. We also showed how the environment affects the dielectric properties of the damaged composite materials.

To assist in the interpretation and understanding of our results, we introduced a proper conformal computational model and established some agreements between the results of this model with our experimental observations. For example, we showed how the dielectric properties (i.e., conductivity, permittivity) and distribution of the inclusions inside materials affects the interfacial polarizations and how the global dielectric relaxation related to this polarization mechanism shifted with increasing volume fraction of the inclusions.

In general, the dielectric properties of heterogeneous systems are influenced by various physical factors: electrical and structural interactions between particles, heterogeneity of morphological and electrical properties of the constituent phases, frequency dependence of electrical phase parameters, intra-particle structure, particle shape, size, orientation and morphology. This dependence complicates the determination of the electrical parameters of heterogeneous materials from the observed dielectric relaxation spectra, but also presents us with an opportunity to recover important

information not only about the electrical and structural properties of constituents but also about the interactions between constituents, including parent material and damage phases.

From the results presented it can be concluded that the analysis of the dielectric data gives us information about the type of material state change throughout the mechanical life of the composite material. It should be emphasized that these changes in the dielectric properties are distinct and measurable changes in material state, and that they are caused by a non-conservative, non-equilibrium material response to the applied fields.

Dielectric data also can be used to predict mechanical properties such as strength, life, and durability, and these dielectric characteristics can be predicted by multiphysics analysis as a foundation for interpretation of their changes in terms of micro-damage, and as a basis for design for durability. As such, the work provides a new foundation for assessing the durability and prognosis of future performance of heterogeneous material systems in general, and structural composite materials in particular, i.e., it shows promise as a tool for knowledge based design for durability of composite material systems.

8.1 Further Research recommendation

A realistic conformal computer simulation can be done by acquiring 3D information by X-ray tomography of the real structural composites and rendering that data cloud as a foundation for multiphysics analysis. Such an analysis should consider not only the fibers and matrix of the host material in the finite element simulation, but also must consider the interphase properties.

A more thorough study of the effect of anisotropy on resulting properties should also be pursued. For example, the present results can likely be generalized to many principle fiber orientations by constructing a master curve for the dielectric properties of the composite material by using information from measurements of predictions of the dielectric properties of composite plies of different directions.

Finally, further investigation should be made of dielectric properties as a foundation for prediction of composite strength and life. Success of this effort would provide a much needed replacement in composite materials for the present lack of a degradation parameter (like crack length in homogeneous materials) that can be directly related to strength and life as a predictive observable. This could be a foundation for the "current state analysis" that is vigorously sought by vehicle and aircraft manufacturers.

REFERENCES

[1]. Qian, H., Kucernak, A. R., Greenhalgh, E. S., Bismarck, A., & Shaffer, M. S. (2013). Multifunctional structural supercapacitor composites based on carbon aerogel modified high performance carbon fiber fabric. *ACS applied materials & interfaces*, 5(13), 6113-6122.

[2]. Volvo develops body panels that serve as batteries (2013, October 17). Retrieved from http://www.carbodydesign.com.

[3]. Reifsnider, K. L.; Ed. *Damage in Composite Materials*. ASTM 775, American Society for Testing and Materials, Philadelphia 1982

[4]. Reifsnider, K.L., and Case, S. W. (2002), *Damage Tolerance and Durability of Material Systems*. New York: John Wiley and Sons.

[5]. Highsmith, A. L., & Reifsnider, K. L. (1982). Stiffness-reduction mechanisms in composite laminates. *Damage in composite materials, ASTM STP*, *775*, 103-117.

[6]. Nairn, J. A. (2000). Matrix microcracking in composites. *Polymer matrix composites*, *2*, 403-432.

[7]. Talreja, R. (1985). Transverse cracking and stiffness reduction in composite laminates. *Journal of composite materials*, *19*(4), 355-375.

[8]. Talreja, R., & Singh, C. V. (2012). *Damage and failure of composite materials*. Cambridge University Press.

[9]. Varna, J., & Krasnikovs, A. (1998). Transverse cracks in cross-ply laminates 2. Stiffness degradation. *Mechanics of composite materials*, *34*(2), 153-170.

[10]. O'brien, T. K. (1982). Characterization of delamination onset and growth in a composite laminate. *Damage in composite materials, ASTM STP, 775*(2), 140-167.

[11]. Stinchcomb, W. W., & Bakis, C. E. (1990). Fatigue behavior of composite laminates. *Fatigue of composite materials*, *4*, 105-180.

[12]. Subramanian, S., Reifsnider, K. L., & Stinchcomb, W. W. (1995). Tensile strength of unidirectional composites: the role of efficiency and strength of fiber-matrix interface. *Journal of composites technology & research*, *17*(4), 289-300.

[13]. Razvan, A., & Reifsnider, K. L. (1991). Fiber fracture and strength degradation in unidirectional graphite/epoxy composite materials. *Theoretical and applied fracture mechanics*, *16*(1), 81-89.

[14]. Gao, F., Boniface, L., Ogin, S. L., Smith, P. A., & Greaves, R. P. (1999). Damage accumulation in woven-fabric CFRP laminates under tensile loading: Part 1. Observations of damage accumulation. *Composites science and technology*, *59*(1), 123-136.

[15]. Holmes, J. W., & Cho, C. (1992). Experimental Observations of Frictional Heating in Fiber-Reinforced Ceramics. *Journal of the American Ceramic Society*, *75*(4), 929-938.

[16]. Christensen, R. M. (2012). *Mechanics of composite materials*. Courier Dover Publications.

[17]. Dillard, D. A. (1991). Viscoelastic behavior of laminated composite materials. *Fatigue of composite materials*, *4*, 339-384.

[18]. Gates, T. S. (1991). Rate Dependent Stress-Strain Behavior of Advanced Polymer Matrix Com- posites. *NASA TM 104070, NASA Langley Research Center.*

[19]. Wang, Z., Xia, Y., & Yang, B. (1996). A statistical model and experimental study of the strain rate and temperature dependence of the strength of fibers.*Applied composite materials*, *3*(2), 89-101.

[20]. Nevill, G. E., Ross, C. A., & Jones, E. R. (1971). Dynamic compressive strength and failure of steel reinforced epoxy composites. *Journal of Composite Materials*, *5*(3), 362-377.

[21]. Lataillade J.L., Delaet M., Collombet F. (1993) Damage testing of cross-ply laminates under high strain rate effect of intralaminar shear stress. *Proceeding of 9th ICCM, V. 358-365,* Madrid Spain.

[22]. Staab G.H., and Gilat A. (1993) High strain rate characterization of angle ply glass/epoxy laminates. *Proceeding of 9th ICCM, V. 278-285*, Madrid Spain.

[23]. Wang, Z. (1995). Experimental evaluation of the strength distribution of E-glass fibres at high strain rates. *Applied Composite Materials*, *2*(4), 257-264.

[24]. Groves, S. E., Sanchez, R. J., Lyon, R. E., & Brown, A. E. (1993). High strain rate effects for composite materials. *Composite Materials: Testing and Design*,*11*, 162-176.

[25]. Hufner, D. (2008). Progressive Failure of Woven Polyer-Based Composites under DynamicLoading: Theory and Analytical Simulation. *University of Connecticut,* PhD Dissertation.

[26]. Talreja, R. (1981). Fatigue of composite materials: damage mechanisms and fatigue-life diagrams. *Proceedings of the Royal Society of London. A. Mathematical and Physical Sciences*, *378*(1775), 461-475.

[27]. Prasse, T., Michel, F., Mook, G., Schulte, K., & Bauhofer, W. (2001). A comparative investigation of electrical resistance and acoustic emission during cyclic loading of CFRP laminates. *Composites science and technology*, *61*(6), 831-835.

[28]. Degala, S., Rizzo, P., Ramanathan, K., & Harries, K. A. (2009). Acoustic emission monitoring of CFRP reinforced concrete slabs. *Construction and Building Materials*, *23*(5), 2016-2026.

[29]. Takeda, N., Okabe, Y., Kuwahara, J., Kojima, S., & Ogisu, T. (2005). Development of smart composite structures with small-diameter fiber Bragg grating sensors for damage detection: Quantitative evaluation of delamination length in CFRP laminates using Lamb wave sensing. *Composites science and technology*, *65*(15), 2575-2587.

[30]. Fuwa, M., Bunsell, A. R., & Harris, B. (1976). An evaluation of acoustic emission techniques applied to carbon-fibre composites. *Journal of Physics D: Applied Physics*, *9*(2), 353.

[31]. Kim, S. T., & Lee, Y. T. (1997). Characteristics of damage and fracture process of carbon fiber reinforced plastic under loading-unloading test by using AE method. *Materials Science and Engineering: A*, *234*, 322-326.

[32]. Ceysson, O., Salvia, M., & Vincent, L. (1996). Damage mechanisms characterisation of carbon fibre/epoxy composite laminates by both electrical

resistance measurements and acoustic emission analysis. *Scripta Materialia,34*(8), 1273-1280.

[33]. Yang, B., Huang, Y., & Cheng, L. (2013). Defect detection and evaluation of ultrasonic infrared thermography for aerospace CFRP composites. *Infrared Physics & Technology*, *60*, 166-173

[34]. Mizutani, Y. O. S. H. I. H. I. R. O., Nagashima, K., Takemoto, M., & Ono, K. (2000). Fracture mechanism characterization of cross-ply carbon-fiber composites using acoustic emission analysis. *NDT & E International*, *33*(2), 101-110.

[35]. Prosser, W. H., Jackson, K. E., Kellas, S., Smith, B. T., McKeon, J., & Friedman, A. (1995). Advanced waveform-based acoustic emission detection of matrix cracking in composites. *Materials evaluation*, *53*(9), 1052-1058.

[36]. Rippert, L., Wevers, M., & Van Huffel, S. (2000). Optical and acoustic damage detection in laminated CFRP composite materials. Composites science and technology, 60(14), 2713-2724.

[37]. Maslov, K., Kim, R. Y., Kinra, V. K., & Pagano, N. J. (2000). A new technique for the ultrasonic detection of internal transverse cracks in carbon-fibre/bismaleimide composite laminates. *Composites science and technology*,*60*(12), 2185-2190.

[38]. Kaczmarek, H. (1995). Ultrasonic detection of damage in CFRPs. *Journal of composite materials*, *29*(1), 59-95.

[39]. Aymerich, F., & Meili, S. (2000). Ultrasonic evaluation of matrix damage in impacted composite laminates. *Composites Part B: Engineering*, *31*(1), 1-6.

[40]. Steiner, K. V., Eduljee, R. F., Huang, X., & Gillespie Jr, J. W. (1995). Ultrasonic NDE techniques for the evaluation of matrix cracking in composite laminates. *Composites science and technology, 53*(2), 193-198.

[41]. Fowler, T., Kinra, V. K., Maslov, K., & Moon, T. J. (1892). Research Report: Inspecting FRP Composite Structures with Nondestructive Testing. *Work*, 1.

[42]. Cuc, A., Giurgiutiu, V., Joshi, S., & Tidwell, Z. (2007). Structural health monitoring with piezoelectric wafer active sensors for space applications. *AIAA journal*, *45*(12), 2838-2850.

[43]. Todoroki A., Kobayashi H, Lee J.G.(1994). Impact analysis of delamination cracks in carbon-fibre composites by scanning acousticmicroscopy. *Composites Sci Technol, 52*:551-9.

[44]. Gao, S. L., & Kim, J. K. (1999). Scanning acoustic microscopy as a tool for quantitative characterisation of damage in CFRPs. *Composites science and technology, 59*(3), 345-354.

[45]. Gros, X. E., Ogi, K., & Takahashi, K. (1998). Eddy current, ultrasonic C-scan and scanning acoustic microscopy testing of delaminated quasi-isotropic CFRP materials: a case study. *Journal of reinforced plastics and composites, 17*(5), 389-405.

[46]. Loutas, T., Kostopoulos, V., Tsotra, P., Vavouliotis, A., Karapappas, P., & Tsantzalis, S. (2007). Damage detection during fatigue loading of CNF doped CFRPs via resistance measurements and AE. *Solid State Phenomena, 121*, 1399-1402.

[47]. Kostopoulos, V., Vavouliotis, A., Karapappas, P., Tsotra, P., & Paipetis, A. (2009). Damage monitoring of carbon fiber reinforced laminates using resistance measurements. Improving sensitivity using carbon nanotube doped epoxy matrix system. *Journal of Intelligent Material Systems and Structures, 20*(9), 1025-1034.

[48]. Vavouliotis, A., Karapappas, P., Loutas, T., Voyatzi, T., Paipetis, A., & Kostopoulos, V. (2009). Multistage fatigue life monitoring on carbon fibre reinforced polymers enhanced with multiwall carbon nanotubes. *Plastics, Rubber and Composites, 38*(2-4), 2-4.

[49]. Athanasopoulos, N., & Kostopoulos, V. (2011). Prediction and experimental validation of the electrical conductivity of dry carbon fiber unidirectional layers. *Composites Part B: Engineering, 42*(6), 1578-1587.

[50]. Vavouliotis, A., Paipetis, A., & Kostopoulos, V. (2011). On the fatigue life prediction of CFRP laminates using the electrical resistance change method. *Composites Science and Technology, 71*(5), 630-642.

[51]. Athanasopoulos, N., & Kostopoulos, V. (2012). Resistive heating of multidirectional and unidirectional dry carbon fibre preforms. *Composites Science and Technology*, *72*(11), 1273-1282.

[52]. Baltopoulos, A., Polydorides, N., Pambaguian, L., Vavouliotis, A., & Kostopoulos, V. (2013). Damage identification in carbon fiber reinforced polymer plates using electrical resistance tomography mapping. *Journal of Composite Materials*, *47*(26), 3285-3301.

[53]. Prasse, T., Michel, F., Mook, G., Schulte, K., & Bauhofer, W. (2001). A comparative investigation of electrical resistance and acoustic emission during

cyclic loading of CFRP laminates. *Composites science and technology*, *61*(6), 831-835.

[54]. Sevkat, E., Li, J., Liaw, B., & Delale, F. (2008). A statistical model of electrical resistance of carbon fiber reinforced composites under tensile loading. *Composites Science and Technology*, *68*(10), 2214-2219.

[55]. Louis, M., Joshi, S. P., & Brockmann, W. (2001). An experimental investigation of through-thickness electrical resistivity of CFRP laminates. *Composites science and technology*, *61*(6), 911-919.

[56]. Prabhakaran, R. (1990). Damage Assessment through Electrical Resistance Measurement in Graphite Fiber-Reinforced Composites. *Experimental Techniques*, *14*(1), 16-20.

[57]. Schueler, R., Joshi, S. P., & Schulte, K. (2001). Damage detection in CFRP by electrical conductivity mapping. Composites Science and Technology, 61(6), 921-930.

[58]. Wen, J., Xia, Z., & Choy, F. (2011). Damage detection of carbon fiber reinforced polymer composites via electrical resistance measurement. *Composites Part B: Engineering*, *42*(1), 77-86.

[59]. Xia, Z. H., & Curtin, W. A. (2008). Damage detection via electrical resistance in CFRP composites under cyclic loading. *Composites science and technology*, *68*(12), 2526-2534.

[60]. Ceysson, O., Salvia, M., & Vincent, L. (1996). Damage mechanisms characterisation of carbon fibre/epoxy composite laminates by both electrical

resistance measurements and acoustic emission analysis. *Scripta Materialia,34*(8), 1273-1280.

[61]. Fankhänel, B., Müller, E., Mosler, U., Siegel, W., & Beier, W. (2001). Electrical properties and damage monitoring of SiC-fibre-reinforced glasses. *Composites science and technology, 61*(6), 825-830.

[62]. Park, J. B., Okabe, T., Takeda, N., & Curtin, W. A. (2002). Electromechanical modeling of unidirectional CFRP composites under tensile loading condition. *Composites Part A: Applied Science and Manufacturing, 33*(2), 267-275.

[63]. Irving, P. E., & Thiagarajan, C. (1998). Fatigue damage characterization in carbon fibre composite materials using an electrical potential technique. *Smart materials and structures, 7*(4), 456.

[64]. Alexopoulos, N. D., Jaillet, C., Zakri, C., Poulin, P., & Kourkoulis, S. K. (2013). Improved strain sensing performance of glass fiber polymer composites with embedded pre-stretched polyvinyl alcohol–carbon nanotube fibers. *Carbon*, *59*, 65-75.

[65]. Abry, J. C., Bochard, S., Chateauminois, A., Salvia, M., & Giraud, G. (1999). In situ detection of damage in CFRP laminates by electrical resistance measurements. *Composites Science and Technology, 59*(6), 925-935.

[66]. Abry, J. C., Choi, Y. K., Chateauminois, A., Dalloz, B., Giraud, G., & Salvia, M. (2001). In-situ monitoring of damage in CFRP laminates by means of AC and DC measurements. *Composites Science and Technology, 61*(6), 855-864.

[67]. Flandin, L., Cavaille, J. Y., Brechet, Y., & Dendievel, R. (1999). Characterization of the damage in nanocomposite materials by ac electrical

properties: experiment and simulation. *Journal of materials science, 34*(8), 1753-1759.

[68]. Böger, L., Wichmann, M. H., Meyer, L. O., & Schulte, K. (2008). Load and health monitoring in glass fibre reinforced composites with an electrically conductive nanocomposite epoxy matrix. *Composites Science and Technology*, *68*(7), 1886-1894.

[69]. Todoroki, A., Omagari, K., Shimamura, Y., & Kobayashi, H. (2006). Matrix crack detection of CFRP using electrical resistance change with integrated surface probes. *Composites science and technology*, *66*(11), 1539-1545.

[70]. Thiagarajan, R. C., & Chiranjeevi, K. V. Micro Mechanical Exploration of Composites for Superior Properties.

[71]. Curtin, W. A. (2008). Multiscale Models of Multifunctional Composites for On-Board Damage Detection and Failure Prevention. *Brown University Providence of Engineering*.

[72]. Kupke, M., Schulte, K., & Schüler, R. (2001). Non-destructive testing of FRP by dc and ac electrical methods. *Composites Science and Technology*, *61*(6), 837-847.

[73]. Lubineau, G., Nouri, H., & Roger, F. (2013). On micro–meso relations homogenizing electrical properties of transversely cracked laminated composites. *Composite Structures, 105*, 66-74.

[74]. Vavouliotis, A., Paipetis, A., & Kostopoulos, V. (2011). On the fatigue life prediction of CFRP laminates using the electrical resistance change method. *Composites Science and Technology, 71*(5), 630-642.

[75]. Joy, T., & Strieder, W. (1979). Percolation in a thin ply of unidirectional composite. *Journal of Composite Materials, 13*(1), 72-78.

[76]. Xia, Z., Okabe, T., Park, J. B., Curtin, W. A., & Takeda, N. (2003). Quantitative damage detection in CFRP composites: coupled mechanical and electrical models. *Composites science and technology, 63*(10), 1411-1422.

[77]. Li, P., Strieder, W., & Joy, T. (1982). Random lattice electrical conductivity calculations for a graphite/epoxy ply of finite thickness. *Journal of Composite Materials, 16*(1), 53-64.

[78]. Chung, D. D. L., & Wang, S. (2003). Self-sensing of damage and strain in carbon fiber polymer-matrix structural composites by electrical resistance measurement. *Polymers and Polymer Composites, 11*(7), 515-525.

[79]. Wang, X., Wang, S., & Chung, D. D. L. (1999). Sensing damage in carbon fiber and its polymer-matrix and carbon-matrix composites by electrical resistance measurement. *Journal of materials science, 34*(11), 2703-2713.

[80]. Todoroki, A., Ueda, M., & Hirano, Y. (2007). Strain and damage monitoring of CFRP laminates by means of electrical resistance measurement. *Journal of Solid Mechanics and Materials Engineering, 1*(8), 947-974.

[81]. Zihlif, A. M., Ayish, I. O., & Elimat, Z. M. (2012). The AC electrical behavior of cement–polymer composite. *Journal of Thermoplastic Composite Materials*.

[82]. Thiagarajan, R. C.(2011). Multiscale Damage Detection in Conductive Composites. *COMSOl Conference*, Bangalore,India.

[83]. Irving, P. E., & Thiagarajan, C. (1998). Fatigue damage characterization in carbon fibre composite materials using an electrical potential technique. *Smart materials and structures, 7*(4), 456.

[84]. Huray P.G., (2010). *Maxwell's equation*, John Wiley & Sons, Inc. Hoboken, New Jersey

[85]. Fleisch D., (2008). *A student's guide to Maxwell's equations,* Cambridge University Press, New York.

[86]. Tuncer, E., Serdyuk, Y. V., & Gubanski, S. M. (2001). Dielectric mixtures--electrical properties and modeling. arXiv preprint cond-mat/0111254.

[87]. Kremer F., Dominguez L., Meyer W.H., Wenger G., (1989) *Polymer 30*:2023

[88]. Wagne R. W. (1914) *Arch Electrotech 2*:371

[89]. Sillars R. W. (1937) *J Inst Elect Eng 80*:378

[90]. Kremer F., Schonhals A., *Broadband Dielectric Spectroscopy*. in Springer-Verlag, 2002.

[91]. Abry, J. C., Chateauminois, A., Giraud, G., Henaff-Gardin, C., Lafarie-Frénot, M. C., & Salvia, M (1999). Damage Monitoring in CFRP Laminates by Means of Dielectric Properties, *ICCM-12*, Paris, France.

[92]. Reifsnider, K., Fazzino, P., and Majumdar, P. (2009). Material State changes as a basis for Prognosis in Aeronautical Structures. *J. Royal Aero. Soc., 113*#1150, 789-98.

[93]. Fazzino, P. and Reifsnider, K.L. (2008). Electrochemical Impedance Spectroscopy Detection of Damage in Out-of –Plane Fatigued Fiber Reinforced Composite Materials. *Appl. Composite Materials, 15*(3), 127-38.

[94]. Majumdar, P., Raihan, M., Reifsnider, K. and Rabbi, F. (2011). Effect of Porous electrode Morphology on Broadband Dielectric Characteristics of SOFC and Methodologies for Analytical Predictions. *Proc. ASME 2011, 9th Fuel Cell Science Engineering and Technology Conf.*, Paper # 54946.

[95]. Reifsnider, K., Raihan, R., & Majumdar, P. (2011). Durability Methodologies for Material Systems. ASME Pressure Vessels and Piping Conference. *Volume 6: Materials and Fabrication, Parts A and B*. Baltimore, Maryland, USA.

[96]. Cable, T. and Sophie S. (200), A Symmetrical Planar SOFC Design for NASA's High Specific Power Density Requirements. Journal of Power Sources, 174(1): p. 221-227.

[97]. Cable, T. L., Setlock, J. A., Farmer, S. C., & Eckel, A. J. (2011). Regenerative performance of the NASA symmetrical solid oxide fuel cell design. *International Journal of Applied Ceramic Technology*, *8*(1), 1-12.

[98]. Liu J., Duan C-G., Yin W-G., Mei W.N., Smith R.W., Hardy J.R. (2003). Dielectric Permittivity and Electric Modulus in Bi2Ti4O11 , J. *Chemical Physics, 199#5*, 2812-2819.

[99]. Liu Q. and K. Reifsnider K. (2012)Heterogeneous mixtures of elliptical particles: directly resolving local and global properties and responses. *Journal of Computational Physics* doi.org/10.1016/j.jcp.2012. 09.039

[100]. Baker, J., Adkins, J. M., Rabbi, F., Liu, Q., Reifsnider, K., & Raihan, R. (2014). Meso-design of heterogeneous dielectric material systems: Structure property relationships. *Journal of Advanced Dielectrics*.

[101]. Reifsnider, K. L., Raihan, R., & Liu, Q. (2013). Rational durability design of heterogeneous functional materials: Some first principles. *Mechanics of Composite Materials, 49*(1), 21-34.

[102]. Brosseau, C., Beroual, A., & Boudida, A. (2000). How do shape anisotropy and spatial orientation of the constituents affect the permittivity of dielectric heterostructures?. *Journal of Applied Physics, 88*(12), 7278-7288.

[103]. Boudida, A., Beroual, A., & Brosseau, C. (1998). Permittivity of lossy composite materials. *Journal of applied physics, 83*(1), 425-431.

[104]. Soles, C., Yee A. (2000). A discussion of the molecular mechanisms of moisture transport in epoxy resins. *Journal of Polymer Science, Part B: Polymer Physics, 38,* 792–802.

[105]. Adamson, M.J. (1980). Thermal expansion and swelling of cured epoxy resin used in graphite/epoxy composite materials. *Journal of Material Science, 15*, 1736–1745.

[106]. Tencer, M. (1994). Moisture ingress into nonhermetic enclosures and packages – a quasisteady state model for diffusion and attenuation of ambient humidity variations. *IEEE 44th Electronic Components Technology Conference*, Washington DC, USA.

[107]. Shirangi, M. H., & Michel, B. (2010). Mechanism of moisture diffusion, hygroscopic swelling, and adhesion degradation in epoxy molding compounds. In *Moisture Sensitivity of Plastic Packages of IC Devices* (pp. 29-69). Springer US.

[108]. Banhegyi, G., & Karasz, F. E. (1986). The effect of adsorbed water on the dielectric properties of CaCO3 filled polyethylene composites. *Journal of Polymer Science Part B: Polymer Physics, 24*(2), 209-228.3.

[109]. Banhegyi, G., Hedvig, P., & Karasz, F. E. (1988). DC dielectric study of polyethylene/CaCO3 composites. *Colloid and Polymer Science, 266*(8), 701-715.

[110]. Cotinaud, M., Bonniau, P., & Bunsell, A. R. (1982). The effect of water absorption on the electrical properties of glass-fibre reinforced epoxy composites. *Journal of Materials Science, 17*(3), 867-877.6. kremer ref chpter 59-65

[111]. Reid, J. D., Lawrence, W. H., & Buck, R. P. (1986). Dielectric properties of an epoxy resin and its composite I. Moisture effects on dipole relaxation. *Journal of applied polymer science, 31*(6), 1771-1784.

[112]. Paquin, L., St-Onge, H., & Wertheimer, M. R. (1982). The Complex Permittivity of Polyethylene/Mica Composites. *Electrical Insulation, IEEE Transactions on*, (5), 399-404.